

Pulsed laser deposition of efficient ternary metal oxide photoelectrodes

vorgelegt von
M. Sc.
Moritz Kölbach

von der Fakultät II – Mathematik und Naturwissenschaften
der Technischen Universität Berlin
zur Erlangung des akademischen Grades

Doktor der Naturwissenschaften
- Dr. rer. nat. -

genehmigte Dissertation

Promotionsausschuss:

Vorsitzender: Prof. Dr. Peter Hildebrandt

Gutachter: Prof. Dr. Roel van de Krol

Gutachter: Prof. Dr. Alfred Ludwig

Tag der wissenschaftlichen Aussprache: 06. Februar 2019

Berlin 2019

Abstract

Climate change, mainly driven by the combustion of fossil fuels releasing the greenhouse gas CO₂, is a major threat to humanity and the ecosystems on our planet. To limit global warming, a transition towards a sustainable energy infrastructure based on renewable energies is essential. The storage of solar energy in the form of chemical bonds, in so-called *solar fuels*, is thereby believed to be a key technology. This approach solves the problem of the intermittent nature of solar power—the only renewable energy source capable of meeting the still growing world energy demand on a TW scale. One possible pathway towards solar fuels is the generation of hydrogen via photoelectrochemical (PEC) water splitting using semiconducting photoelectrodes immersed in an aqueous electrolyte. However, the material that meets all the stringent requirements for efficient and commercially viable solar water splitting is still elusive.

Metal oxides are a promising class of photoelectrode materials because they are in general cheaper and more stable in aqueous solutions than conventional III-V semiconductors. Since only few—if any—of the simple binary oxides show the desired properties, recent efforts in the field have shifted towards investigating the more complex multinary oxides. To study the fundamental properties and performance limitations of such novel photoelectrode materials, one needs to be able to deposit thin and compact films of high electronic quality. Pulsed laser deposition (PLD) is a versatile physical vapor deposition technique that meets these demands. Therefore, in this thesis, this powerful tool is used to (i) deposit dense and high-quality BiVO₄ photoelectrodes and (ii) to comprehensively evaluate the new and promising material α -SnWO₄.

In the first part, the complex PLD process of BiVO₄ films by ablating a BiVO₄ target is systematically elucidated with a special focus on the deviations from an ideal stoichiometric target-to-substrate transfer. By correlating the V:Bi ratio of the films with their charge carrier transport properties and PEC performance, remarkable AM1.5 sulfite oxidation photocurrents of $2.4 \pm 0.2 \text{ mAcm}^{-2}$ at $E = 1.23 \text{ V vs. RHE}$ with stoichiometric films are achieved without any doping or nanostructuring. BiVO₄ photoelectrodes with similar PEC performance are additionally prepared for the first time by the alternating ablation of Bi₂O₃ and V₂O₅ targets. This approach is shown to be an attractive alternative route to control the cation stoichiometry and lays the foundation for the future growth of epitaxial BiVO₄ films.

The second part of this thesis contains a comprehensive evaluation of α -SnWO₄ as a novel photoelectrode material. α -SnWO₄ has recently attracted attention in the field due to the combination of a nearly ideal bandgap ($\sim 1.9 \text{ eV}$) and a very early photocurrent onset potential ($\sim 0 \text{ V vs. RHE}$). Using phase-pure pulsed laser deposited films, the close-to-optimum band alignment and bandgap is confirmed, and other important parameters such as the charge carrier mobility, lifetime, diffusion length, and the PEC stability are reported for the first time. A high-temperature treatment is shown to enhance the charge carrier mobility of α -SnWO₄ films by more than two orders of magnitude, as measured with time-resolved

microwave conductivity (TRMC). This results in one of the highest effective charge carrier diffusion lengths ever measured in a metal oxide photoelectrode (~ 200 nm). A complimentary analysis by time-resolved terahertz spectroscopy (TRTS) shows that this improvement can be attributed to larger grain/domain sizes with increasing heat-treatment temperature. In other words, grain boundaries significantly limit the charge carrier transport in α -SnWO₄. In addition, a hole-conductive NiO_x protection layer is introduced to prevent self-passivation of the surface of the α -SnWO₄ films (formation of a thin SnO₂ layer), which drastically increases the sulfite oxidation photocurrent by a factor of ~ 100 setting a new benchmark AM1.5 photocurrent density (~ 0.75 mA cm⁻² at E = 1.23 V vs. RHE) and IPCE ($\sim 38\%$ at $\lambda = 355$ nm) for α -SnWO₄. These findings provide important insights into the key PEC properties and performance limitations of α -SnWO₄, and allow the identification of strategies to further improve the performance of this promising photoanode material.

Kurzfassung

Der Klimawandel, welcher hauptsächlich durch die Verbrennung fossiler Brennstoffe zur Energiegewinnung und den daraus resultierenden Emissionen des Treibhausgases CO_2 vorangetrieben wird, ist eine immense Bedrohung für die Menschheit und Ökosysteme unserer Erde. Um die globale Erwärmung zu begrenzen, ist ein Übergang von fossilen zu erneuerbaren Energien essentiell. Dabei wird der Speicherung von solarer Energie in Form von chemischen Bindungen in sogenannten solaren Brennstoffen eine bedeutende Rolle zugeschrieben. Dieses an die Photosynthese in Pflanzen angelehnte Konzept löst das Problem der diskontinuierlich verfügbaren Solarenergie, welche unverzichtbar ist um den stetig wachsenden Weltenergiebedarf auf einer TW-Skala zu decken. Eine Möglichkeit solare Brennstoffe herzustellen ist die Produktion von Wasserstoff mittels photoelektrochemischer Wasserspaltung mit Hilfe von in wässrigen Lösungen eintauchenden halbleitenden Photoelektroden. Das Photoelektrodenmaterial, das alle strikten Anforderungen erfüllt um hoch-effizient und wirtschaftlich Wasserstoff zu erzeugen, wurde jedoch noch nicht gefunden.

Metalloxide stellen eine vielversprechende Materialklasse für Photoelektroden dar, weil sie generell günstiger und stabiler sind als konventionelle III-V Halbleiter. Da nur wenige der binären Oxide geeignete Eigenschaften besitzen, werden in diesem Forschungsfeld nun auch komplexere multinäre Oxide untersucht. Um die fundamentalen Eigenschaften und limitierenden Faktoren zu erforschen, werden kompakte Filme von hoher elektronischer Qualität benötigt. Die gepulste Laserabscheidung („pulsed laser deposition“, PLD) ist ein vielseitiges physikalisches Gasphasenabscheidungs-Verfahren, das diese Anforderungen erfüllt. Daher wird es in dieser Arbeit genutzt, um zum einen (i) kompakte und qualitativ hochwertige BiVO_4 Photoelektroden abzuscheiden und zum anderen (ii) das neue und vielversprechende Material $\alpha\text{-SnWO}_4$ umfassend zu untersuchen.

Im ersten Teil dieser Arbeit wird der komplexe gepulste Laserabscheidungsprozess von BiVO_4 Filmen mittels Ablation eines BiVO_4 Targets systematisch mit besonderem Hinblick auf Abweichungen von einem idealen stöchiometrischen Target-zu-Substrat Transfer untersucht. Dabei wird das V:Bi Verhältnis der Filme mit deren Ladungsträgertransport und photoelektrochemischen Aktivität korreliert und so ohne jegliche Dotierung oder Nanostrukturierung relativ hohe AM1.5 Photoströme mit stöchiometrischen Filmen erzielt ($2.4 \pm 0.2 \text{ mAcm}^{-2}$ bei $E = 1.23 \text{ V vs. RHE}$ mit Na_2SO_3 als Lochfänger). Darüber hinaus werden BiVO_4 Photoelektroden mit einer ähnlich hohen Photoaktivität zum ersten Mal durch die alternierende Ablation von Bi_2O_3 und V_2O_5 Targets hergestellt. Dieser Ansatz stellt sich als eleganter alternativer Weg heraus, die kationische Stöchiometrie von Metalloxiden zu kontrollieren und legt die Grundlage für das zukünftige Abscheiden von epitaktischen Schichten.

Im zweiten Teil der Arbeit wird $\alpha\text{-SnWO}_4$ ausführlich als Photoelektrodenmaterial evaluiert. Dieses Material erregte Aufmerksamkeit aufgrund seiner nahezu idealen Bandlücke

(~1.9 eV) und seines bei sehr negativen Potentialen einsetzenden Photostroms (~0 V vs. RHE). Mittels gepulster Laserabscheidung hergestellte α -SnWO₄ Filme werden benutzt, um die schon in der Literatur bekannte Bandanordnung und -lücke zu bestätigen und zum ersten Mal weitere essentielle Eigenschaften wie die Mobilität, Lebensdauer und Diffusionslänge der Ladungsträger sowie die photoelektrochemische Stabilität zu untersuchen. Es wird gezeigt, dass die mittels zeit-aufgelöster Mikrowellen Spektroskopie gemessene Ladungsträgermobilität durch eine Hochtemperatur-Behandlung der Schichten um mehr als zwei Größenordnungen erhöht werden kann. Daraus ergibt sich für α -SnWO₄ eine der größten je gemessenen Diffusionslängen in Metalloxid Photoelektroden (~200 nm). Eine ergänzende Analyse mittels zeit-aufgelöster Terahertz Spektroskopie zeigt, dass diese Verbesserung auf größere Korngrößen in den hochtemperaturbehandelten Schichten zurückgeführt werden kann und liefert die wichtige Erkenntnis, dass Korngrenzen den Ladungstransport in α -SnWO₄ limitieren. Zusätzlich wird eine lochleitende NiO_x Schutzschicht auf die α -SnWO₄ Filme aufgetragen, die die Selbstpassivierung (Oxidation der Oberfläche zu SnO₂) verhindert. Dadurch wird der Photostrom (mit Na₂SO₃ als Lochfänger) um einen Faktor von ~100 erhöht und so neue Maßstäbe für den AM1.5 Photostrom (~0.75 mA cm⁻² bei $E = 1.23$ V vs. RHE) und die Quanteneffizienz (~38% bei $\lambda = 355$ nm) für dieses Material gesetzt. Diese Ergebnisse liefern wichtige Erkenntnisse über Schlüssel-Parameter von α -SnWO₄ und zeigen Strategien auf, die Performance von diesem vielversprechenden Photoelektrodenmaterial weiter zu verbessern.

Table of contents

Chapter 1 – Introduction	1
1.1 <i>Climate change & energy crisis</i>	2
1.2 <i>From solar to fuel: The key role of hydrogen</i>	5
1.3 <i>Principles of photoelectrochemical water splitting</i>	9
1.3.1 Basics of semiconductors	10
1.3.2 Semiconductor/electrolyte interface	14
1.3.3 Semiconductor requirements and device concepts for efficient solar water splitting.....	17
1.4 <i>Metal oxide photoelectrodes</i>	23
1.4.1 BiVO ₄	25
1.4.2 α -SnWO ₄	27
1.5 <i>This thesis</i>	29
Chapter 2 – Methods & experimental section	30
2.1 <i>Sample preparation</i>	31
2.1.1 Pulsed laser deposition of metal oxides.....	31
2.1.2 Target preparation	32
2.1.3 Fabrication of BiVO ₄ films.....	33
2.1.4 Fabrication of α -SnWO ₄ films	34
2.2 <i>Analysis methods</i>	35
2.2.1 Rutherford backscattering spectrometry (RBS)	35
2.2.2 X-ray diffraction (XRD)	36
2.2.3 Time-resolved microwave conductivity (TRMC).....	38
2.2.4 Photoelectrochemical (PEC) measurements	41
2.2.5 Other methods.....	43
Chapter 3 – Elucidating the pulsed laser deposition process of efficient BiVO₄ photoelectrodes for solar water splitting	47
3.1 <i>Introduction</i>	48
3.2 <i>Control of the V:Bi ratio</i>	49
3.3 <i>Structural characterization & charge carrier dynamics</i>	54
3.4 <i>Photoelectrochemical characterization</i>	58
3.5 <i>Alternating target approach</i>	61
3.6 <i>Conclusion</i>	64

Chapter 4 - α-SnWO₄: a new promising photoanode material for solar water splitting	65
4.1 <i>Introduction</i>	66
4.2 <i>PLD process, structural & optical characterization of α-SnWO₄ thin films</i>	67
4.3 <i>Charge carrier dynamics in α-SnWO₄</i>	76
4.4 <i>Photoelectrochemical characterization & NiO_x protection layer</i>	82
4.5 <i>Conclusion</i>	88
Summary	90
Appendix	93
a) <i>Supplemental information</i>	94
b) <i>List of abbreviations</i>	112
c) <i>List of figures</i>	115
d) <i>List of tables</i>	120
e) <i>Publications</i>	121
f) <i>Acknowledgement</i>	122
g) <i>References</i>	124

Chapter 1 – Introduction

1.1 Climate change & energy crisis

One of the greatest scientific and social challenges for humanity in the coming decades is to establish a sustainable energy supply that stops man-made climate change. But how did we get to this point?

Since the industrial revolution in the 19th century, the world's energy demand has steadily increased. In 2017, ~7.5 billion people on our planet consumed ~18 TW of energy.^[1] With a continuously growing world population and world economy, this value is estimated to further increase to ~24 TW by 2040.^[2] From the beginning of industrialization, fossil fuels (i.e., coal, oil, and natural gas) have met the major part of our energy demands and currently (2017) cover ~85% of the world's energy consumption.^[1] Although the proven available reserves of fossil fuels are still enough for a relatively long period of time (200 years for coal and 50 years for oil/natural gas based on the predicted consumption rates for the year of 2040^[1-2]), meeting the world's energy demand on the long run is clearly not sustainable.

An even greater concern, however, is that combusting fossil fuels emits the greenhouse gas CO₂, which is the main driving force of global warming. This is illustrated in **Figure 1a**, which depicts the steadily increased CO₂ emissions from the beginning of the industrialization up until now. More than 80% of the current annual global emissions (~40 Gt) can be attributed to the combustion of fossil fuels in the energy sector.^[3] As a result, the concentration of CO₂ in the earth's atmosphere has increased up to a current (2018) value of 407 ppm^[4] (inset **Figure 1a**). This is already accompanied by an increase of the global annual temperature by ~0.9°C (**Figure 1b**).

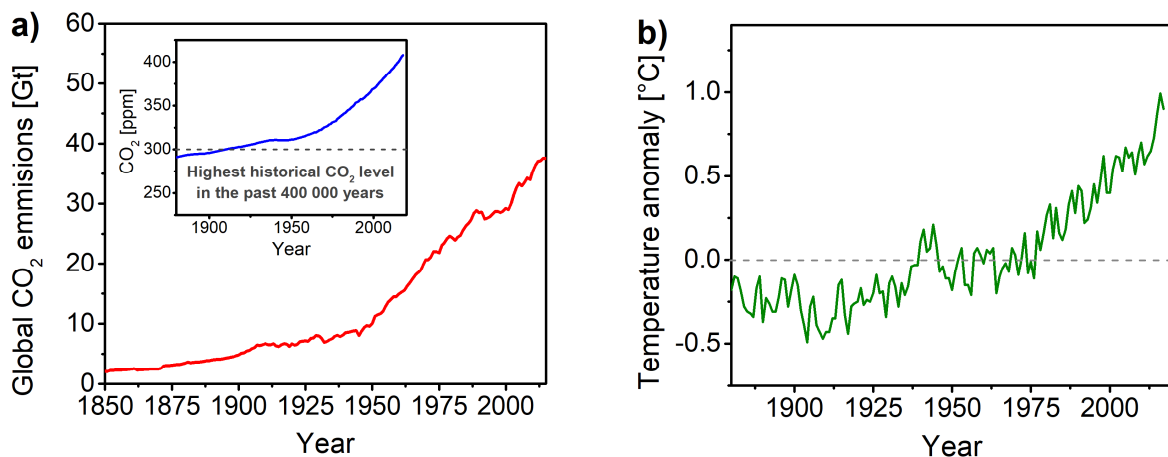


Figure 1. **a)** Global CO₂ emissions from 1850 up until now adapted from reference ^[3]. Inset: CO₂ concentration in the earth's atmosphere according to reference ^[5]. **b)** Global annual mean surface air temperature change from 1880 until now revealing a global warming of 0.9°C (base period: 1951-1980) adapted from reference ^[6].

If the current increase of the CO₂ concentration in the atmosphere of ~2 ppm per year is not stopped, the global temperature is expected to continuously increase, and the consequences for the human society and ecosystems will be disastrous: melting of glaciers,

rising of the sea level, extreme weather events (storms, floods, and droughts), famines, political instability, and ultimately, uninhabitability of the earth for humans. The urgency of the problem was recently illustrated by Steffen et al., who issued a warning about tipping elements and domino-like cascades which could accelerate global warming and result in a *hothouse earth*.^[7] **Figure 2** depicts a world map with the location of these tipping elements divided into three clusters according to their estimated trigger temperature. Elements of the first cluster (e.g., melting of the Greenland and West Antarctic ice sheet) could already be triggered by an increase of the global temperature by only 1–3°C, which might subsequently trigger the second and the third cluster.

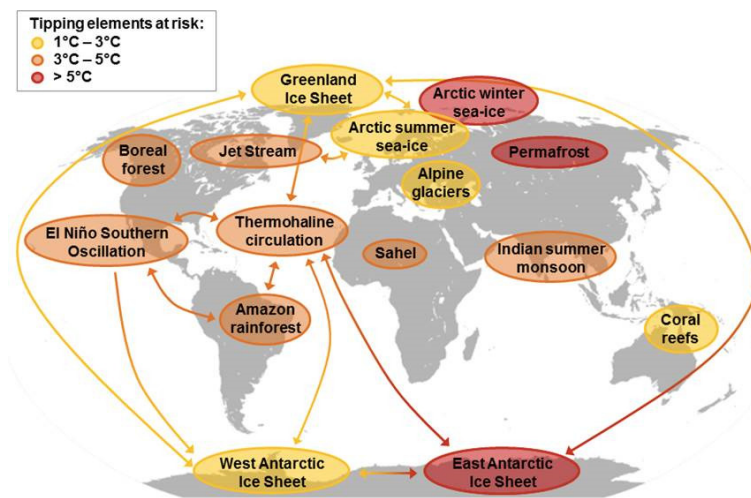


Figure 2. World map with the location of potential tipping cascades with estimated threshold temperatures (change of the global surface temperature) adapted from reference ^[7].

As a response to the threat of climate change, 181 nations declared to pursue efforts to limit global warming to 1.5–2°C in the Paris Agreement from 2015 within the United Nations Framework Convention on Climate Change (UNFCCC).^[8] To achieve the aim of the Paris Agreement and stop climate change, the global CO₂ emissions have to be substantially reduced. Therefore, a large-scale transition to renewable and carbon-neutral energy sources (e.g., wind, solar, hydroelectricity, bio mass, geothermal, and tidal/ocean currents) is the most important action to take. Any future sustainable energy scenario will likely be a mixture of these sources tailored to regional conditions as climate, geography and population density. However, since renewable energies have to be implemented on a Terawatt scale in a fossil fuel-free energy scenario, solar energy will undoubtedly be of great importance. This is illustrated in **Figure 3** that shows the estimated global power capacities of various renewable energies sources. It can be clearly seen that the global power capacity of the sun far exceeds that of any other source. The total power that reaches the earth's surface is ~120.000 TW. To generate a power of 20 TW (higher than the current world energy consumption of 18 TW^[11]) only 0.16% of the earth's surface has to be covered with 10% efficient solar cells (see inset **Figure 3**).^[9] In 2017, the total installed photovoltaic capacity was ~0.4 TW which is expected to double in the next five years.^[10] This growing photovoltaic

market and the high power capacity of the sun leave no doubt that solar energy will play a key role in a future sustainable energy scenario and in the fight against climate change.

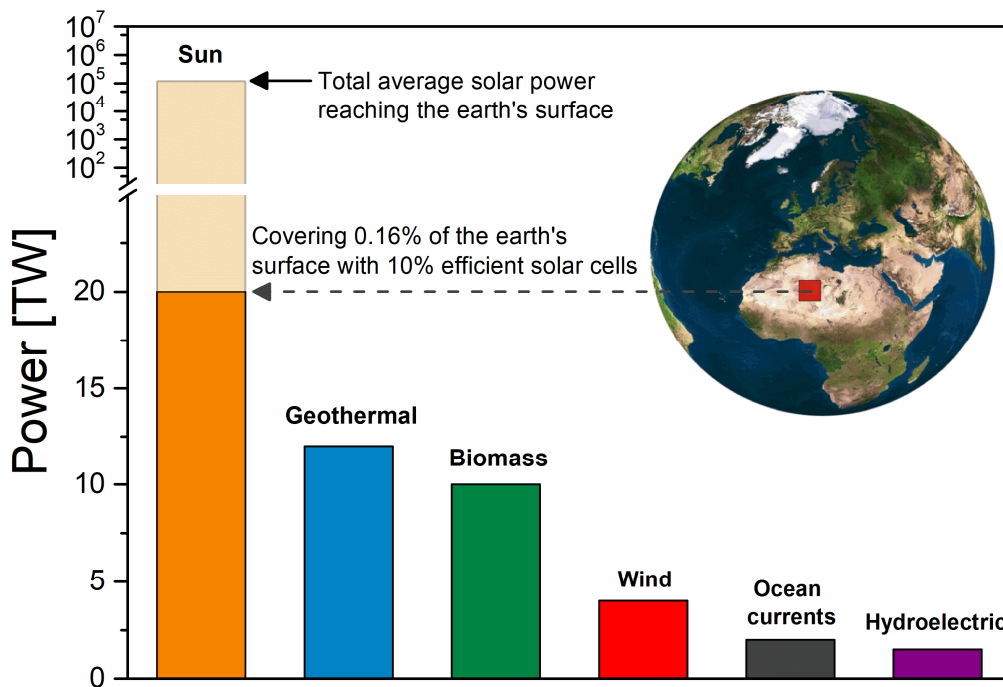


Figure 3. Global power capacities of sustainable energy resources adapted from references ^[9,11]. Inset: Area of the earth's surface needed to be covered with 10% efficient solar cells to generate a power of 20 TW adapted from reference ^[9].

1.2 From solar to fuel: The key role of hydrogen

Despite the high power capacity of solar energy as discussed above, there is a major issue to solve: the energy production using photovoltaics is directly dependent on the day/night cycle, the time of the year, atmospheric conditions (clouds) as well as the geographical position. Due to its natural variability and intermittency, the peak supply period of solar energy does not typically match the peak demand period. The intermittent nature of the energy output presents a major problem when solar energy should be used on a TW scale, since grid-based storage capacities will be exceeded at a certain point. Therefore, large-scale storage solutions of solar energy are essential in a future sustainable energy scenario.

One promising and elegant pathway is the storage of solar energy in the form of chemical bonds in the so-called *solar fuels*. This process is also referred to as *artificial photosynthesis* since it mimics the ability of plants in nature to convert CO₂, H₂O and sunlight into chemical energy stored in carbohydrate molecules. Solar fuels have two major advantages: (i) they can be easily transported over long distances (e.g., in pipelines) and (ii) they have very high energy densities as compared to other storage systems such as capacitors, gravity-based mechanical systems, or batteries as can be seen in **Table 1**.

Table 1: Gravimetric and volumetric energy densities of various energy storage technologies

Storage system	Energy density	
	Gravimetric [MJ kg ⁻¹]	Volumetric [MJ l ⁻¹]
Capacitors		
Supercapacitor ^[12]	< 0.018	-
Ultracapacitor ^[12]	0.045	-
Mechanical		
Pumped-storage	0.001 (100 m height)	0.001 (100 m height)
Hydroelectricity		
Flywheels ^[13]	1.1	-
Compressed air ^[12]	-	0.0072–0.0432
Batteries		
Pb ^[14]	0.126–0.144	0.288–0.324
Li-ion ^[15]	0.936	2.772
Fuels		
Coal ^[9]	24	-
Wood ^[9]	16	-
Gasoline ^[9]	44	35
Diesel ^[9]	46	37
Natural gas ^[9]	54	0.036
Hydrogen ^[9]	143	0.011 / 5.6 (700 bar)

Among the fuels listed in **Table 1**, hydrogen stands out as the simplest of the chemical fuels and is believed to play a key role in a future sustainable energy scenario. In contrast to the reduction of CO₂ to carbon based fuels including complex half-cell reactions involving up

to eight-electron transfer steps, hydrogen production from water splitting is technically and scientifically more feasible. This process only involves a two- and four-electron transfer steps for the reduction and oxidation half reaction, respectively. In addition, water is a much more convenient and abundant source than CO₂ captured from the atmosphere.^[16-17] To store the energy the world is predicted to consume by 2040, a volume of ~40 km³ water is required. For comparison, this is roughly the amount of water in the lake Bodensee in Germany or only ~3 × 10⁻⁹% of the amount in the oceans. Produced by solar energy, as discussed later in detail, hydrogen cannot only be directly converted into electricity in a fuel cell but is also an important feedstock element for industrial chemical processes (**Figure 4**). Many of these processes currently use non-renewable hydrogen produced from steam reforming. For example, hydrogen is essential for ammonia production in the Haber-Bosch-process which is in turn crucial to produce fertilizers needed to grow enough food for the growing world population. In addition, hydrogen can be used to produce methane (via the methanation of CO₂) or it can be converted to other liquid fuels or specialty chemicals (via Fischer-Tropsch reactions). These processes are already highly developed and used on a large scale in the chemical industry; it could therefore circumvent the challenging direct reduction of CO₂ as discussed above.

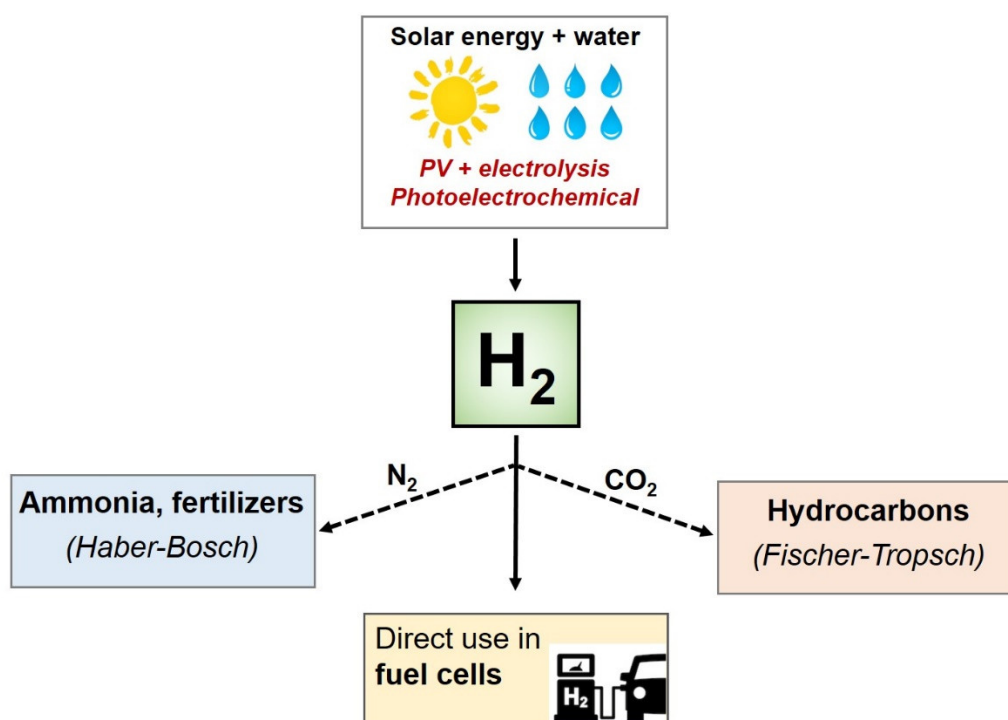


Figure 4. Future sustainable energy infrastructure with hydrogen produced by solar energy as a key element.

A sustainable energy scenario with renewable hydrogen as a key element is often referred to as a Hydrogen Economy. Global companies as Shell, Total or Linde joined together and founded the Hydrogen Council with the aim to foster the transition towards such a sustainable energy system.^[18] For example, the Japanese automobile manufacturer Toyota is currently further pushing the development of fuel cells for powering vehicles as an alternative to Li-ion batteries. In the summer of 2018, the first fuel cell powered trains from

the French company Alstom received authorization from the German Railway Agency. During the writing of this thesis, the first train was put into operation on the 16th of September 2018.^[19] Another example is the “Nationale Organisation Wasserstoff” (national hydrogen organization) based in Germany currently working on establishing an infrastructure for fuel cell powered cars in Germany and Europe. Recently, they opened the 50th public hydrogen refueling station in Germany.^[20] To realize a global energy system based on hydrogen, however, the infrastructure has to be further developed, the cost of fuel cells have to be reduced, and cheap hydrogen has to be produced with solar energy. In addition, such a transition will not work without the support of the governments of the world that have to keep investing and subsidizing hydrogen technologies and put a price on CO₂ emissions (carbon tax).

Many different routes towards renewable hydrogen production such as thermochemical methods, bio-artificial, plasma-chemical conversion and coupled photovoltaic–electrolysis systems are currently being studied. For the coming 2-3 decades, however, photovoltaics-powered electrolysis will be the technology of choice for practical applications. According to recent estimates, the hydrogen production cost via PEM electrolysis amounts to \$3.40–\$6.60/kg H₂ assuming an electricity cost of \$0.03–\$0.08 per kWh^[21]; the latter is indeed already achievable with photovoltaics.^[22] This production cost is already close to the target of \$2.00–\$4.00/kg H₂ per gasoline gallon equivalent set by the U.S. Department of energy (DOE).^[23]

In this thesis, the focus is on hydrogen production via photoelectrochemical water splitting. Compared to coupled photovoltaic–electrolysis systems, the light absorption and the water splitting functionalities are integrated into one device. This approach was first (partially) realized by Fujishima and Honda in 1972 using an n-type semiconducting TiO₂ photoelectrode connected to a platinum counter electrode immersed in an aqueous electrolyte.^[24] Upon UV-light irradiation, oxygen and hydrogen were evolved at the photo- and the counter electrode, respectively. Even though great progress has been made in the field in the last decades, no photoelectrochemical water splitting device with a stable operation on the time scale of years and a lower hydrogen production cost than coupled photovoltaic–electrolysis systems has been realized. Nevertheless, this approach offers several theoretical advantages over coupled photovoltaic–electrolysis systems. In state-of-the-art PEM electrolyzers with efficiencies of 70-80%, highly active catalysts based on noble metals (e.g., platinum and iridium) are used due to the high operating current densities of 1–2 A cm⁻². Currently, the costs for these catalysts are only a small fraction of the whole electrolyzer system. However, this could change when solar water splitting should be implemented on a TW scale. In contrast, photoelectrochemical devices operate at much lower current densities of 10-20 mA cm⁻² reducing the demands on the catalysts and thus enabling the use of earth-abundant and low-cost catalyst materials. Another advantage of the direct approach is the heat management. In a photoabsorber with an efficiency of 20% and 10% reflection losses, 70% of the incoming light is transformed into heat. In photovoltaic

devices, this heat can lead to efficiency losses of up to 10% due to operating temperature of 60-80°C.^[25] In PEC devices, however, the electrolyte constantly cools the absorber resulting in smaller losses, especially when convective flow systems are integrated. In addition, according to Arrhenius' law, the electrochemical reaction kinetics increase by a factor of ~2 per 10°C. Recent studies have shown that this benefit can outweigh the performance loss of the light absorber.^[26-27]

In conclusion, due to the advantages discussed above direct photoelectrochemical water splitting is a worthwhile goal. By pursuing this aggressively this technology may become relevant in the second half of this century. However, as discussed in the following subchapter, substantial breakthroughs and developments are required to achieve this goal.

1.3 Principles of photoelectrochemical water splitting

Figure 5 shows a schematic illustration of the simplest photoelectrochemical device to generate hydrogen by solar water splitting. It consists of a semiconducting photoelectrode (in this case n-type) connected to a metal counter electrode, both immersed in an aqueous electrolyte. Under solar illumination, electron-hole pairs are generated and separated in the semiconductor.

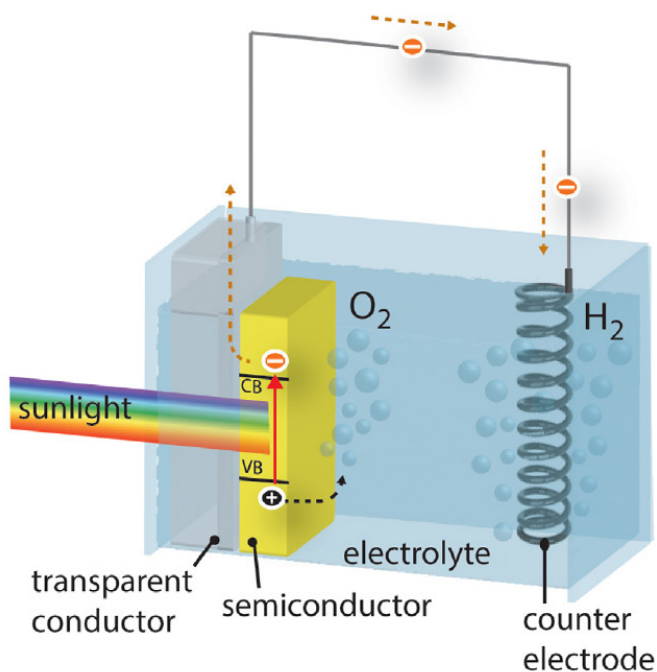
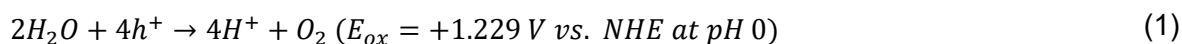


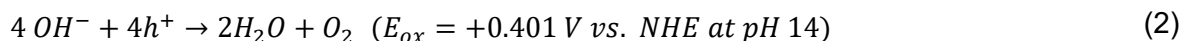
Figure 5. Schematic illustration of a photoelectrochemical water splitting device based on an n-type semiconducting photoelectrode and a metal counter electrode, both immersed in an aqueous electrolyte adapted from reference [28].

The holes are swept towards the semiconductor/electrolyte interface and drive the oxygen evolution reaction (OER) according to the following half-reactions:

Acidic electrolyte:

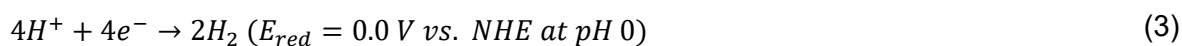


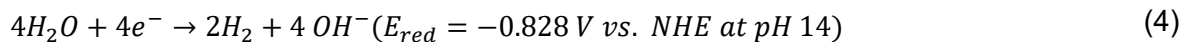
Alkaline electrolyte:



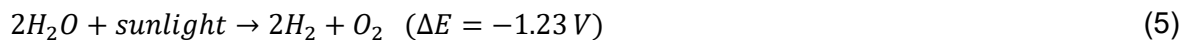
The electrons are swept towards the counter electrode via an external circuit and drive the hydrogen evolution reaction (HER) as follows:

Acidic electrolyte:



Alkaline electrolyte:

The overall water splitting reaction can be written as follows:



The key component of all PEC water splitting devices is the semiconducting photoelectrode. For this reason, the basics of semiconductors and the energetics at the semiconductor/electrolyte interface are discussed in this chapter. In addition, the requirements on the semiconductors to build a highly efficient and economically viable PEC water splitting device are reviewed, and different device concepts are presented.

1.3.1 Basics of semiconductors

According to quantum mechanics, electrons can only occupy atomic orbitals with discrete energy levels. In addition, the Pauli Exclusion Principle states that no two electrons in an atom or a molecule are allowed to have the same set of quantum numbers n (principal), l (angular momentum), m (magnetic) and s (spin). As a result, when two atoms are brought close together, the atomic orbitals overlap and split into bonding and anti-bonding molecular orbitals with different energy levels. When a large number of N atoms are brought together such as in a crystal lattice ($N \sim 10^{22} \text{ cm}^{-3}$), all of the atomic orbitals split into N molecular orbitals resulting in closely spaced discrete energy states. These states can be considered as a continuum and are therefore referred to as energy bands. The energy band formed by the bonding molecular orbitals is mostly filled with electrons and is called the valence band, whereas the energy band formed by the anti-bonding molecular orbitals is mostly empty and is referred to as the conduction band. In between the valence and conduction band edges is a region where no energy states are allowed; this region is called the bandgap.

The size of the bandgap (E_g) of a material defines its opto-electrical properties and is commonly used to classify materials into three different groups: (i) metals, (ii) semiconductors and (iii) insulators (**Figure 6a**). Only partially filled energy bands can carry an electrical current. In a metal, no bandgap exists, i.e., the valence band and the conduction band overlap. This results in a partially filled band, which explains the good conductivity of metals. When the bandgap is very large and nearly no thermal excitation of electrons into the conduction band is possible, the material is a poor conductor and is referred to as an insulator.

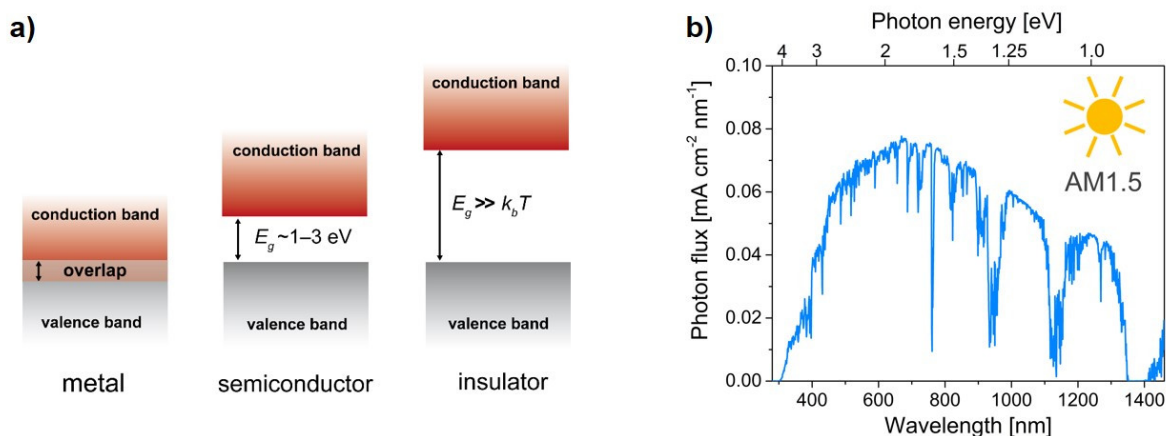


Figure 6. a) Classification of materials based on their bandgap energy in metals, semiconductors and insulators. b) Photon flux of AM1.5 irradiation as a function of the wavelength (low x-axis) and photon energy (upper x-axis).

With a bandgap energy of $\sim 1-3 \text{ eV}$, semiconductors lie in between metals and insulators. Even though this bandgap energy is too high for extensive thermal excitation of electrons at room temperature, it is in the energy range that can be provided by the sunlight (AM1.5) as shown in **Figure 6b**. As a result, an electron can be excited from the valence band of a semiconducting material to the conduction band upon AM1.5 illumination creating a mobile hole (missing electron) in the valence band and a mobile electron in the conduction band. These bands are now partially empty and partially filled, respectively, and can therefore carry a current. Moreover, the separation of these photogenerated carriers by an electric field (see below) results in a photocurrent and a photovoltage (i.e., the conversion of sunlight into electricity). This is the basis process of any solar cell or photoelectrochemical water splitting device.

Figure 7 depicts the definitions of other important parameters to describe a semiconducting material besides its bandgap. The vacuum level (E_{vac}) is defined as the energy where an electron has no kinetic energy with respect to the surface. The ionization energy (I_E) is the difference between the energy of the valence band maximum (E_{VBM}) and the vacuum level, i.e., the minimum energy needed to remove an electron from the system. The difference between the vacuum level and the conduction band minimum (E_{CBM}) is defined as the electron affinity (EA) which is the energy gained when an electron from the vacuum level occupies the lowest unoccupied state in the semiconductor. The Fermi level (E_F) is one of the most important parameters in a semiconductor. It is defined as the energy level with an occupation probability of exactly 50% and can be seen as the electrochemical potential of electrons in the semiconductor. The work function (Φ) of a semiconductor is defined as the energy difference between E_{vac} and E_F .

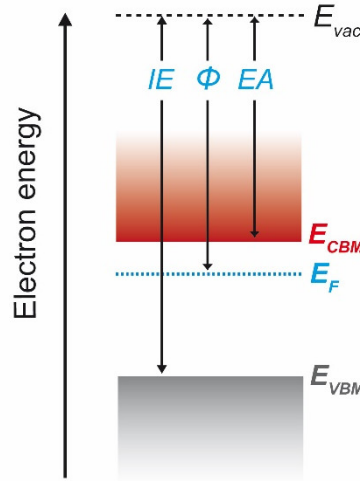


Figure 7. Energy diagram of a semiconductor including the definitions of the vacuum level (E_{vac}), energy of the valence band maximum (E_{VBM}), energy of the conduction band minimum (E_{CBM}), Fermi level (E_F), ionization energy (IE), work function (Φ), and electron affinity (EA).

At absolute zero temperature (0 K), no thermal excitation from the valence band into the conduction band is possible. As a result, all states in the valence band are occupied whereas the conduction band is completely empty and the Fermi level is located at an energy level (almost) exactly in between the valence and conduction band. Above 0 K, the distribution of electrons can be described by the Fermi-Dirac distribution and the density of states. The former one defines the occupation probability of an energy level E by an electron at a certain temperature and is given by the following equation:

$$f(E) = \frac{1}{\exp\left(\frac{E - E_F}{k_b T}\right) + 1} \quad (6)$$

where E_F is the Fermi energy, k_b is the Boltzmann constant and T is the temperature. The density of states (DOS, $g(E)$) is defined as the number of energy states per energy interval at an energy level E and is given by the following equations for the conduction band ($g_c(E)$) and valence band ($g_v(E)$):

$$g_c(E) = \frac{m_e^* \sqrt{2m_e^*(E - E_{CBM})}}{\pi^2 \hbar^3} \quad (7)$$

$$g_v(E) = \frac{m_h^* \sqrt{2m_h^*(E_{VBM} - E)}}{\pi^2 \hbar^3} \quad (8)$$

Here, h is Planck's constant ($\hbar = h/2\pi$), E_{CBM} is the energy of the conduction band minimum, E_{VBM} is the energy of the valence band minimum and m_e^* and m_h^* are the effective masses of electrons and holes, respectively. The combination of both the Fermi-Dirac distribution and the density of states yields the number of electrons (n) and holes (p) in the conduction and valence band, respectively, and can be expressed as follows:

$$n = \int_{E_{CBM}}^{E_{top}} g_c(E) f(E) dE \quad (9)$$

$$p = \int_{E_{CBM}}^{E_{top}} g_v(E) (1 - f(E)) dE \quad (10)$$

Under the assumption that the Fermi level is more than $\sim 3k_bT$ away from the conduction and the valence band (i.e., in a non-degenerate semiconductor), equation (9) and (10) can be simplified to the following expressions:

$$n = N_C \exp\left(\frac{E_F - E_{CBM}}{kT}\right) \text{ with } N_C = 2 \left(\frac{2\pi m_e^* kT}{h^2}\right)^{3/2} \quad (11)$$

$$p = N_V \exp\left(\frac{E_{VBM} - E_F}{kT}\right) \text{ with } N_V = 2 \left(\frac{2\pi m_h^* kT}{h^2}\right)^{3/2} \quad (12)$$

where N_C and N_V are the effective densities of states in the conduction and valence band, respectively.

For the application of semiconductors as photoabsorbers in solar cells or as photoelectrodes in PEC water splitting a good conductivity is required. The conductivity (σ) of a material is given by:

$$\sigma = ne\mu_e + pe\mu_p \quad (13)$$

Therefore, a higher concentration of the free electrons n or free holes p will increase the conductivity. This can be realized with doping, i.e., the incorporation of impurities in the semiconductor. There are two types of dopants depending on their valency with respect to the semiconductor host atom: donor- and acceptor-type dopants. The former one has a higher valency than the host atom (e.g., phosphorus in silicon). The additional electrons can be excited to the conduction band, increase the electron concentration and thus the conductivity of the semiconductor. Such a donor-doped semiconductor with electrons as the majority carriers is referred to as an *n-type* semiconductor. Because of the higher concentration of electrons in the conduction band, the Fermi level is shifted closer to the conduction band edge, as shown in **Figure 8a**. In contrast, when an acceptor dopant with a smaller valency than the host atom is introduced (e.g., boron in silicon), an electron can be excited from the valence band to the energy level of the acceptor species thereby increasing the concentration of holes in the valence band. In such a *p-type* semiconductor, the holes are the majority carriers and the Fermi level is closer to the valence band (**Figure 8b**).

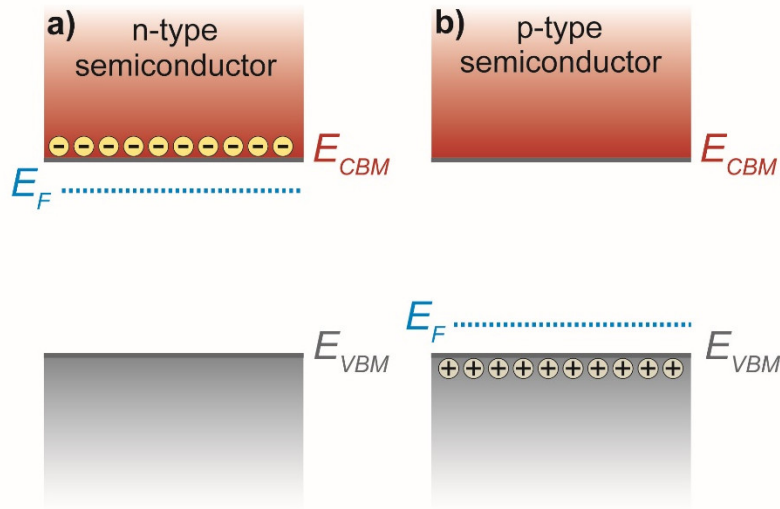


Figure 8. Energy diagrams of a) n-type semiconductor and b) p-type semiconductor.

1.3.2 Semiconductor/electrolyte interface

In a PEC water splitting device, the semiconducting photoelectrode is in direct contact with an aqueous electrolyte and illuminated with sunlight. The physicochemical processes occurring at the semiconductor/electrolyte interface are crucially important in the solar water splitting process. Since the work in this thesis focuses on n-type photoelectrodes, these processes are summarized for an n-type semiconductor. Similar considerations for p-type semiconductors can be found elsewhere.^[9]

Figure 9a depicts the isolated energy diagram of an n-type semiconductor and the electrolyte. When the semiconductor gets in contact with the electrolyte (**Figure 9b**), charges flow between the semiconductor and the electrolyte until an equilibrium is reached, i.e., the Fermi level and the redox potential of the electrolyte have the same energy level. In the case of an n-type semiconductor, the majority carriers (electrons) usually flow to the semiconductor/electrolyte interface and leave behind the non-mobile ionized donor species. The net positive charge in this ‘depletion region’ induces an upward band bending.

This depletion layer is also called the space charge layer and is of great importance for PEC water splitting. This is simply because the potential drop (Φ_{SC}) in the layer is favorable for the separation of the photogenerated electrons and holes needed for the water splitting reactions. The width of the space charge layer (W_{SC}) is given by the following equation:

$$W_{SC} = \sqrt{\frac{2\varepsilon_0\varepsilon_r}{eN_D} \left(\Phi_{SC} - \frac{k_bT}{e} \right)} \quad (14)$$

Here, ϵ_0 is the dielectric permittivity of vacuum, ϵ_r is the relative dielectric permittivity of the semiconductor, e is the electronic charge, N_D is the density of the ionized donors, Φ_{SC} is the potential drop in the space charge layer, and all other symbols have their usual meaning. The capacitance (C_{SC}) of the space charge layer is typically between 10–1000 nF cm⁻².^[9]

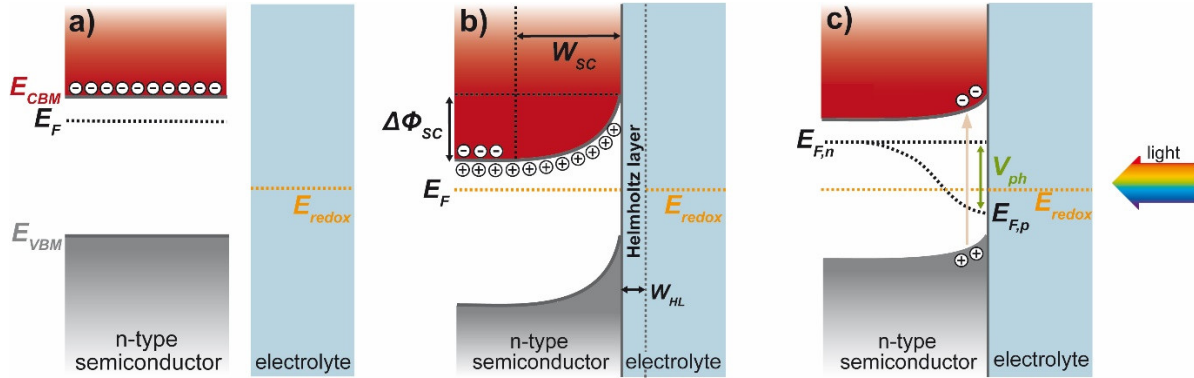


Figure 9. **a)** Energy diagrams of an isolated n-type semiconductor and electrolyte. **b)** After getting in contact, charges flow from the semiconductor to the electrolyte until the Fermi level equilibrated with redox potential of the electrolyte. As a result, a space charger layer (W_{SC}) with a potential drop (Φ_{SC}) is formed in the semiconductor. **c)** Semiconductor/electrolyte interface under operating conditions. Upon illumination, a photovoltage (V_{ph}) is generated defined as the difference between the quasi Fermi levels of the holes ($E_{F,p}$) and electrons ($E_{F,n}$).

Simultaneous with the formation of the space charge layer, a Helmholtz layer is formed when the semiconductor gets in contact with the electrolyte. Trapped charge carriers and absorbed protons or hydroxide ions at the surface of the semiconductor are counter charged by the ionized donors in the semiconductor as well as an accumulation of oppositely charged ions on the electrolyte. The Helmholtz layer is defined as the region in between the adsorbed ions at the semiconductor's surface and the nearest ions in the electrolyte. The ions in the electrolyte are surrounded by a solvation shell of (dipolar) water molecules, which explains why they cannot get too close to the semiconductor surface. The Helmholtz layer usually has a width (W_{HL}) of $\sim 2\text{--}5 \text{ \AA}$, a capacitance (C_{HL}) of $\sim 10\text{--}20 \mu\text{F cm}^{-2}$, and a potential drop inside the layer of $\sim 0.1\text{--}0.5 \text{ V}$.

The space charge layer and the Helmholtz layer act as two capacitances in series with a total capacitance (C_{tot}) given by:

$$\frac{1}{C_{tot}} = \frac{1}{C_{SC}} + \frac{1}{C_{HL}} \quad (15)$$

Because both layers are associated with the same charge and $Q = C/V$, the potential distribution is given by the following expression:

$$\frac{\Delta V_{SC}}{\Delta V_{HL}} = \frac{C_{HL}}{C_{SC}} \quad (16)$$

Since $C_{HL} \gg C_{SC}$ in most cases, any external potential applied to the semiconductor with respect to a reference electrode will fall across the space charge layer of the semiconductor (see chapter 2.2.4 for typical PEC measurement setups and methods). This implies that a positive bias potential applied to an n-type semiconductor increases the band bending (to increase the band bending of a p-type semiconductor, a negative potential has to be applied). The fact that the band bending can be changed by a bias potential is used to specify an important PEC parameter, the flatband potential (ϕ_{FB}). As indicated by the name, it is defined as the bias potential at which the bands are completely flat, i.e., no band bending is present. For semiconducting photoelectrodes, the flatband potential reflects the earliest possible photocurrent onset potential and is very important when it comes to designing tandem device for overall water splitting as will be discussed in the following chapter in detail.

Figure 9c shows the energy diagram of an n-type semiconductor immersed in an electrolyte in which electron-hole pairs are generated upon illumination. Under these conditions the system is no longer in equilibrium and the use of a single Fermi level energy is not suitable anymore. As an alternative, the concept of quasi Fermi levels is used which reflects the concentration of electrons and holes at a certain point inside the semiconductor and are defined as follows:

$$n = n_0 + \Delta n = N_C e^{-\left(\frac{E_{CBM} - E_{F,n}^*}{kT}\right)} \quad (17)$$

$$p = p_0 + \Delta p = N_V e^{-\left(\frac{E_{F,n}^* - E_{VBM}}{kT}\right)} \quad (18)$$

where n_0 and p_0 are the carrier concentration in equilibrium conditions in the dark, and Δn and Δp are the additional photogenerated carriers. The difference in the quasi Fermi levels of the electrons and holes can be interpreted as the thermodynamic driving force that is available in the system. In other words, the difference between the Fermi levels reflects the photovoltage (V_{ph}) generated upon illumination—another very important parameter for solar water splitting as will be shown in the following subchapter.

For a more detailed description of the semiconductor/electrolyte interface and other important aspects as the pH-dependence of the band edges, defect chemistry, surface states, photocurrent-voltage characteristics, etc., the readers are referred to textbooks on this topic.^[9,29]

1.3.3 Semiconductor requirements and device concepts for efficient solar water splitting

Semiconductors have to meet stringent requirements to be used as photoelectrodes in an economically viable photoelectrochemical water splitting device. Therefore, in this subchapter, these requirements are discussed and routes towards highly efficient solar water splitting devices are presented.

Figure 10 depicts the energy diagram of the simple PEC water splitting device shown in **Figure 5**. It consists of an n-type semiconductor connected to a metal counter electrode via an external circuit, both electrodes immersed in an aqueous electrolyte. Initially, sunlight shines on the semiconductor and generates electron-hole pairs and thus a photovoltage (V_{ph}) is generated. This voltage corresponds to the difference between the quasi Fermi levels of the electrons ($E_{F,n}$) and holes ($E_{F,p}$).

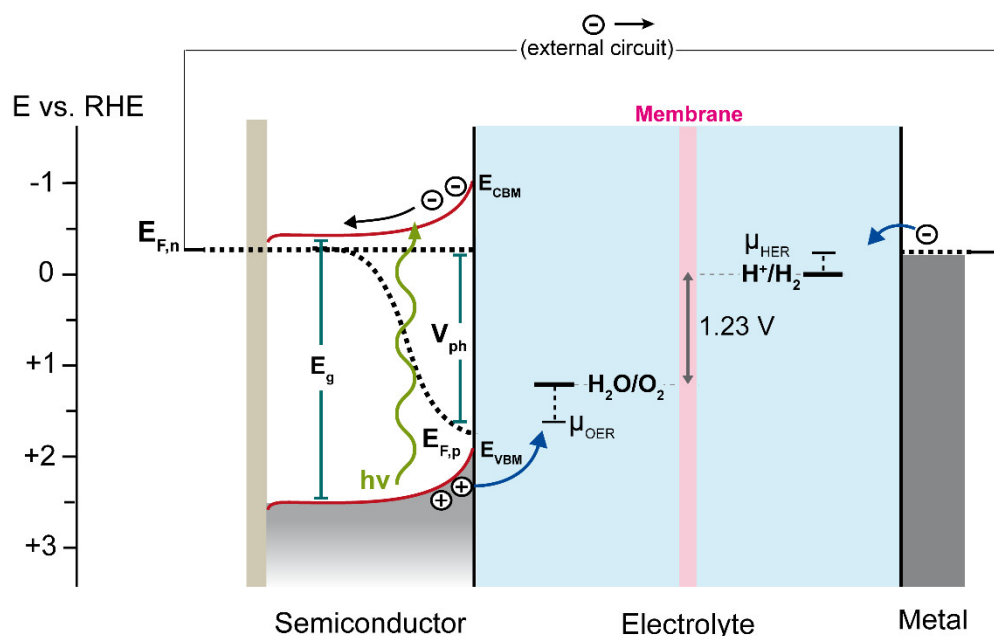


Figure 10. Energy diagram of PEC water splitting device based on an n-type semiconductor connected to a metal counter electrode via an external circuit, with both electrodes immersed in an aqueous electrolyte. Upon illumination, electron-hole pairs are generated in the semiconductor. The photovoltage (V_{ph}) equals to the difference of the quasi Fermi levels of the electrons and holes ($E_{F,n}$ and $E_{F,p}$). Due to the electric field in the space charge layer the holes are swept towards the semiconductor-liquid junction and drive the water oxidation reaction whereas the electrons in the conduction band travel to the metal counter electrode via an external circuit and drive the water reduction reaction. The membrane ensures the product separation of the two half-cell reactions.

To drive both water splitting half reactions, this photovoltage has to be at least higher than the thermodynamic standard potential of 1.23 V which corresponds to a Gibbs free energy change (ΔG) of $+237 \text{ kJ mol}^{-1}$ at RT. In practice, the photovoltage also has to provide the additional kinetic overpotentials for the oxygen (μ_{OER}) and hydrogen evolution reaction (μ_{HER}). To facilitate charge transfer from the semiconductor to the electrolyte and minimize these overpotentials, cocatalysts are usually deposited onto the semiconductor's surface. This is

especially true for photoanodes since they have to drive the OER, which is kinetically challenging because it involves four consecutive electron transfer steps. OER and HER catalysts typically require an overpotential of ~ 0.4 V and ~ 0.2 V, respectively, to generate a current density of ~ 10 mA cm⁻².^[30] As a result, the photovoltage provided by the photoelectrode should be at least ~ 1.8 V.

In addition to the photovoltage, the band positions of the semiconductor are also important parameters. The energy levels that correspond to the conduction band minimum (E_{CBM}) and the valence band maximum (E_{VBM}) can be seen as the theoretical maximum thermodynamic driving forces that can be provided by the electrons and holes, respectively. Therefore, the conduction band minimum has to be more negative than the water reduction potential and E_{VBM} more positive than the water oxidation potential. In other words, the band edges of the semiconductor have to straddle the water reduction and oxidation potentials for overall water splitting.

The considerations above lead to another important parameter of the semiconducting photoelectrode: its bandgap (E_g , i.e., the energy difference between the conduction band minimum and the valence band maximum). On the one hand, the bandgap defines the theoretical maximum obtainable photovoltage under illumination. Due to free energy losses in the semiconductor, however, the generated photovoltage is at least ~ 0.4 – 0.6 V lower than the bandgap.^[31] As a result, a semiconductor with a bandgap of ~ 2.3 eV is required to generate a photovoltage of 1.8 V needed for overall water splitting as discussed above. On the other hand, however, the bandgap also dictates the maximum photocurrent that can be generated under AM1.5 illumination since only photons with an energy of $E_{ph} > E_g$ can be absorbed. Unfortunately, this results in a trade-off between photovoltage and photocurrent in a single absorber device. To illustrate this, **Figure 11** depicts the maximum theoretical cumulative photocurrent that can be generated in a semiconductor as a function of its bandgap calculated from the AM1.5 spectrum. Assuming a Faradaic efficiency of 100% (i.e., all electron and holes generated in the photoelectrode are used for the water splitting reactions) and in the absence of an externally applied bias voltage, the solar-to-hydrogen efficiency of a water splitting device can be calculated from the photocurrent (j_{ph}) as follows:

$$\eta_{STH} = \frac{j_{ph} \cdot V_{redox}}{P_{AM1.5}} \quad (19)$$

here, V_{redox} is 1.23 V ($\Delta G = 237$ kJ mol⁻¹ at RT) and $P_{AM1.5}$ is the intensity of the AM1.5 spectrum (1000 mW m⁻²).

Based on this formula and under the assumption of a free energy loss of 0.49 eV, perfectly aligned band positions, and the current–voltage characteristics of RuO_x and Pt as an OER and HER catalyst, respectively, the maximum obtainable STH efficiency as a function of the semiconductor's bandgap can be estimated and is shown in the inset of **Figure 11**.^[31] A bandgap value of ~ 2.3 eV is found to represent the optimum trade-off between photovoltage

and photocurrent under these conditions, which translates into a STH-efficiency of ~11% for a water splitting device with a single (ideal) absorber.^[31]

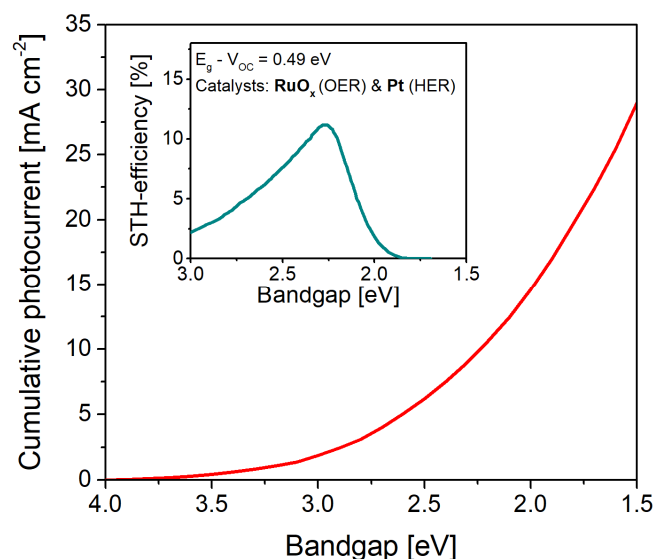


Figure 11. a) Cumulative photocurrent as a function of the bandgap of the semiconductor. Inset: STH-efficiency of a single absorber device as a function of its bandgap estimated under the assumption of an energy loss of 0.49 eV, perfect band alignment and the current–voltage characteristics of RuO_x (OER) and Pt (HER) catalysts (adapted from reference ^[31]).

Up to now, all considerations above assumed that all photons of the AM1.5 spectrum with $E_{ph} > E_g$ are absorbed and that all photogenerated charge carriers reach the back contact and the semiconductor/electrolyte interface before they recombine. Since recombination processes in photoelectrodes directly translate into efficiency losses, the charge carrier diffusion length in relation to the required film thickness needed to absorb a significant portion of the AM1.5 spectrum is a very important criterion.

Lastly, to build an economically viable water splitting device, the semiconductor has to show stable operation on the time scale of years and should consist of earth-abundant and low-cost elements.

As discussed above, the STH efficiency of a solar water splitting device consisting of single photoabsorber is limited to ~11%. To achieve higher efficiencies, at least two photoabsorbers have to be combined in a stacked tandem device. **Figure 12** shows a representative example of such a device consisting of a photoanode ($E_{g, top}$) as a top absorber and a photocathode with a smaller bandgap as a bottom absorber ($E_{g, bottom}$). The photoelectrodes are connected via an external circuit and are both immersed in an aqueous electrolyte. Upon illumination, electron-hole pairs and a photovoltage are generated in the top absorber as discussed above. In this approach, however, the transmitted photons ($E_{ph} < E_{g, top}$) are used to generate additional electron-hole pairs and a photovoltage in the bottom absorber. The photogenerated holes in the photoanode drive the OER, while the photogenerated electrons in the conduction band of the photocathode drive the HER. The

electrons in the conduction band of the photoanode travel via the external circuit to the photocathode and recombine with the holes in the valence band.

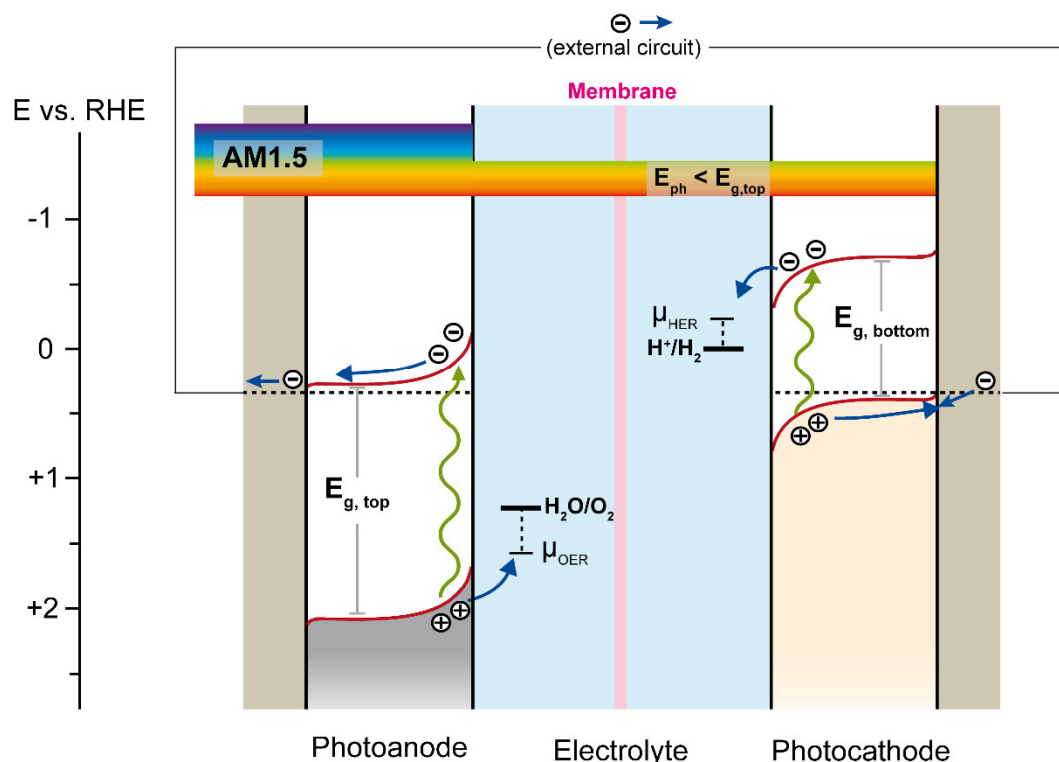


Figure 12. Schematic energy diagram of a tandem device for solar water splitting consisting of a photoanode and photocathode as a top and bottom absorber, respectively, with both electrodes immersed in an aqueous electrolyte. Upon illumination, electrons-hole pairs and a photovoltage are generated in the top absorber. The transmitted photons ($E_{ph} < E_{g, top}$) generate electron-hole pairs and a photovoltage in the bottom absorber. The photogenerated holes in the photoanode drive the OER, while the photogenerated electrons in the conduction band of the photocathode drive the HER. The electrons in the conduction band of the photoanode travel to the photocathode via the external circuit and recombine with the holes in the valence band. The membrane ensures the separation of the produced O_2 and H_2 gas.

In such a tandem device, the photovoltage of ~ 1.8 V needed for overall water splitting is provided by two semiconductors connected in series. As a result, the bandgaps of both semiconductors can be smaller than in a single absorber device, higher photocurrents can be generated and thus higher STH efficiencies can be achieved. However, the in-series connection of the absorbers also represents a challenge since the absorber that generates the smallest photocurrent will always dictate the STH efficiency. Therefore, the photocurrents in each absorber have to be matched. By considering this *current matching*, free energy losses in the semiconductors, and the overpotentials for the OER and HER, Seitz et al. estimated the STH efficiency of a dual absorber tandem device as a function of the bandgap of the top and bottom absorber (**Figure 13a**).^[31] It should be noted, that their calculations assume that all photons with $E_{ph} > E_g$ are absorbed (infinite thick absorber) and that the band edges are perfectly aligned with respect to the water oxidation and reduction potentials. It can be seen that a top absorber with a bandgap of ~ 1.7 – 1.9 eV has to be combined with a bottom absorber with a bandgap of ~ 1.0 – 1.3 eV to achieve a STH efficiency higher than 20%.

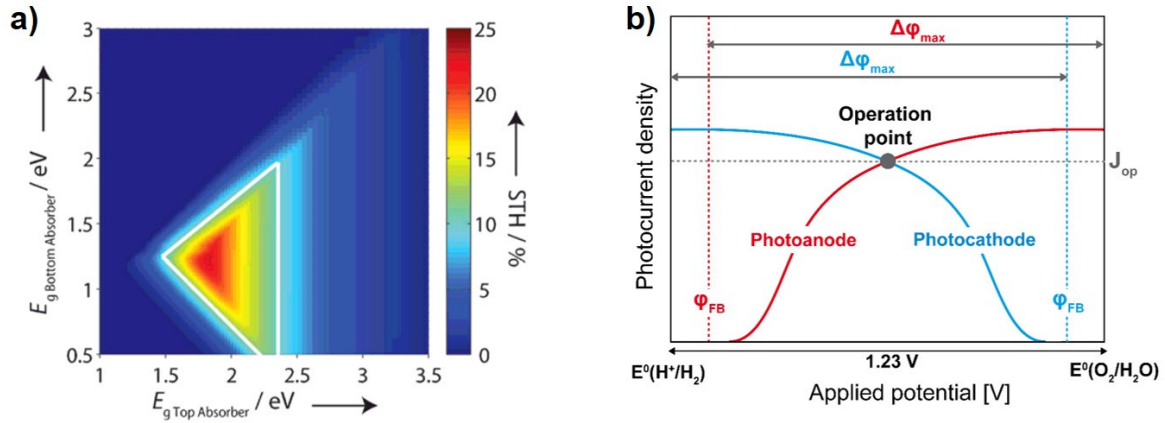


Figure 13. a) Contour plot of the solar to hydrogen efficiency of a stacked dual absorber tandem device as a function of the bandgap of the top and bottom absorber assuming a free energy loss of 0.49 eV, perfectly aligned bands and the current–voltage characteristics of Pt (HER) and RuO_x (OER) catalysts adapted from reference [31]. The white triangle indicates the area with a STH efficiency of >10%. b) Overlaid photocurrents of a photoanode and photocathode as a function of the applied potential indicating the operation point of the tandem device. The $\Delta\varphi_{max}$ values for both absorbers are illustrated.

In the tandem approach, the band positions of both semiconductors are also important parameters that define the STH efficiency. As discussed above, the operating current density (j_{op}) is determined by the overlap of the photocurrent density generated in each photoelectrode. Since the flatband potential of a photoelectrode (φ_{FB} , i.e., the applied potential at which the bands are completely flat) defines the earliest photocurrent onset potential, there should be a large difference (~ 1 V) between the flatband potentials of the photoanode and photocathode and the electrochemical potentials for the OER and HER, respectively (**Figure 13b**). This potential difference defined as $\Delta\varphi_{max}$ can be written as follows:[28]

$$\Delta\varphi_{max} = 1.23 \text{ V vs. RHE} - \varphi_{FB} \text{ (for photoanodes)} \quad (20)$$

$$\Delta\varphi_{max} = \varphi_{FB} - 0.0 \text{ V vs. RHE} \text{ (for photocathodes)} \quad (21)$$

In addition to coupling a photoanode with a photocathode (**Figure 12**), a tandem device can also be realized by combining a single photoelectrode with a photovoltaic cell as shown in **Figure 14**. In this configuration, the solar cell provides the additional photovoltage needed for overall water splitting. The combination of a wide bandgap photoelectrode ($E_g \sim 1.7\text{--}1.9$ eV) with a single junction Si solar cell is of particular interest. This is because Si has a nearly ideal bandgap of ~ 1.1 eV for the use as a bottom absorber and silicon solar cells are very cheap due to the highly developed Si solar cell technology and industry. Therefore, this approach represents an attractive tandem cell configuration towards highly efficient and low-cost solar water splitting.

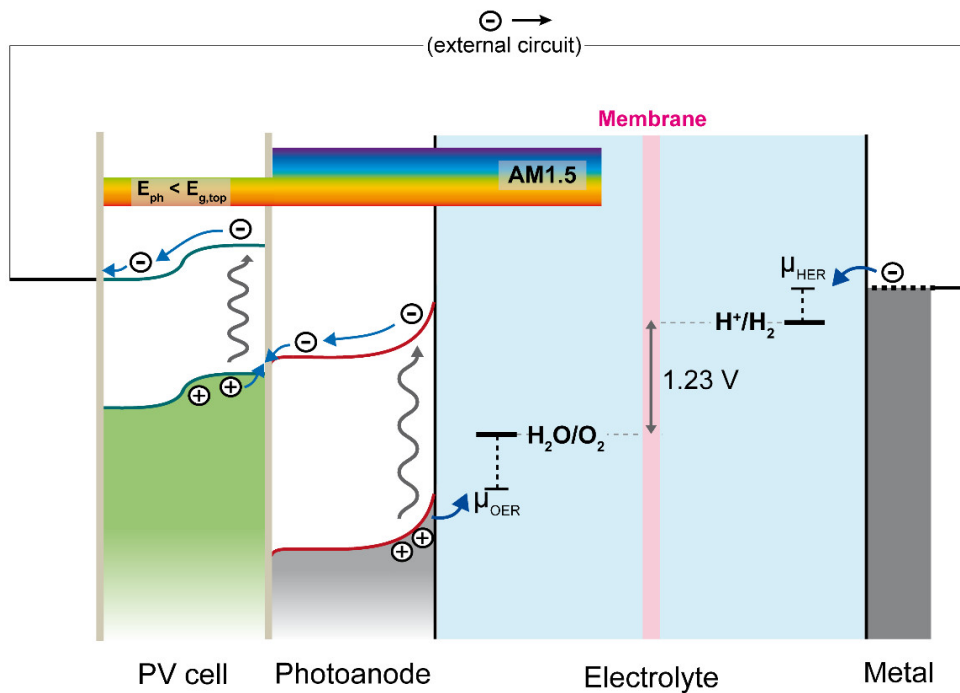


Figure 14. Schematic energy diagram of a PV-biased photoelectrochemical cell. In contrast to the tandem device consisting of two photoelectrodes (see **Figure 12**), the additional photovoltage needed for overall water splitting is provided by the PV cell.

The requirements on semiconductors to build a highly efficient photoelectrochemical solar water splitting tandem device can thus be summarized as follows:

- 1) Suitable bandgaps ($E_{g, top} = 1.7\text{--}1.9$ eV, $E_{g, bottom} = 1.0\text{--}1.2$ eV) and band positions ($\Delta\phi_{max} \sim 1$ V)
- 2) Sufficient large photovoltage generated by the semiconductor system (~ 1.8 V)
- 3) Facile charge transfer from the photoelectrode to the solution (possibly through surface functionalization with suitable cocatalysts)
- 4) Long-term stability on the time scale of years (e.g., by use of suitable protection layers)
- 5) Earth-abundant and low-cost materials

1.4 Metal oxide photoelectrodes

Due to the stringent requirements on semiconductors to be used as efficient photoelectrodes, no economically viable PEC water splitting device has been realized yet. The main bottleneck is the identification of semiconducting materials that are not only efficient, but also low-cost and highly stable (on a time scale of years). Several water splitting devices based on high quality III-V semiconductors have been reported. **Figure 15a** depicts such a device consisting of GaInP and GaInAs as a front- and bottom absorber, respectively. With a STH efficiency of 19.3%, it currently holds the world record for integrated PEC solar water splitting. However, the use of III-V semiconductors has two major disadvantages: (i) very high material costs and (ii) the inherently poor stability and hence the need of pinhole-free protection layers.

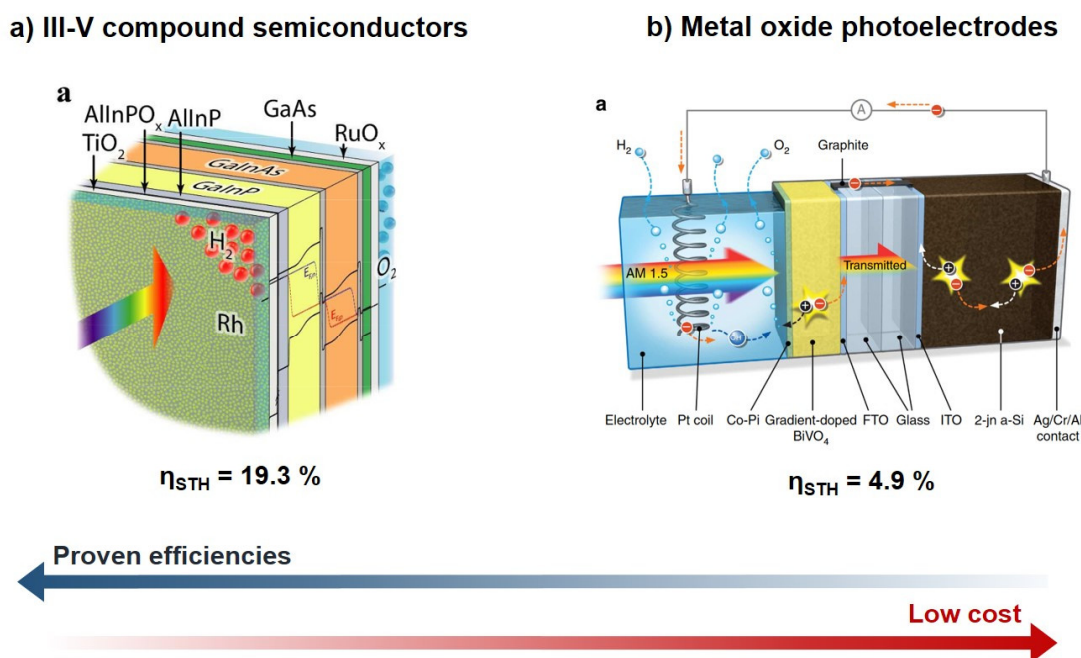


Figure 15. Device concepts for photoelectrochemical solar water splitting based on **a)** III-V compound semiconductors adapted from reference [32] and **b)** metal oxide photoelectrodes adapted from reference [33].

To avoid these disadvantages, one can also fabricate devices using earth-abundant metal oxide photoelectrodes in combination with a Si solar cell as a bottom absorber,^[33-34] or combine two metal oxides in an all-oxide device.^[35-36] An example of such a device is shown in **Figure 15b** consisting of an n-type BiVO₄ photoelectrode combined with a double junction Si solar cell. Compared to III-V semiconductors, the major advantage of metal oxides is their potentially lower cost and their generally higher stability in aqueous electrolytes. For example, stable operation of > 1000 h under AM1.5 illumination has been demonstrated for a α-Fe₂O₃ (hematite) photoanode.^[37] However, PEC solar water splitting devices based on metal oxide photoelectrodes usually show moderate STH efficiencies; the highest efficiencies reported so far are just below 8%.^[33,38-39] This is usually caused by the combination of a poor

charge carrier transport and a modest light absorption resulting in a mismatch between the charge carrier diffusion length and the film thickness needed to absorb a significant portion of the AM1.5 spectrum. In contrast to covalent semiconductors that can reach charge carrier mobilities of $> 1000 \text{ cm}^2 \text{ V}^{-1} \text{ s}^{-1}$ ^[40], metal oxides typically have carrier mobilities in the range between $0.001 - 0.1 \text{ cm}^2 \text{ V}^{-1} \text{ s}^{-1}$. This poor charge carrier transport is typically caused by polaron hopping transport mechanisms^[41-42] and point defects that introduce deep energy levels in the bandgap acting as recombination centers.

However, the poor charge carrier transport properties of metal oxides is not believed to be a show-stopper since it can be overcome by several strategies already shown in the literature: (i) doping with metal ions was shown to increase the carrier concentration and therefore the conductivity;^[33,43-45] (ii) H_2 -treatments were found to not only increase the conductivity of n-type metal oxides by the formation of oxygen vacancies as shallow donors,^[46] but also increase the charge carrier lifetime by passivation of defect states;^[47] (iii) high-temperature treatments of metal oxides were shown to improve the crystallinity and reduce the concentration of point defects;^[48-49] (iv) preferentially oriented films along the crystal axis with the highest intrinsic mobility can drastically increase the effective carrier diffusion length;^[50] and (v) nanostructuring was shown to decouple (“orthogonalize”) light absorption and charge transport.^[51] In addition, the preparation method of complex metal oxide photoelectrodes plays a crucial role in determining their charge carrier transport properties. Solution synthesis methods, such as spray pyrolysis, drop casting or electrodeposition, tend to create non-crystalline phases or intrinsic point defects. In contrast to this, UHV-based processes such as pulsed laser deposition (PLD) as used in this thesis are capable of producing compact metal oxide films with a high electronic quality (see chapter 2.1.1).

Among the group of the simple binary oxides, n-type $\alpha\text{-Fe}_2\text{O}_3$ (hematite) has a suitable bandgap of $\sim 2.1 \text{ V}$ and excels in stability.^[37] However, its photoelectrochemical performance is still limited by a poor charge carrier transport in the bulk.^[52] p-type Cu_2O also has the right bandgap of 2.0 eV , but photocorrosion is a major issue with this material. However, its stability was greatly enhanced by the introduction of protection layers (e.g., TiO_2) using Atomic Layer Deposition (ALD).^[53-54] Recently, Pan et al. reported on nanostructured $\text{Cu}_2\text{O}/\text{Ga}_2\text{O}_3/\text{TiO}_2/\text{RuO}_x$ photocathodes that produced a photocurrent density of 10 mA cm^{-2} at a potential of 0 V vs. RHE and a stable operation of $> 100 \text{ h}$ at $E = 0.5 \text{ V}$ vs. RHE).^[35] Due to the lack of other suitable binary oxides, *multinary* metal oxides have become the focus of current research in the field. Considering the number of metals in the periodic system, there are roughly 8.000 different ternary and 700.000 different quaternary metal oxide candidates.^[28] Of those many potential candidates, however, only a small fraction has been characterized in detail. Therefore, high-throughput combinatorial studies and DFT calculations are also the subjects of ongoing research to identify new materials.^[55-62] Recently

explored multinary metal oxide classes are for example vanadates^[56,59] (e.g., BiVO_4 ^[28,63], FeVO_4 ^[64], $\gamma\text{-Cu}_3\text{V}_2\text{O}_8$ ^[65]), spinels (e.g., CaFe_2O_4 ^[66], ZnFe_2O_4 ^[67]), tungstates^[61-62] (e.g., CuWO_4 ^[68], Fe_2WO_6 ^[69]), and delafossites (e.g., CuFeO_2 ^[70]).

Figure 16 depicts an overview of complex metal oxide photoelectrode candidates showing their maximum obtainable photocurrent density ($j_{\text{max, AM1.5}}$; calculated from the bandgap) vs. their $\Delta\phi_{\text{max}}$ values (see chapter 1.3.3 for their definitions).^[28] The metal oxides in the green area in the plots represent the most promising photoelectrode materials. This is because they cannot only achieve high AM1.5 photocurrent densities but also have a large $\Delta\phi_{\text{max}}$ of $\sim 1\text{V}$, so that the combination with a single junction Si solar is sufficient for overall water splitting. For the p-type metal oxides, materials like CuBi_2O_4 , CuFeO_2 (**Figure 16a**) are promising candidates. For these materials the challenge is now to further identify and understand their performance limiting factors and push the still relatively low HER photocurrents (1.0 mA cm^{-2} at 0.0 V vs RHE ^[71] and 2.4 mA cm^{-2} at 0.4 V RHE ^[72] for CuBi_2O_4 and CuFeO_2 , respectively) closer to the theoretical maximum value. For the n-type photoanode candidates, SnWO_4 stands out due to its combination of a high $j_{\text{max, AM1.5}}$ and a large $\Delta\phi_{\text{max}}$ (**Figure 16b**). This material, however, is at an early stage of its development and there is a lack of knowledge of fundamental PEC key properties, such as the charge carrier mobility and lifetime.

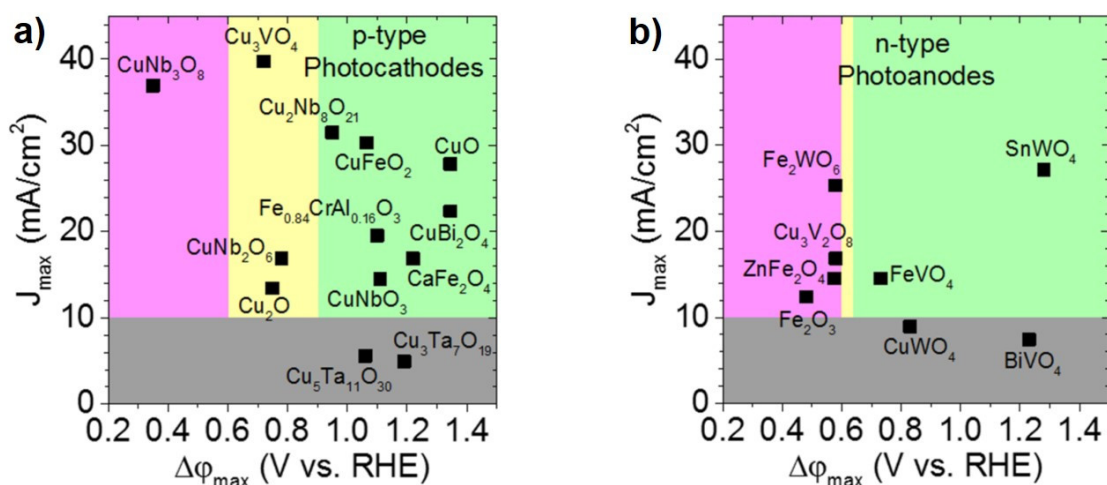


Figure 16. Maximum theoretical AM1.5 photocurrent (defined by the bandgap) vs. $\Delta\phi_{\text{max}}$ of **a)** p-type and **b)** n-type complex metal oxide photoelectrode materials adapted from reference^[28]. Grey areas indicate a $j_{\text{max, AM1.5}} < 10\%$. The colored areas indicate the most suitable tandem configuration for the respective photoelectrode material. (Magenta \triangleq photocathode/–anode or single junction Si; yellow \triangleq photocathode/–anode or multi junction Si; and green \triangleq multijunction Si)

1.4.1 BiVO_4

Bismuth vanadate (BiVO_4) is a remarkable example for the development of a ternary metal oxide photoelectrode. Since the discovery of its photoactivity by Kudo et al. in 1998^[73],

BiVO_4 attracted a huge amount of interest in the field of solar water splitting. Nowadays, it is the most well-studied and therefore also one of the highest performing metal oxide photoanodes (~2100 publications on BiVO_4 since 1998; keyword BiVO_4 and *photo** in the web of science database). Due to established general concepts (e.g., gradient-doping^[33] or surface state passivation^[74]) developed with BiVO_4 , it has also been used as a platform for the accelerated discovery and development of other complex oxide photoelectrode materials.^[63]

BiVO_4 has three different crystal structures: pucherite, dreyerite and clinobisvanate. The latter one has a monoclinic (scheelite-type) crystal structure (space group $C2/c$, $a = 7.247 \text{ \AA}$, $b = 11.697 \text{ \AA}$, $c = 5.09 \text{ \AA}$, and $\beta = 134.226^\circ$) as shown in **Figure 17a** and is the most photoactive phase.^[75] Its structure consists of distorted BiO_8 dodecahedra and VO_4 tetrahedra in which each O atom is coordinated to two Bi centers and one V center. The electronic structure of clinobisvanate, determined by Cooper et al. through a combination of density functional theory (DFT) calculations and advanced spectroscopic analysis, is shown in **Figure 17b**.^[76] The valence band maximum and the conduction band minimum were found to be mostly comprised of O 2p and V 3d orbitals, respectively. The indirect bandgap of clinobisvanate BiVO_4 has been reported to be ~2.4–2.5 eV.^[76-78] while at higher energies, a direct transition occurs ($E_{g, \text{direct}} \sim 2.6\text{--}2.7 \text{ eV}$). The n-type conductivity of BiVO_4 is believed to arise from hydrogen impurities and oxygen vacancies acting as donor-dopants.^[79]

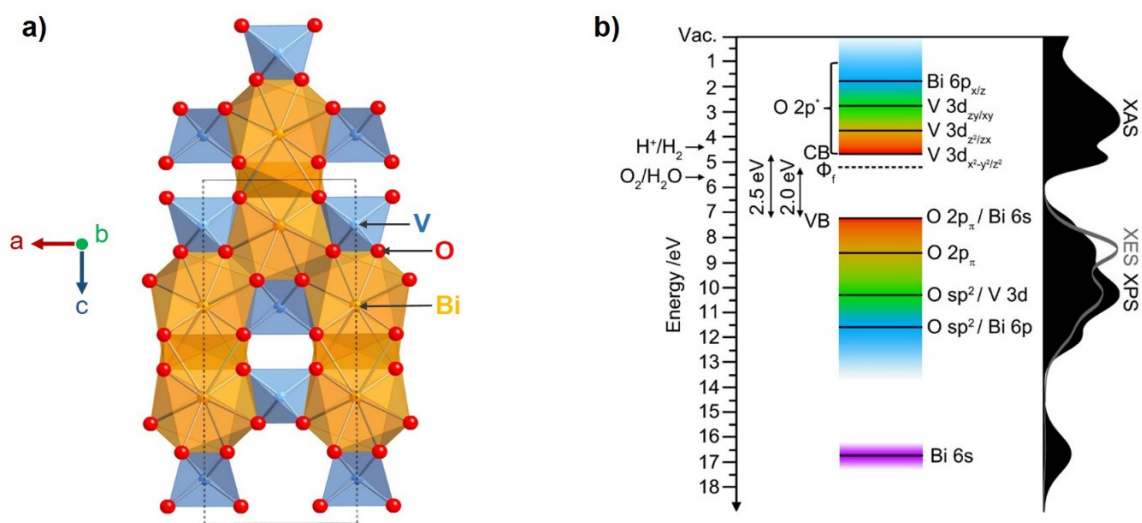


Figure 17. **a)** Crystal structure of monoclinic BiVO_4 (clinobisvanite) shown along the (b -axis). Oxygen, vanadium and Bi ions are colored in red, blue and yellow, respectively. **b)** Electronic band structure of monoclinic BiVO_4 (clinobisvanite) as obtained by DFT calculations as well as X-ray absorption spectroscopy (XAS), X-ray emission spectroscopy (XES) and X-ray emission spectroscopy (XPS) measurements adapted from reference^[76].

In the late 1990s and the beginning of 2000s, the photocurrents reported for BiVO_4 photoelectrodes were relatively small ($< 1 \text{ mA cm}^{-2}$) compared to the theoretical AM1.5 limit of 7.5 mA cm^{-2} defined by its bandgap.^[28,80] This changed, however, when the performance limiting factors of the material were identified and investigated in detail. One limitation was

found to be a slow hole transfer from the semiconductor surface to the electrolyte.^[33,80-83] To compensate this, several surface modification layers, for example CoPi^[33,81] or FeOOH/NiOOH,^[82] have been deposited on the surface. These layers not only lead to an increase of the catalytic activity towards the OER^[84], but also passivate surface states and hence reduce surface state recombination, as suggested by recent studies.^[74] Another limitation in BiVO₄ was the poor charge carrier transport resulting from a small polaron hopping conduction mechanism typical for metal oxide photoelectrodes as discussed above.^[42,85-86] To address this issue, several strategies have been pursued. Cation doping with W⁶⁺ and Mo⁶⁺ was found to increase the carrier concentration and thus the conductivity of BiVO₄ thin films.^[33,43,87-88] A hydrogen treatment was found to increase the effective charge carrier lifetime and thus the charge carrier diffusion length via a reduction or passivation of deep trap states.^[47] In addition, nanostructured photoelectrodes^[82] and guest-host (heterojunction) nanostructures^[89-91] were fabricated to orthogonalize the direction of charge transport and the optical absorption. With this strategy the distance that the carriers have to travel can be kept short by keeping the film thin without compromising the amount of absorbed photons. In addition, plasmonic resonators, such as Ag@SiO₂, were deposited on top of BiVO₄ films to increase the light absorption.^[92-93]

By combining several of these strategies, Pihosh et al. achieved an AM1.5 photocurrent of 6.72 mAcm⁻² at a potential of 1.23 V vs. RHE under one sun illumination with core-shell WO₃/BiVO₄ nanorods modified with CoP₁ in 2015.^[51] This is close to the theoretical maximum value of 7.5 mA cm⁻². This result shows that it is indeed possible to obtain high efficiencies with earth-abundant and low-cost metal oxide photoelectrodes. However, nanostructured photoelectrodes also have disadvantages, especially for the design of the tandem solar water splitting device, as light tends to be highly scattered by these type of photoelectrodes. Pihosh et al. were required to use a highly efficient GaAs/InGaAsP solar cell at an angle of 45° in *front* of the BiVO₄ to utilize the diffusely back-reflected light from the nanorods and to generate the bias voltage needed for overall water splitting.^[51] A non-scattering top absorber is required to build a more practical stacked tandem device.

1.4.2 α -SnWO₄

Tin tungstate (SnWO₄) recently attracted attention as a semiconducting photoelectrode material for solar water splitting. Compared to BiVO₄, it has not yet been studied in great detail (~34 publications in total of which only a small fraction studied SnWO₄ as a light absorber; keyword *SnWO₄* in the web of science database). SnWO₄ has two polymorphs: cubic β -SnWO₄ and orthorhombic α -SnWO₄. The former structure is stable at temperatures > 670°C and can be synthesized by rapid quenching to room temperature after calcination above this temperature.^[94] The bandgap of β -SnWO₄ is reported to be rather large ($E_g = 4.1$ eV) which makes it of no interest for the application as a photoabsorber in solar water splitting.^[95]

The low-temperature polymorph α -SnWO₄, however, is much more interesting. It has an orthorhombic crystal structure (space group *Pnna*, $a = 5.625 \text{ \AA}$, $b = 11.744 \text{ \AA}$, $c = 4.986 \text{ \AA}$) consisting of layers of SnO₄ tetrahedra and WO₆ octahedra in the b direction (**Figure 18a**). The indirect bandgap of α -SnWO₄ is reported to be $\sim 1.5\text{--}2.1 \text{ eV}$ making it a potential candidate to be used as a top absorber in a highly efficient tandem device (see **Figure 13a**). As suggested by DFT calculations by Ziani et al., the valence band of α -SnWO₄ is composed of Sn 5s and O 2p orbitals, while the W 5d orbitals mainly contribute to the conduction band.^[96] The material shows n-type conductivity which is believed to result from oxygen vacancies acting as electron donors.^[97] Its flat band potential has been reported to be $-0.1\text{--}0.0 \text{ V vs. RHE}$, suggesting that the conduction and valence bands nicely straddle the oxygen and hydrogen evolution potentials.^[96-98]

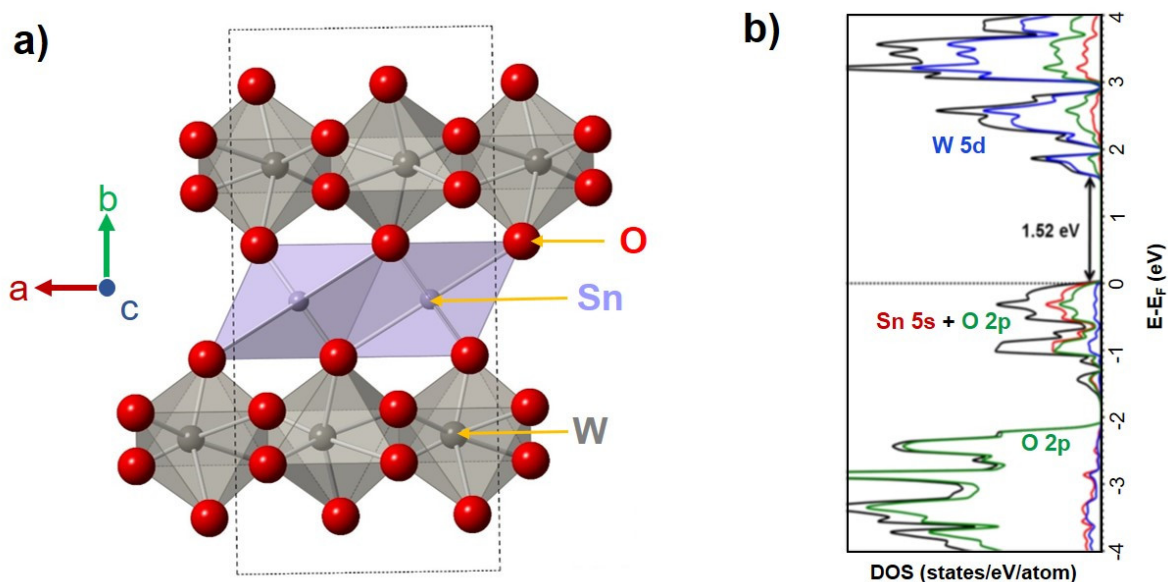


Figure 18. **a)** Crystal structure of orthorhombic α -SnWO₄ shown along the (c -axis). O, Sn, and W ions are colored in red, purple and gray, respectively. **b)** DFT calculation of the density of states (DOS) of α -SnWO₄ adapted from reference ^[98].

The photoelectrochemical performance of α -SnWO₄, however, is reported to be relatively low. AM1.5 photocurrents of only $\sim 0.1 \text{ mA cm}^{-2}$ were reported in acidic and neutral electrolytes.^[96-97,99] This poor performance was attributed to the oxidation of Sn²⁺ to Sn⁴⁺ at the surface forming electron trap sites^[96], impurity phases in the bulk^[97], and hole trapping at Sn-at-W antisite defects within the band gap^[97]. The exact reasons for its poor performance have not been fully elucidated yet since many PEC key parameters, such as the charge carrier diffusion length, are not yet known.

1.5 This thesis

Even though great progress in photoelectrochemical solar water splitting has been made in the past decades, the commercialization potential of this approach is still uncertain. As discussed above, the main bottleneck is the identification of photoelectrode materials that are not only efficient, but also low-cost and stable on a time scale of years. The objective of this work is to produce and investigate compact and high-quality films of two promising photoelectrode materials: BiVO_4 and $\alpha\text{-SnWO}_4$. To ensure that these films have the highest electronic quality possible, pulsed laser deposition is used to fabricate the films. To understand the performance limitations of these materials, their properties are investigated with a variety of photoelectrochemical and other spectroscopic techniques.

In Chapter 3, the pulsed laser deposition process of efficient BiVO_4 photoelectrodes is elucidated. First, the different steps of this rather complex process, i.e., (i) target ablation, (ii) expansion of the plasma plume and (iii) film condensation are discussed with respect to deviations from an ideal stoichiometric-target-to-substrate transfer. Based on this, a straightforward approach for the fabrication of compact and stoichiometric BiVO_4 thin films with a high photoactivity is demonstrated. The importance of tailoring the PLD process parameters is emphasized by correlating them with the charge carrier transport properties measured with time-resolved microwave conductivity (TRMC) and the PEC performance of the deposited films. Finally, the alternating ablation of Bi_2O_3 and V_2O_5 targets is presented as an effective alternative method to control the stoichiometry and to prepare efficient BiVO_4 photoelectrodes.

Chapter 4 contains a comprehensive evaluation of the new photoelectrode material $\alpha\text{-SnWO}_4$. Initially, the PLD process is optimized with respect to the phase-purity of the films. The nearly-ideal bandgap of 1.9 eV for $\alpha\text{-SnWO}_4$ and the suitability of its band positions for use as a top absorber in a tandem device as reported in literature are confirmed. For the first time, the charge carrier mobility of $\alpha\text{-SnWO}_4$ is measured. It is shown that the mobility can be increased by more than two orders of magnitude by a controlled high-temperature treatment, resulting in a relatively high effective charge carrier diffusion length. In addition, by combining time-resolved microwave conductivity (TRMC) and time-resolved terahertz spectroscopy (TRTS), it is shown that this improvement is caused by larger grain/domain sizes in the heat treated films and that grain boundaries are limiting the charge carrier transport in $\alpha\text{-SnWO}_4$. In addition, a hole-conducting pulsed laser deposited NiO_x layer is introduced that protects the surface of $\alpha\text{-SnWO}_4$ from oxidation and thereby drastically improves the AM1.5 sulfite oxidation photocurrent from several $\mu\text{A cm}^{-2}$ to a record value of 0.75 mA cm^{-2} .

Chapter 2 – Methods & experimental section

2.1 Sample preparation

2.1.1 Pulsed laser deposition of metal oxides

In this thesis, pulsed laser deposition (PLD) is used for the preparation of thin films of BiVO_4 and $\alpha\text{-SnWO}_4$. This physical vapor deposition technique was first introduced by Smith and Turner in 1965 to deposit thin films in vacuum.^[100] However, it didn't achieve its breakthrough until the year of 1987 in which Dijkkamp et al. published their work on the successful pulsed laser deposition of superconducting $\text{Y}_1\text{Ba}_2\text{Cu}_3\text{O}_{7-x}$ (YBCO) by ablating a stoichiometric target.^[101] Since then, PLD attracted a lot of interest and was widely used in the deposition of, for example, superconductors, garnet thin films, and metal oxides/nitrides.^[102]

Figure 19a shows a schematic drawing of a pulsed laser deposition system consisting of a target carousel, a heatable substrate holder unit in a vacuum chamber (both usually equipped with a scanning system), and a high power pulsed laser (typically KrF-Excimer or Nd:YAG^[103]). In addition, PLD systems are commonly equipped with gas inlets to add for example an oxygen, argon or hydrogen background pressure during the deposition.

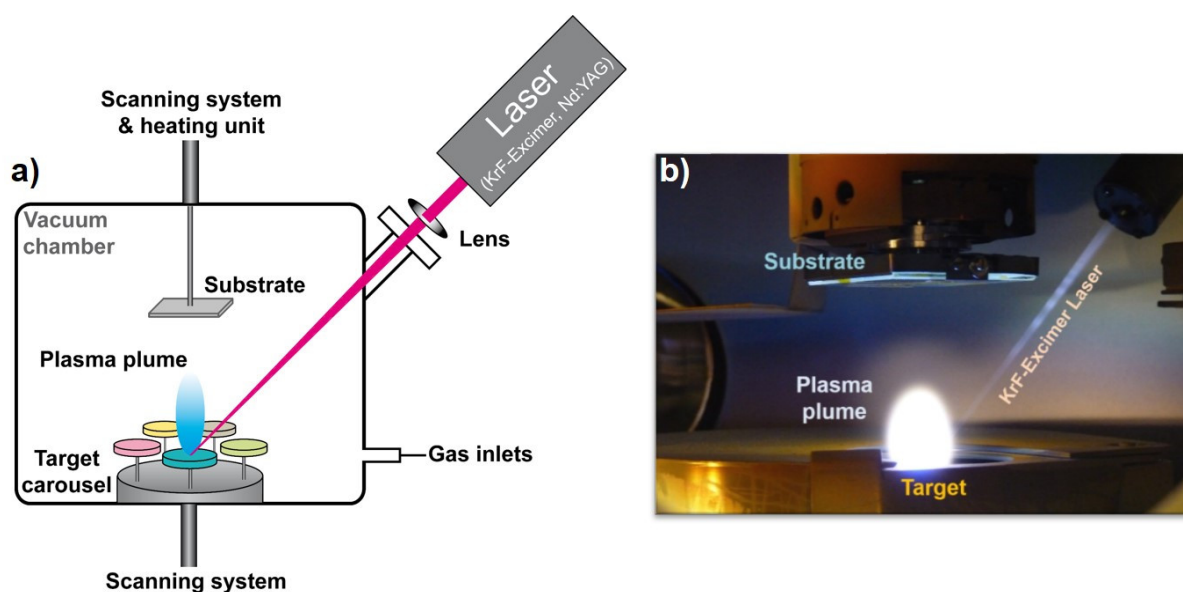


Figure 19. a) Schematic drawing of a PLD system consisting of a target carousel and a heatable substrate holder both equipped with a scanning system in a vacuum chamber. A high power pulsed laser (typically KrF-Excimer or Nd:YAG) is focused on a target resulting in the ablation of the material. Partially ionized by the laser, the ablated species form a luminous plasma plume that expands away from the target and are collected on a substrate, on which a thin film is grown. During the deposition gas inlets allow the use of different background pressures such as oxygen, argon or hydrogen. **b)** Optical photograph of our PLD chamber from PREVAC (Poland).

But what makes the PLD technique so unique and special? The answer can be found in the special deposition conditions. Initially, a short high power laser pulse is focused on a target material in a vacuum chamber with repetition rates typically between 1 and 100 Hz. Due to the high fluence (energy per area) of the laser pulse, typically in the range of $1 - 5 \text{ J cm}^{-2}$, the surface of the target can heat up to more than 5000 K with a heating rate of

about 10^{12} K/s.^[104] Such temperatures are well above the temperature typically required for thermal evaporation and the pulse is too short to establish a thermal equilibrium. As a result, all atoms in the excited volume are ablated and a stoichiometric target-to-substrate transfer can be achieved. Partially ionized by the laser, the ablated species form a luminous plasma plume that expands rapidly away from the target surface and are collected on a substrate (**Figure 19b**). This ion-assisted deposition allows the formation of dense and compact films due to the high kinetic energy of the ablated species (typically in the range of several hundred eV) and the pulsed nature of the deposition. Specifically, the short laser pulses (~25 ns) result in a high supersaturation of the species that arrive at the substrate surface which leads to the formation of a large number of nucleation sites and hence promotes layer-by-layer growth of the film.^[105-106] Furthermore, PLD facilitates the use of high purity target materials as compared to solution-based thin film processing (e.g., spray pyrolysis). Another advantage of PLD is the possibility to change the target material during deposition when the system is equipped with a target carousel. For instance, a complex metal oxide can be prepared by the alternating ablation of the respective binary metal oxide targets while the stoichiometry is controlled by the number of shots on each target.^[107-108] All of this makes this technique well-suited for the preparation of high-quality metal oxide photoelectrodes to investigate their fundamental photoelectrochemical and opto-electronic properties and to identify their performance limiting parameters. Especially for multinary metal oxides, the stoichiometric target-to-substrate transfer is highly beneficial since small deviations in the stoichiometry can lead to large defect densities and poor electronic quality.

PLD, however, is also a very complex process. The stoichiometric target-to-substrate transfer as described above cannot always be achieved for all multicomponent material systems and the deposition parameters such as the fluence, oxygen background pressure, and substrate temperature usually have to be carefully tailored to get the desired phase.^[105] For example, a preferential ablation of the most volatile element in a multicomponent target can occur when the chosen laser fluence is too low.^[105,109] In addition, other factors such as element-dependent thermalization, scattering of the ablated species with the background gas, and re-sputtering/re-evaporation effects from the substrate, may also result in a non-stoichiometric target-to-substrate transfer.^[21,105,109-110]

2.1.2 Target preparation

Complex metal oxide targets were prepared from the respective binary oxide powders by traditional ceramic methods. A mortar and grinding ball (Fritsch) consisting of ZrO_2 were used with a ball mill (FRITSCH Pulverisette) to grind and mix the powders (**Figure 20a**). The mixed powders were pressed into a pellet in a pressing tool with a diameter of 30 mm (P/O/WEBER, Modell 10, **Figure 20b**) using a hydraulic press (P/O/WEBER, Modell PW 20) with a pressing force of ~100 kN (~0.14 GPa). If required, the pressing tool was put into a homebuilt vacuum recipient connected to a fore pump to ensure a sufficient release of air

before and during the pressing (**Figure 20c**). The sintering process of the pellets was performed in a tube furnace in an Al_2O_3 sintering tray.

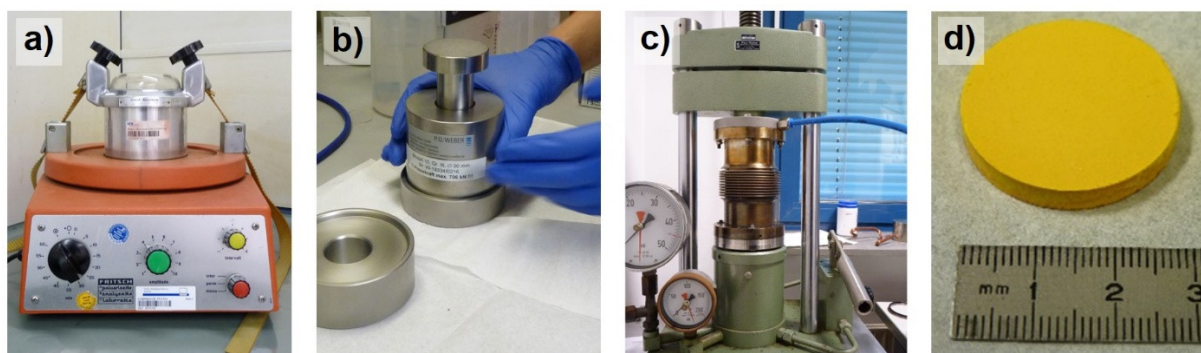


Figure 20. Overview of the target preparation. **a)** Ball mill used for grinding and mixing of powders. **b)** Pressing tool used for pressing the powders into a pellet. **c)** Hydraulic press with the homebuilt vacuum recipient. **d)** Finished BiVO_4 target.

The BiVO_4 target was prepared by mixing Bi_2O_3 (99.9995%, Alfa Aesar) and V_2O_5 (99.995%, Alfa Aesar) with an atomic ratio of 1:1. A pellet was pressed in vacuum and sintered at 700°C for 12 h in air to drive the solid state reaction. Subsequently, the pellet was ground and pressed into a pellet again, and finally sintered at 850°C for 12 h in air. The density of the target was $\sim 82\%$, calculated using the theoretical density of monoclinic BiVO_4 (6.95 g cm^{-2}).

The $\alpha\text{-SnWO}_4$ target was prepared by equimolar amounts of SnO (99.9%, Alfa Aesar) and WO_3 (99.99%, Alfa Aesar). The pressed pellet was sintered at 700°C for 10 h in an argon atmosphere to prevent the oxidation of Sn^{2+} to Sn^{4+} . This process was repeated five times until the target showed a nearly pure $\alpha\text{-SnWO}_4$ phase. Prior to the each sintering, the tube was evacuated ($< 10^{-3}$ mbar) and flushed with Ar for two times to further reduce the risk of oxidation.

2.1.3 Fabrication of BiVO_4 films

BiVO_4 films were prepared by pulsed laser deposition in a custom-built system (PREVAC) equipped with a 248 nm KrF-excimer laser (LPXpro 210, Coherent). Two different approaches were used: (i) ablation of a single-phase BiVO_4 target and (ii) alternating ablation of commercial Bi_2O_3 (99.9%, FHR) and V_2O_5 targets (99.99%, FHR). All depositions were performed after a pre-ablation with the respective laser fluences until a constant deposition rate measured with a quartz crystal microbalance (QCM) was achieved. Fluorine-doped tin oxide (FTO) glass (TEC 7, Pilkington), glassy carbon (Sigradur G, HTW) and quartz glass (Spectrosil 2000, Baumbach & Co Ltd.) were used as substrates. Prior to deposition all substrates were ultrasonically cleaned in isopropanol for 10 min, rinsed with demineralized water and dried under compressed nitrogen. During the deposition, the substrate was positioned off-axis (distance of 12 mm from the plume center) and rotated with an angular

velocity of 12° s^{-1} . The depositions were carried out with a repetition rate of 10 Hz. The thickness of the films was adjusted by the total number of laser pulses and measured with a DEKTAK profilometer. The FTO substrate temperature (T_{sub}) was calibrated with a thermocouple attached to the surface of the FTO.

CoPi catalyst deposition:

CoPi was photo-electrochemically deposited onto the surface of the BiVO₄ films in a PEC setup as described in chapter 2.2.4 in detail. The deposition solution was prepared by dissolving 0.5 mM Co(NO₃)₂·6H₂O (99%, ACROS Organics) in a 0.1 M KP_i (pH 7) buffer solution. The photo-assisted electrodeposition was carried out at a constant potential of 1.1 V vs. RHE for 270 s under backside AM1.5 illumination.

2.1.4 Fabrication of α -SnWO₄ films

α -SnWO₄ films were deposited by ablating an α -SnWO₄ target in the same PLD system and geometry as described above. The thickness of the films was adjusted by the total number of laser pulses. After the deposition, the films were annealed in a tube furnace in an argon atmosphere. The films were deposited on FTO-coated glass substrates (TEC 7, Pilkington) for PEC characterization and on quartz substrates (Spectrosil 2000, Baumbauch LTD) for TRMC, TRTS and UV/VIS analysis. The substrates were ultrasonically cleaned in a 1 vol.% Triton solution (Triton X-100, laboratory grade, Sigma Aldrich), D.I. water, and ethanol ($\geq 99.99\%$, Sigma-Aldrich) for 15 min in each solution, followed by drying under a stream of compressed nitrogen.

NiO_x protection layer:

NiO_x protection layers (~20 nm) were pulsed laser deposited onto α -SnWO₄ films by ablating a Ni target (99.99%, Alfa Aesar) at room temperature with a fluence of 2 J cm^{-2} , an oxygen background pressure of 5×10^{-2} mbar and a target-to-substrate distance of 60 mm. The thickness of the protection layer was controlled with the number of pulsed laser shots on the target.

2.2 Analysis methods

2.2.1 Rutherford backscattering spectrometry (RBS)

Rutherford backscattering spectrometry (RBS) is a powerful and standard-free method to determine the quantitative elemental composition and depth distribution of thin films. In this technique, light ions (usually He^{4+}) are accelerated to an energy in the range between 1–3 MeV and are focused on the specimen in a vacuum chamber. The energy distribution and the yield of the elastically backscattered ions are measured at a certain angle (**Figure 21a**).

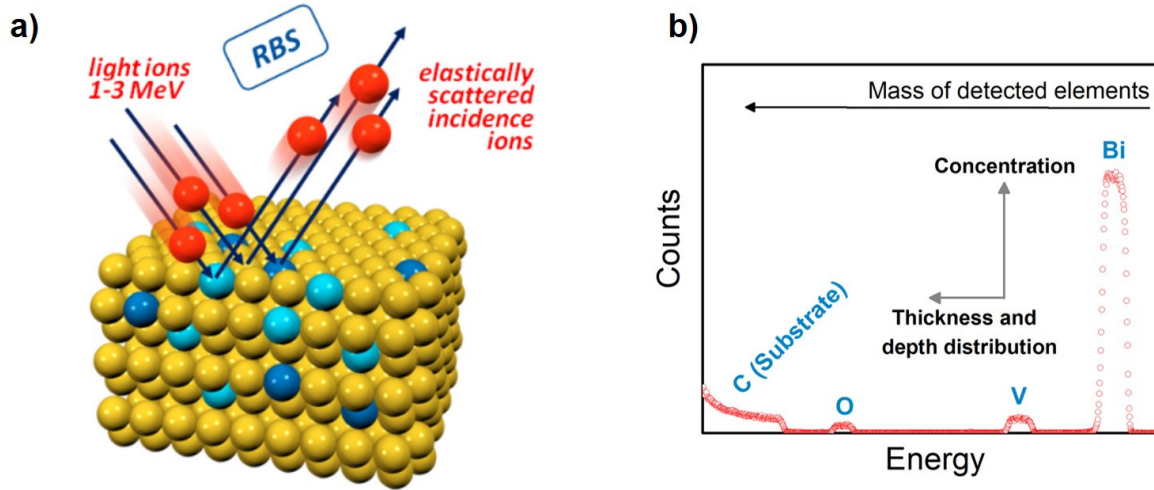


Figure 21. **a)** Schematic representation of Rutherford backscattering spectrometry (RBS) analysis adapted from reference [111]. Light ions are accelerated (1–3 MeV) and focused on the specimen in a vacuum chamber while measuring the energy distribution and yield of the elastically backscattered ions at a certain angle. **b)** Typical RBS spectrum of a thin film (in this case BiVO_4) on a glassy carbon substrate. The height of the signal determines the concentration of the element in the films whereas the width of the signal provides information about the film thickness and the depth profile.

The energy of the scattered projectile (E_1) is reduced from its initial energy (E_0) by $E_1 = kE_0$, where k is called the kinematic factor and is given by the following expression:

$$k = \left[\frac{\sqrt{(M_2^2 - M_1^2 \sin^2 \theta_{SC})} + M_1 \cos \theta_{SC}}{M_2 + M_1} \right]^2 \quad (22)$$

Here, θ_{SC} is the scattering angle and M_1 and M_2 are the masses of the projectile and the atom in the specimen, respectively. The differential cross section σ_R for Rutherford backscattering is given by the following expression:

$$\sigma_R \left[\frac{mb}{sr} \right] = 5.1837 \times 10^6 \left(\frac{Z_1 Z_2}{E [keV]} \right)^2 \frac{\left(\sqrt{(M_2^2 - M_1^2 \sin^2 \theta_{SC})} + M_2 \cos \theta_{SC} \right)^2}{M_2 \sin^4 \theta_{SC} \sqrt{(M_2^2 - M_1^2 \sin^2 \theta_{SC})}} \quad (23)$$

where Z_1 and Z_2 are the atomic numbers of the projectile and the atom in the specimen, respectively.

Based on these equations and considering other effects such as the stopping power (inelastic scattering losses) of the projectile in the specimen and the surface roughness, the obtained spectra can be fitted (for example with the SIMNRA software) and the elemental composition of the film can be quantified. **Figure 21b** shows an example RBS spectrum of a thin film on a light substrate (in this case BiVO_4 on glassy carbon). The signals of the heavier elements appear at higher energies due to the considerations discussed above. The inelastic scattering processes of the projectiles in the specimen result in a broadening of the signals and therefore provides additional information about the film thickness and the depth distribution of elements.

Experimental details:

In this thesis, the elemental composition of the BiVO_4 and $\alpha\text{-SnWO}_4$ films deposited on glassy carbon substrates was determined by RBS with He^{4+} ions ($E_0 = 1.7 \text{ MeV}$) as projectiles. The energy distribution of the backscattered ions was measured at a scattering angle of 165° . The obtained spectra were analyzed with the SIMNRA software.

2.2.2 X-ray diffraction (XRD)

X-ray diffraction (XRD) is used to determine the crystal structure of materials. In this method, incident X-rays are scattered by the atoms of the specimen. A regular array of atoms—as can be found in a crystalline material—results in a regular array of scattered spherical X-ray waves that interfere with each other. The condition for a constructive interference of the scattered X-rays is given by Bragg's law:

$$n\lambda = 2d_{hkl} \sin \theta \quad (24)$$

Here, n is a positive integer, λ is the wavelength of the incident X-ray beam, d_{hkl} is the difference between two crystallographic planes, and θ is the angle of incidence of the X-ray beam with respect to the surface normal (**Figure 22**). In practice, a measurement is performed with a constant wavelength and the diffractogram is recorded as a function of θ . For each θ at which Bragg's law is obeyed, a peak (reflection) is observed in the diffractogram. Since different crystalline materials have different crystal symmetries, bond distances and space groups, the whole set of recorded reflections can be seen as a "fingerprint" of the material. Huge crystallographic databases (e.g., PDF or IOCD database) enable the identification of crystalline phases in the specimen.

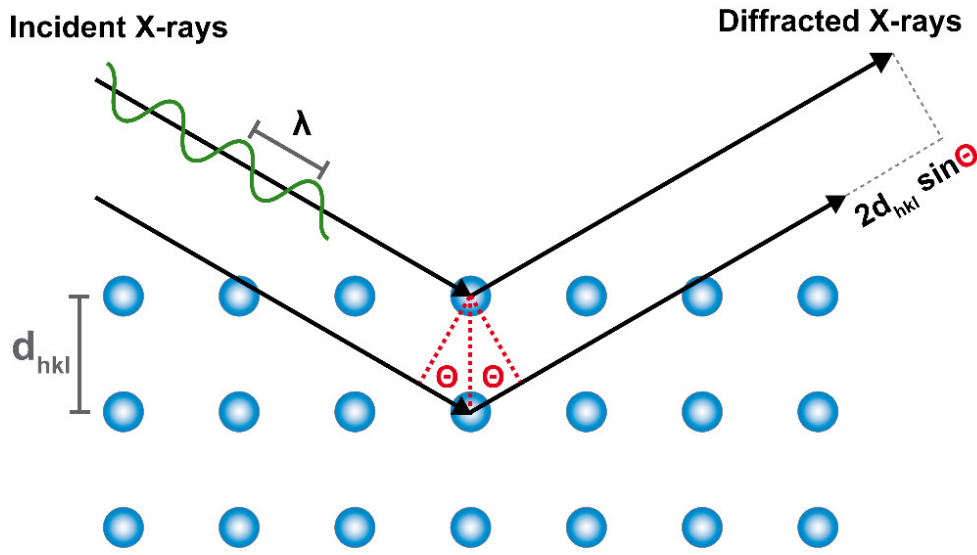


Figure 22. Schematic illustration of X-ray diffraction by a crystalline material. Constructive interference occurs when the difference in the optical path of scattered X-ray waves by two crystalline planes with a distance d_{hkl} ($2d_{hkl} \sin \theta$) is equal to an integer multiple of the wavelength of the incident X-ray (λ) (Bragg's law).

The coherent scattering domain size of a crystalline material (d_{ds}) can be estimated with the integral width of the peak profile (β_i) after correction for the instrumental line broadening using the Scherrer equation:

$$d_{ds} = \frac{K_s \lambda}{\beta_i \cos \theta} \quad (25)$$

Here, K_s is the dimensionless shape factor. It should be noted that this formula is only valid for domain sizes smaller than $\sim 0.1 \mu\text{m}$ and assumes no strain in the crystal.

Figure 23 illustrates two common measurement geometries for X-ray diffraction. In the $\theta/2\theta$ scan geometry (**Figure 23a**), the X-ray tube and the detector have the same angle with respect to the sample during the whole measurement. This geometry is mostly used for powder diffraction. In this thesis, this configuration was used for measuring the home-made PLD targets. In the grazing incidence geometry, the X-ray tube is fixed at a small angle and only the detector is moved during the measurement (**Figure 23b**). This configuration is preferred for the measurement of thin films since the small angle results in a higher surface sensitivity compared to the $\theta/2\theta$ scan geometry.

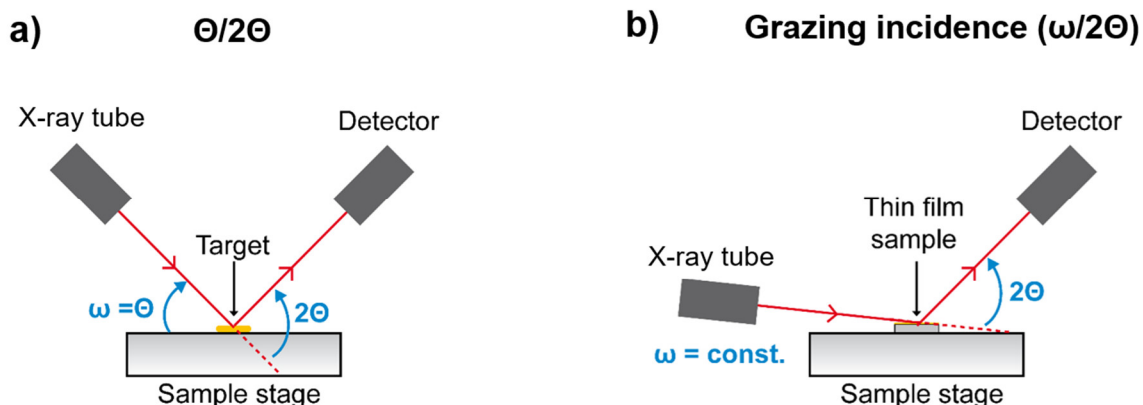


Figure 23. Measurement geometries for X-ray diffraction. **a)** $\theta/2\theta$ geometry in which X-ray tube and the detector have the same angle (θ) with respect to the sample during the whole measurement. **b)** Grazing incidence geometry commonly used for thin film samples. Here, the X-ray tube is fixed at a small angle (ω) and only the detector moves during the measurement increasing the surface sensitivity.

Experimental details:

X-ray diffraction measurements of the prepared targets were performed using a PANalytical MPD diffractometer with Cu K_{α} radiation ($\lambda = 1.5406 \text{ \AA}$) at 40 kV and 40 mA in a $\theta/2\theta$ geometry. The integration time was 2.7 s/step and the step size was 0.013° . XRD patterns of thin films were obtained using a Bruker D8 diffractometer with Cu K_{α} radiation at 40 mA and 40 kV in a grazing incidence geometry. Measurements were carried out with an angle of incidence of 0.5° , a step size of 0.02° and a step time of 5 s. Reference patterns from the PDF and IOCD crystallographic databases were used to identify the crystalline phases.

2.2.3 Time-resolved microwave conductivity (TRMC)

Time-resolved microwave conductivity (TRMC) is a powerful tool to study the charge carrier transport in thin film semiconducting materials.^[112-114] The measurement setup consists of a microwave source, a microwave cavity containing the sample, a nanosecond laser, a microwave detector with an amplifier, and an oscilloscope (**Figure 24**). In short, charge carriers are generated in the sample by a short laser pulse ($\sim 7 \text{ ns}$) and probed with a microwave. The cavity is designed to form a single standing microwave. The sample is positioned at the maximum of the wave (at $\frac{1}{4}$ distance from the end of the cavity) which increases the sensitivity of the setup by a factor of ~ 10 compared to measurements without a cavity.^[112] From the change of the reflected microwave power with time, important parameters such as the effective charge carrier mobility, lifetime, and diffusion length can be derived as presented in the following part.

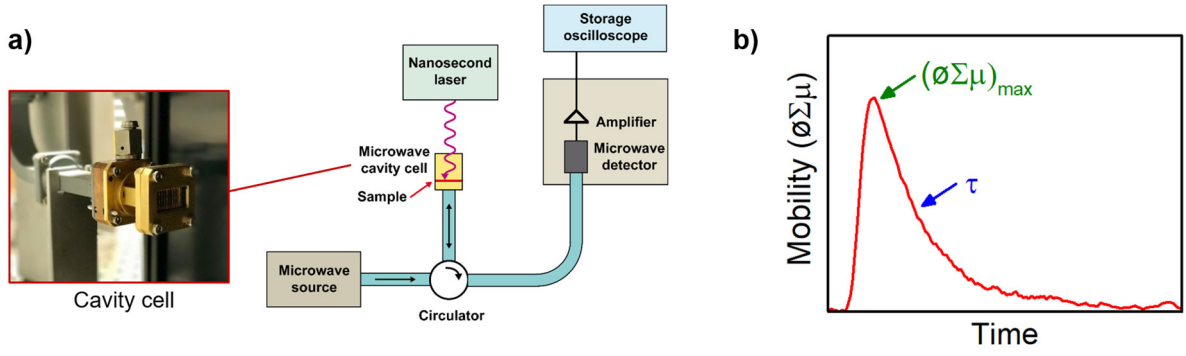


Figure 24. **a)** Time-resolved microwave conductivity (TRMC) measurement setup with an photograph of the cavity. **b)** Typical TRMC signal of a semiconducting material depicting the peak mobility $(\varnothing\Sigma\mu)_{max}$ and the effective lifetime (τ) .

The normalized change of the reflected microwave power ($\Delta P/P$) by the cavity is directly related to the change in conductance (ΔG) in the sample as follows:

$$\frac{\Delta P(t)}{P} = -K\Delta G(t) \quad (26)$$

Here, K is the sensitivity factor of the cavity. It depends on the cavity dimensions, the quality of the inner cavity walls and the dielectric properties of the sample and is given by the following expression:

$$K = \frac{2Q_L \left(1 + \frac{1}{\sqrt{R_0}}\right)}{\pi f_0 \varepsilon_0 \varepsilon_r L \beta} \quad (27)$$

Where Q_L is the quality factor of the cavity, R_0 is the depth of the resonance curve, f_0 is the resonance frequency, ε_0 is the dielectric permittivity of vacuum, ε_r is the relative dielectric permittivity of the sample, L is the length of the cavity, and β is the ratio of the length and width of the cavity.

The change in conductance ΔG is related to the conductivity at a depth z in the film $\Delta\sigma(z)$ as follows:

$$\Delta G = \beta \int_0^L \Delta\sigma(z) dz \quad (28)$$

With $\Delta\sigma(z) = eN(z)\Sigma\mu$, where $N(z)$ is the concentration of photogenerated electron-hole pairs at a depth z and $\Sigma\mu$ is the sum of the electron and hole mobilities (μ_e and μ_h), equation (28) can be written as follows:

$$\Delta G = \beta e \sum \mu \int_0^L n(z) dz \quad (29)$$

Under the assumption that no recombination occurs during the rise-time of the laser pulse, equation (29) can be simplified to:

$$\Delta G = \beta e I_0 A \phi \sum \mu \quad (30)$$

Where I_0 is the intensity of the excitation laser, A is the absorptance of the film at the excitation laser wavelength, and ϕ is the internal quantum yield. Overall, the change of the reflected microwave power is related to the sum of the electron and hole mobilities as follows:

$$\frac{\Delta P(t)}{P} = -K \beta e I_0 A \phi \sum \mu \quad (31)$$

Being a time-resolved technique, the lifetime of the photogenerated charge carriers can be extracted from the decay of the TRMC signal. To avoid confusion, it should be noted that the term *lifetime*, which is conventionally defined as the average time needed for charge carriers to recombine in covalent semiconductors (e.g., Si), can be misleading in the TRMC analysis of metal oxide semiconductors. In metal oxides, charge carriers can for example form polarons or undergo trapping/de-trapping processes through defect states; the mobility can therefore be greatly reduced and result in a decrease of the signal; however, this decrease does *not* indicate recombination. Therefore, it is difficult to distinguish if the decay of the TRMC signal in metal oxides is caused by the loss of carrier concentration (recombination) or a decrease in their mobility (trapping). The term *effective lifetime* is a more suitable description in metal oxide semiconductors and will be used in this work.

The effective charge carrier diffusion length (L_D) can be calculated from the effective charge carrier lifetime (τ) as follows:

$$L_D = \sqrt{\frac{\mu T k_B \tau}{e}} \quad (32)$$

Experimental details:

In this thesis, TRMC measurements of the BiVO₄ films were performed using a frequency-doubled Q-switched Nd:YAG laser ($\lambda = 355$ nm) as the excitation source and an X-band (8400-8700 MHz) microwave generated by a voltage-controlled oscillator (Sivers IMA VO3262X) as the probe. The pulse length of the laser was 7 ns. The films deposited on quartz were placed in a cavity and were exposed to air during the measurements. Due to an upgrade of our setup during the preparation of this thesis, TRMC analysis of the α -SnWO₄ were performed using a wavelength-tunable laser (NT230-50-SH/SF, EKSPLA) as the

excitation source. For the quantification of the K factor (equation (27)), dielectric constants of 62.3^[96] and 68^[115] were used for α -SnWO₄ and BiVO₄, respectively.

2.2.4 Photoelectrochemical (PEC) measurements

Photoelectrochemical measurements are essential to quantify the performance of a photoelectrode material. One of the most common techniques is to measure the AM1.5 photocurrent density (j_{ph}) as a function of the applied potential. Typically, a single material is measured in a photoelectrochemical cell with a three-electrode arrangement: (i) the photoelectrode as the working electrode, (ii) a reference electrode (e.g. Ag/AgCl), and (iii) a platinum wire as the counter electrode (**Figure 25**). The cell is filled with an electrolyte and has a transparent quartz window to allow the photoelectrode to be illuminated. During the measurement, a potentiostat applies a potential to the working electrode with respect to the stable and known potential of the reference electrode, while the current is flowing and measured between the working and counter electrode. In this way, uncertainties in the potential of the working electrode resulting from the unknown current-dependent overpotential at the counter electrode can be avoided.

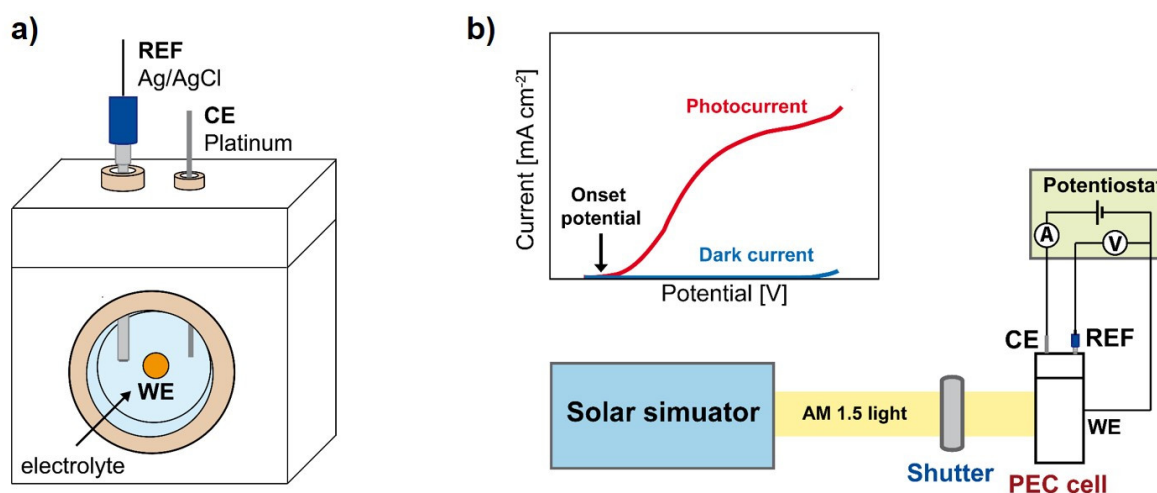


Figure 25. a) Photoelectrochemical cell with a three electrode arrangement: reference electrode (REF), counter electrode (CE) and the photoelectrode as the working electrode (WE). The cell can be filled with an electrolyte and has a transparent window to allow illumination during the measurements. b) PEC measurement setup consisting of an AM1.5 solar simulator, a shutter, and the PEC cell connected to a potentiostat. In addition, a typical photocurrent measurement is shown indicating the onset potential of the photocurrent.

Usually, measurements are performed in the dark and under AM1.5 illumination generated by a solar simulator to distinguish between the dark current and the photocurrent (**Figure 25b**). Chopped measurements are also commonly performed since they can provide information about surface recombination processes or slow charge transfer kinetics.^[116]

Another important method is the measurement of the external quantum efficiency, which is usually referred to as the incident photon-to-current efficiency (IPCE). IPCE values are

usually measured as a function of the incident light wavelength in order to reveal the individual contribution from each photon energy to the overall photocurrent (**Figure 26a**). The measurement setup is similar to the photocurrent measurements as discussed above. However, instead of a solar simulator, a white light source coupled to a monochromator is used. IPCE values can also be measured as a function of light intensity instead of wavelength (**Figure 26b**). Here, a laser (e.g., Ar ion laser) in combination with different optical density filters is used as the excitation light source. This method can provide important insights into a possible light intensity dependence of the IPCE.

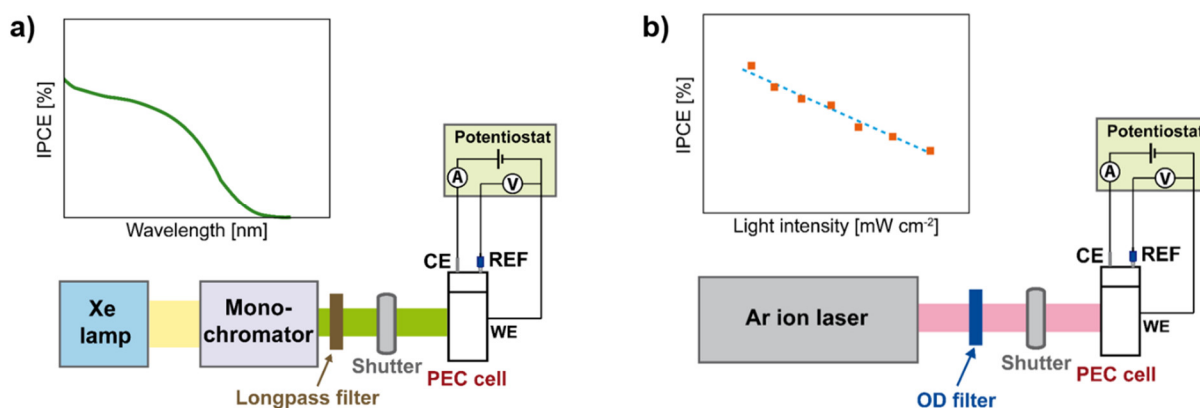


Figure 26. **a)** Wavelength-dependent IPCE measurement setup consisting of a Xe lamp coupled to monochromator, a longpass filter and a PEC cell connected to a potentiostat. **b)** Light intensity dependent IPCE measurement setup using an Ar ion laser and different optical density filters as an excitation source. Typical measurement results for both methods are shown.

The IPCE is given by the following formula:

$$IPCE(\lambda) = \frac{1240 \cdot j(\lambda)}{\lambda \cdot I_0(\lambda)} \quad (33)$$

Here, λ is the wavelength in nm, $j(\lambda)$ is the photocurrent density in mA cm^{-2} , and $I_0(\lambda)$ is the light intensity of the incident light in mW cm^{-2} .

Experimental details:

In this thesis, all photoelectrochemical measurements were performed in a PEC cell with an Ag/AgCl-reference electrode ($E_{\text{Ag/AgCl}} = 0.199 \text{ V}$ vs. normal hydrogen electrode, NHE), a platinum wire as the counter electrode and the respective film as the working electrode. The illuminated area of the sample was 0.28 cm^2 (circular area with a diameter of 6 mm). The electrolyte was a 0.5 M potassium phosphate (KP_i) buffer solution prepared by adjusting the ratio of KH_2PO_4 (99%, Sigma Aldrich) and K_2HPO_4 (99%, Sigma Aldrich) to obtain a pH 7 solution. If necessary, either 0.5 M Na_2SO_3 (99%, Sigma Aldrich) or 5 mM RuCl_3 (99%, Aldrich) was added as a hole scavenger.

AM1.5 photocurrent density measurements were carried out with a WACOM Super Solar Simulator (Model WXS-505-5H, AM1.5, Class AAA) and an EG&G Princeton Applied Research Potentiostat/Galvanostat (Model 273A). All electrochemical potentials are given with respect to the reversible hydrogen electrode (RHE) according to the following equation:

$$E_{RHE} = E_{measured} + E_{Ag/AgCl} + 0.059 \times pH \quad (34)$$

Incident photon-to-current efficiency measurements as a function of wavelength were performed with a Xe lamp (LOT, LSH302) and an Acton Research monochromator (Spectra Pro 2155). An electronic shutter (Uniblitz LS6) was used, and a long-pass colored filter (Schott, 3 mm thick) was placed between the monochromator and the sample to remove higher-order diffracted light. IPCE as a function of light intensity was measured with a continuous wave (CW) argon ion laser (Innova 90C Series, Coherent) at a wavelength of 459.7 nm. The intensity was varied by applying different neutral density filters (Melles Griot, OD 0.1-3). The power density of the incident light was measured by a calibrated photodiode (PD300R-UV, Ophir) at the back-side of the PEC cell. For the light intensity measurements, an uncoated quartz substrate was used instead of the photoelectrode so that light travels via the front quartz window of the PEC cell, the electrolyte and the quartz substrate onto the photodiode.

2.2.5 Other methods

a) UV-Vis spectroscopy

UV/Vis-spectroscopy was performed to investigate the optical properties of the pulsed laser deposited BiVO_4 and $\alpha\text{-SnWO}_4$ films. Measurements were conducted using a PerkinElmer Lambda 950 spectrophotometer with an integrating sphere. The films deposited on quartz were placed inside the integrating sphere with an offset of $\sim 7.5^\circ$ from the incident light, and the transfectance (TR , i.e., transmittance T + reflectance R) was measured. The absorption coefficient (α) was calculated from the transfectance and the thickness (t) of the film using the following formula:

$$\alpha = \frac{-\ln(TR)}{t} \quad (35)$$

The bandgap energy was determined from the absorption coefficient (α) using the Tauc relationship which is given as follows:

$$(\alpha h\nu)^{\frac{1}{n}} \propto (h\nu - E_g) \quad (36)$$

Here, h is the Planck's constant, ν is the frequency of the light, and n denotes the nature of the optical transition (1/2 for direct allowed transition, 3/2 for direct forbidden transition, 2 for indirect allowed transition and 3 for indirect forbidden transition).

b) Microscopy

The morphology of the pulsed laser deposited films was investigated with several microscopy techniques. Scanning electron microscopy (SEM) micrographs were taken using a LEO GEMINI 1530 with acceleration voltage of 4–10 kV. High-resolution scanning electron microscope (HRSEM) imaging was performed in a Zeiss Merlin KMAT scanning electron microscope at 15 kV acceleration voltage with 74 pA beam current. Cross sections of the α -SnWO₄ films deposited on FTO were prepared by focused Ga ion beam machining in a Zeiss Crossbeam 340 KMAT dual beam instrument. A ~200 nm thick platinum protective layer was deposited onto the surface of the films by electron beam induced deposition. The patterning was carried out at an acceleration voltage of 30 kV and 50 pA followed by a 10 pA polishing step. To investigate the morphology of α -SnWO₄ films deposited on quartz, helium ion microscopy (HIM) was performed. Imaging were taken at an acceleration voltage of 30 kV and currents from 0.6–2.4 pA in a Zeiss Orion Nanofab instrument with an Everhart-Thornley detector. The system was equipped with an electron flood gun for charge compensation.

c) Energy-dispersive X-ray spectroscopy (EDX)

As discussed above, RBS is the method of choice to quantify the elemental composition of a thin film on a light (i.e., low atomic mass) substrate. Films deposited on FTO needed for PEC measurements, however, cannot be precisely analyzed with RBS due to the heavy element Sn in the substrate. Therefore, Energy-Dispersive X-ray spectroscopy (EDX) was performed as a complementary technique to determine the V:Bi ratio of BiVO₄ films deposited on FTO. In this technique, an electron beam excites an electron in an inner shell of an atom in the specimen creating a core hole which is subsequently filled by an electron from a higher-energy shell. This process emits an X-ray with an energy that corresponds to the energy difference between the two states. The energy of the emitted X-ray is measured with a detector and is characteristic for the element that was excited. From the counts, a quantitative element analysis by EDX is possible. However, even though the quantitative element analysis by EDX is performed with the Phi-Rho-Z correction method, the obtained element ratios are often afflicted by a systematic error when no real standard is used. Especially the exact determination of the elemental composition of thin films (~150 nm) is difficult since EDX typically probes a volume of 1 μm^3 and the spectrum therefore contains spectral lines as well as a broad continuum (bremsstrahlung) from the substrate material.

In this thesis, EDX analysis of the BiVO₄ target and BiVO₄ films deposited on FTO was performed using a LEO GEMINI 1530 scanning electron microscope with an electron

acceleration voltage of 10 kV. The elemental analysis was performed with the Phi-Rho-Z correction method. To calibrate the quantitative EDX analysis of films deposited on FTO, a $\text{Bi}_x\text{V}_y\text{O}_z$ film with a thickness of ~150 nm and a V:Bi ratio of ~1 was pulsed laser deposited on glassy carbon by the alternating ablation of Bi_2O_3 and V_2O_5 targets. The V:Bi ratio of this film was analyzed with both RBS and EDX (see **Figure S 1**). From this, a correction factor of ~0.76 is obtained. In addition, identical films were prepared on glassy carbon and FTO by the ablation of a BiVO_4 target and the composition of both films was analyzed with EDX (see **Figure S 2**). Here, no significant change is found. Therefore, a correction factor of 0.76 with an estimated error of ± 0.05 is used to estimate the V:Bi ratio of films deposited on FTO with EDX.

d) X-ray photoelectron spectroscopy (XPS) / ultraviolet photoelectron spectroscopy (UPS)

To investigate the oxidation states of Sn and W in the $\alpha\text{-SnWO}_4$ films, X-ray photoelectron spectroscopy (XPS) was performed with a monochromatic Al K_α X-ray-source (1486.74 eV, Specs Focus 500 monochromator). In this technique, an X-ray photon excites a core electron of the surface atoms and the kinetic energy ($E_{kinetic}$) of the escaped electron is measured. The binding energy of the electrons ($E_{binding}$) in the material is given by:

$$E_{binding} = E_{ph} - (E_{kinetic} + \chi) \quad (37)$$

Here, E_{ph} is the energy of the incident X-ray and χ is the work function of the spectrometer. The obtained spectrum contains binding energy peaks that are characteristic for different elements and their oxidation states. The work function (Φ) and the valence band maximum edge of $\alpha\text{-SnWO}_4$ were determined using ultraviolet photoelectron spectroscopy (UPS) with a He I source ($E_{HeI} = 21.218$ eV). The work function is given by the following expression:

$$\phi = E_{HeI} - (SEC - U_{bias}) \quad (38)$$

where SEC is the energy that corresponds to the secondary electron cutoff and U_{bias} is the bias voltage. A hemispherical analyzer (Specs Phoibos 100) was used for both XPS and UPS measurements. The base pressure of the system was $\sim 10^{-9}$ mbar.

e) Time-resolved THz spectroscopy (TRTS)

In addition to time-resolved microwave conductivity, time-resolved terahertz spectroscopy (TRTS) was performed to investigate the charge carrier transport properties in $\alpha\text{-SnWO}_4$. With this technique, charge carriers are generated with a 150 fs laser pulse and are probed with a THz pulse. Measurements were performed with a THz spectrometer connected to a

femtosecond laser system consisting of a 150 kHz amplifier (RegA, Coherent) seeded by 800 nm pulses of a Ti:sapphire 80 MHz oscillator (Mira, Coherent). The laser pulses had an energy of 7 μJ and an autocorrelation lengths of ~ 70 fs (FWHM). For THz generation, THz detection, and the optical excitation of the $\alpha\text{-SnWO}_4$, the laser output was split into three branches at the frequency-doubled wavelength of 400 nm. The intensity of the laser pulse for the optical excitation was $7 \times 10^{13} \text{cm}^{-2}$. A more detailed description of the measurement setup and data analysis can be found elsewhere.^[117]

Chapter 3 – Elucidating the pulsed laser deposition process of efficient BiVO_4 photoelectrodes for solar water splitting

Parts of this chapter were adapted from:

M. Kölbach, K. Harbauer, K. Ellmer, R. van de Krol, *Elucidating the pulsed laser deposition process of efficient BiVO_4 photoelectrodes for solar water splitting*, **in preparation**

3.1 Introduction

As discussed in chapter 1.4.1, BiVO₄ is a useful platform for the development of efficient ternary metal oxide photoelectrodes. After the discovery of its photoactivity by Kudo et al. in 1998, many groups started to work on this material and hence its performance has been steadily increased by systematically identifying and addressing its performance limitations. The main limitations of BiVO₄ are its poor charge carrier transport properties (resulting from a small polaron conduction mechanism) and recombination of charge carriers via surface states. Using core-shell WO₃/BiVO₄ nanorods modified with CoP_i, Pihosh et al. achieved a record AM1.5 photocurrent of 6.72 mA cm⁻² at a potential of 1.23 V vs. RHE in 2015, which is close to the theoretical maximum value of 7.5 mA cm⁻².^[51] To build a more practical stacked tandem device, however, a compact and hence non-scattering top absorber is required (see chapter 1.4.1).

Pulsed laser deposition (PLD) is a physical vapor deposition technique that meets the demands of producing compact non-scattering films with a high electronic quality (see chapter 2.1.1). Retti et al. successfully prepared both epitaxial and polycrystalline BiVO₄ films with PLD and achieved an AM1.5 sulfite oxidation photocurrent of 0.15 mA cm⁻² with the latter one.^[118] Murcia-López et al. reported on pulsed laser deposition of SnO₂/WO₃/BiVO₄ heterostructures by the consecutive ablation of these materials and reported an AM1.5 photocurrent of > 2 mA cm⁻² with H₂O₂ added as a hole scavenger.^[119] The effect of the growth temperature on the morphology of BiVO₄ photoelectrodes prepared with PLD was investigated by Jeong et al.^[120] They achieved AM1.5 sulfite oxidation photocurrents of up to 3.0 mA cm⁻² at 1.23 V vs. RHE and attributed these high values to an enhanced surface area of their films when deposited at a substrate temperature of 230°C. The more fundamental aspects of the PLD process, however, have not yet been investigated in detail. For example, the reasons for the dependence of the V:Bi ratio of the deposited film on the substrate temperature^[120] and on the oxygen background pressure^[118-119] are still not known.

Here, the complex pulsed laser deposition process of efficient BiVO₄ photoelectrodes is systematically elucidated. First, the laser fluence, the oxygen background pressure, and the substrate temperature are carefully optimized to achieve a stoichiometric target-to-substrate transfer during the ablation of a BiVO₄ target. Based on this, a straightforward approach for the fabrication of compact, stoichiometric and efficient BiVO₄ thin films is devised. Moreover, the process parameters are correlated with the charge carrier transport properties measured using time-resolved microwave conductivity (TRMC) and with the PEC performance of the deposited films. Finally, an alternative preparation route based on the alternating ablation of Bi₂O₃ and V₂O₅ targets is presented as an effective way to control the stoichiometry and to synthesize efficient BiVO₄ photoelectrodes.

3.2 Control of the V:Bi ratio

To minimize the amount of defects in BiVO₄ prepared by PLD, deviations from the ideal stoichiometric target-to-substrate transfer should be avoided.^[28] When a complex metal oxide target is ablated, the cation stoichiometry of the deposited films can be a function of several process parameters. The most important ones are the laser fluence, the oxygen background pressure, and the substrate temperature.^[105,109] These parameters affect one or more of the three main steps in the PLD process, i.e., the target ablation, expansion of the plasma plume and the film condensation (**Figure 27**). Therefore, in the following part, the influence of the process parameters on these three processes and on the resulting V:Bi ratio of the deposited films are investigated.

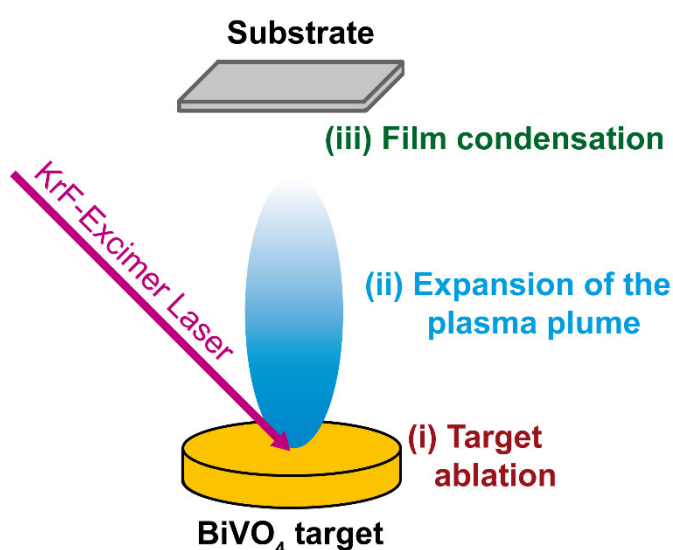


Figure 27. Schematic drawing of the three main PLD processes that occur during the preparation of BiVO₄ thin films by ablating a BiVO₄ target

The laser fluence (F) is one of the most important PLD process parameters. Its influence on the film stoichiometry is commonly attributed to a preferential ablation of the most volatile elements in the target when the chosen fluence is too low.^[105,121-122] To investigate the ablation process for a BiVO₄ target, the laser fluence was varied and the V:Bi ratio of the deposited films and the ablated target material were measured by RBS and EDX, respectively (**Figure 28a**). The films were deposited in vacuum at room temperature (RT) to minimize the influence of gas-phase collisions and re-sputtering/re-evaporation from the substrate on the V:Bi ratio. The upper panel in **Figure 28a** reveals that films deposited with fluences $\leq 1 \text{ J cm}^{-2}$ are Bi-rich (see **Figure S 3** for fitted RBS spectra). Correspondingly, the target surface was found to be V-rich at these fluences, as shown in the middle panel. These results clearly indicate a preferential ablation of Bi from the laser-induced melt for fluences $\leq 1 \text{ J cm}^{-2}$. At higher fluences, a nearly stoichiometric target-to-substrate transfer is observed (the reason for the slight V-enrichment will be discussed later). The change from the Bi-rich to the near-stoichiometric regime is accompanied by a change in the slope of the deposited

mass as a function of the fluence measured with a quartz crystal monitor (**Figure 28a**, lower panel). This behavior is likely caused by a change in the ablation mechanism.^[121] This is supported by the appearance of so-called *cones* at the target surface after irradiation with laser fluences $\leq 1 \text{ J cm}^{-2}$ (**Figure 28b**). These are typically formed during a preferential ablation of one species out of a multicomponent target.^[123]

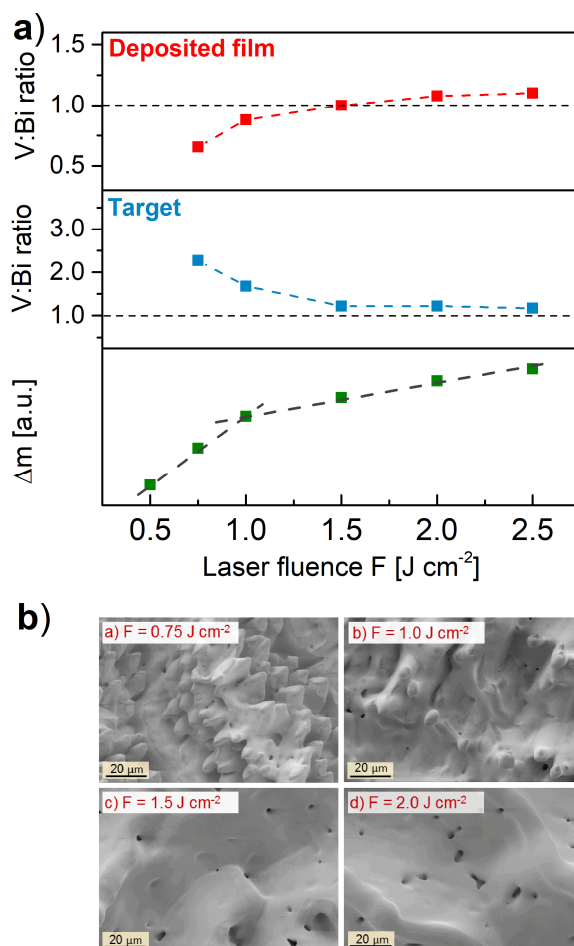


Figure 28. a) Impact of the laser fluence (F) on the V:Bi ratio of the deposited film measured with RBS (top), on the V:Bi ratio of the target surface qualitatively measured with EDX (middle) and on the deposited mass (Δm) determined with a quartz crystal microbalance (bottom). Films with a thickness of $\sim 100 \text{ nm}$ were deposited on glassy carbon in vacuum at RT. The target-to-substrate and target-to-QCM distances were both set to 60 mm. **b)** Scanning electron microscopy images of the BiVO_4 target surface after irradiation with different laser fluences.

The reason for preferential ablation of Bi at low fluences is attributed to the ~ 7 orders of magnitude higher vapor pressure of Bi compared to V (see **Figure S 4**). The ablation mechanism of a BiVO_4 target for $F \leq 1 \text{ J cm}^{-2}$ is, therefore, partially determined by evaporation rather than fully stoichiometric transfer.^[109]

A surprising observation is that the films deposited from a V-rich target surface continue to be rich in Bi. Similar behavior was found for the PLD of SrTiO_3 at fluences $< 1.3 \text{ J cm}^{-2}$ by Dam et al., who observed the deposition of Sr-rich films from a Ti-rich target surface.^[121] This was explained by a compensation of the Sr depletion at the target surface via diffusion of Sr

from the bulk to the laser-induced melt. It seems likely that the Bi-depletion at our BiVO₄ target surface is compensated by a similar mechanism.

After the laser pulse, the ablated species expand rapidly away from the target surface to the substrate. When depositing metal oxides with PLD, an oxygen background pressure usually has to be added to obtain (and maintain) the desired anion stoichiometry.^[124-128] There can be several reasons for this, such as a change in the oxygen concentration in the target material after laser irradiation^[123,129] or a low sticking coefficient of oxygen at the surface of the growing film^[128]. Adding an oxygen background gas, however, may also influence the cation stoichiometry of the deposited films due to element-dependent thermalization and scattering processes.^[105,109] To investigate the effects of an oxygen background pressure in the PLD process of BiVO₄, films were deposited on glassy carbon in different oxygen pressures. During these experiments, the substrates were not heated and the laser fluence was kept constant at 1.5 J cm⁻². RBS analysis of the films (**Figure 29a**) clearly shows that an increase in oxygen background pressure results in a gradual decrease of the V:Bi ratio (see **Figure S 5** for the fitted RBS spectra). At the highest oxygen background pressure used in these experiments, 2.5 x 10⁻² mbar, the film has a V:Bi ratio of only ~0.77.

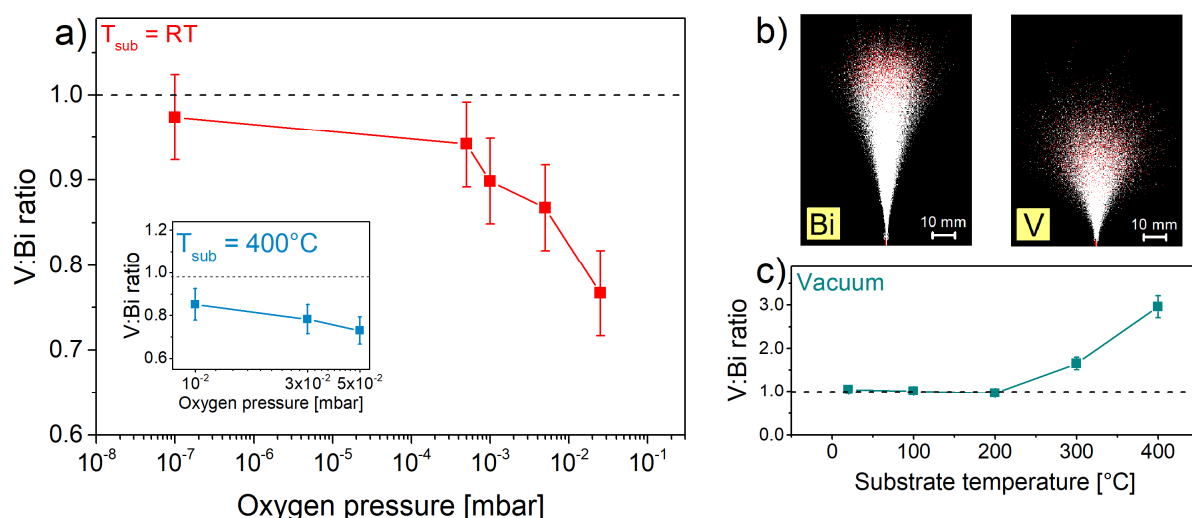


Figure 29. a) V:Bi ratio of films deposited on glassy carbon as a function of the oxygen background pressure measured with RBS. Films were deposited in vacuum at RT. Inset: V:Bi ratio of films deposited onto FTO with a substrate temperature of 400 °C as a function of the oxygen background pressure determined with RBS corrected EDX measurements. b) Qualitative Stopping-Range-of-Ions-in-Matter (SRIM) simulations for Bi and V atoms in an oxygen pressure of $p_{O_2} = 2.5 \times 10^{-2}$ mbar with a starting kinetic energy of 50 eV. c) V:Bi ratio of films deposited in vacuum onto FTO-glass as a function of the substrate temperature determined with RBS corrected EDX measurements. The laser fluence 1.5 J cm⁻² and the target-to-substrate distance was 60 mm for all shown depositions.

This observation can be qualitatively explained with Stopping-Range-of-Ions-in-Matter (SRIM) simulations.^[130] Although these Monte-Carlo-based simulations cannot describe complex gas dynamic processes, such as the formation of shock waves or plasma confinement, they can provide useful insights in thermalization processes at modest

pressures.^[131-133] The simulations for an oxygen pressure of 2.5×10^{-2} mbar reveal a much faster thermalization of V compared to Bi in the propagating plasma plume (**Figure 29b**). This can simply be attributed to the huge difference in the atomic masses of Bi and V. The ratio of the atomic masses of Bi and its impact partner O₂ is 6.5, which is a factor of ~4 times higher than the ratio for V and O₂ (1.6). The critical oxygen pressure (p_c) for which the mean free path (λ) of the ions equals to the target-to-substrate distance (d) can be calculated using the following relationship,

$$\lambda = \frac{k_b T}{\sqrt{2} \sigma p_c} \quad (39)$$

where k_b is the Boltzmann constant, T is the temperature, and σ is the collision cross section ($\sim 0.5 \text{ nm}^2$).^[134] With a target-to-substrate distance of 60 mm, the critical oxygen pressure is found to be 1×10^{-3} mbar. This is indeed in the range where the oxygen pressure starts to significantly affect the ~V:Bi ratio (see **Figure 29a**).

The final step in the PLD process is the film condensation. Here, the substrate temperature (T_{sub}) is an important parameter since it determines the growth kinetics and thus the structure and morphology of the deposited film.^[131-132] However, it can also influence the cation stoichiometry of complex metal oxides films due to element-dependent re-sputtering or re-evaporation effects from the substrate.^[105,109,135] In the case of BiVO₄, the V:Bi ratio of films deposited in vacuum is indeed affected by the substrate temperature. For $T_{sub} > 200$ °C, the V:Bi ratio drastically increases as shown in **Figure 29c**, whereas for $T_{sub} \leq 200$ °C no influence on the film stoichiometry is observed. Since the vapor pressure of Bi is extremely low at 200°C (see **Figure S 4**), little or no re-evaporation of Bi would be expected under thermodynamic equilibrium conditions. The loss of Bi may, however, be enhanced by the high kinetic energy of the impinging species from the plasma plume. Depending on the substrate temperature and kinetic energy of the impinging species, this may give rise to either plasma-assisted re-evaporation or even re-sputtering of Bi.^[105] Such a re-sputtering of Bi might be also the reason for the slight enrichment in V when the films are deposited with a fluence $> 1.5 \text{ J cm}^{-2}$ in vacuum (**Figure 28a**, upper panel), since an increase in the fluence is accompanied by an increase in the kinetic energies of the impinging species.

Based on the $p(\text{O}_2)$ and temperature dependencies shown in **Figure 29a** and **c**, it should be possible to compensate the loss of Bi at higher oxygen pressures by using higher substrate temperatures to increase the V content. Interestingly, this is not the case as can be seen in the inset of **Figure 29a** which shows the V:Bi ratio of films deposited with a substrate temperature of 400°C while varying the oxygen background pressure. Only the process of the preferential thermalization of the lighter element V can be observed (decrease of the V:Bi ratio with increasing p_{O_2}). The re-sputtering/re-evaporation effects at higher substrate temperatures of the more volatile element Bi as discussed above is not present anymore. This is attributed to the thermalization of the ablated species due to collisions with the

oxygen molecules. In other words, the energy of the species is not high enough to cause re-sputtering/re-evaporation effects.

Based on the findings above, a straightforward approach was followed to obtain crystalline and stoichiometric BiVO₄ films. The deposition was carried out in vacuum at RT and the V:Bi ratio was adjusted with the laser fluence (see **Figure 28**). Subsequently, the films were crystallized by annealing in air at 450°C for 2 h. In the following two subchapters, these films are characterized with respect to their structure, charge carrier transport and PEC performance.

3.3 Structural characterization & charge carrier dynamics

XRD measurements were performed to determine the crystal structure of the pulsed laser deposited films. **Figure 30a** shows the diffractogram of a BiVO₄ film deposited in vacuum at RT on fluorine-doped tin oxide (FTO) coated glass with a fluence of 1.5 J cm⁻², and annealed at 450°C for 2h in air. In addition, the diffractogram of the BiVO₄ target as well as the reference pattern of monoclinic BiVO₄ (clinobisvanite, PDF no. 00-014-0688) are shown. Both the target and the thin film only show the reflections of monoclinic BiVO₄. The only other reflections in the film originate from the underlying FTO substrate (cassiterite, SnO₂, PDF no. 00-041-1445) and are marked with black asterisks. The as-deposited films without a post-deposition annealing step are found to be X-ray amorphous (see **Figure S 6**).

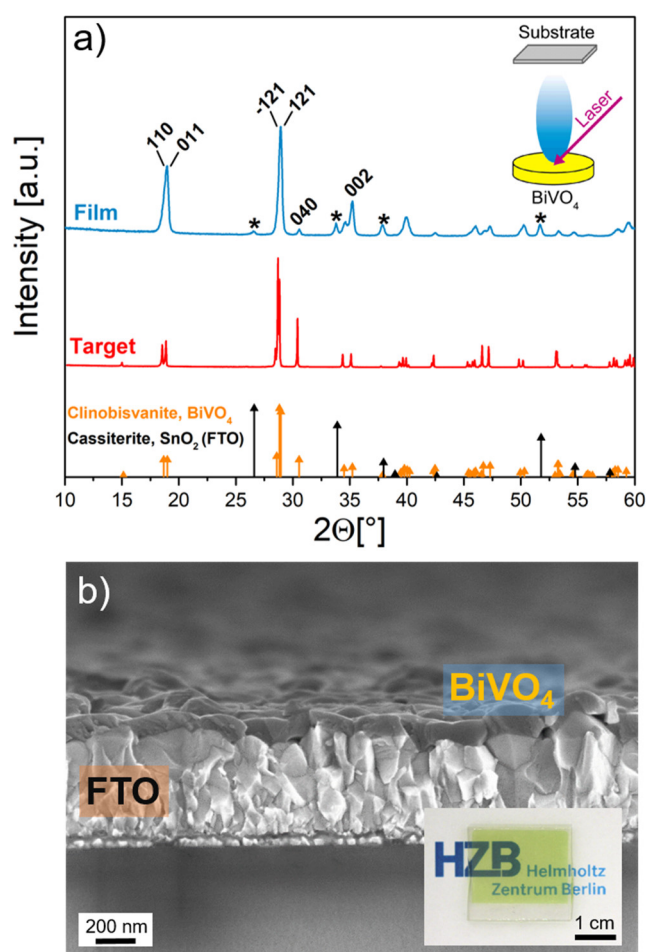


Figure 30. a) X-ray diffractograms of the BiVO₄ target and the BiVO₄ film with a thickness of 90 nm deposited on a FTO substrate ($F = 1.5 \text{ J cm}^{-2}$, vacuum, RT, annealing in air at 450 °C for 2 h). Orange lines represent the reference pattern of monoclinic BiVO₄ (PDF no. 00-014-0688). The reflections of the underlying FTO substrate are marked with black asterisks (cassiterite, SnO₂, PDF no. 00-041-1445). **b)** SEM cross section image of the respective BiVO₄ film. Inset: optical photograph.

The SEM cross section shown in **Figure 30b** reveals a compact and dense BiVO₄ film that shows little optical scattering (see inset **Figure 30b**). This is a crucial requirement for photoelectrodes that are to be combined with a bottom absorber in a practical stacked

tandem device for overall water splitting.^[31,51] The indirect bandgap of the film is found to be 2.4 eV (see **Figure S 8**) which gives the typical yellow color.

Charge carrier dynamics:

To investigate the charge transport properties and elucidate the electronic quality of the BiVO₄ films, TRMC measurements were performed (see chapter 2.2.3).^[112-114,136] **Figure 31** shows the peak mobility $(\phi\sum\mu)_{max}$ as a function of photon flux, averaged for three identical stoichiometric BiVO₄ films deposited on quartz. Two series were measured, one with a laser fluence of 1.5 J cm⁻² (blue curve) and one with a fluence of 1.0 J cm⁻² (red curve). The mobility $(\phi\sum\mu)_{max}$ for the 1.5 J cm⁻² series increases with increasing light intensity up to a maximum value of 0.13 cm² V⁻¹ s⁻¹ and decreases for higher light intensities. Such a maximum is typically attributed to the competing effects of electron trap filling (at low photon fluxes) and non-geminate higher order electron hole recombination (at high photon fluxes), as reported elsewhere.^[114,137] Similar behavior was also found in BiVO₄ films prepared by spray pyrolysis in our institute.^[138] The concentration of trap states in the films that dominate the behavior at low light intensities (< 1 x 10¹³ cm⁻²) is higher than the number of absorbed photon per pulse. From this value, the film thickness (90 nm), and its absorbance at $\lambda = 355$ nm of 0.74, a trap density (N_{trap}) of $\sim 8 \times 10^{15}$ cm⁻³ can be estimated. It should be noted that this value is only valid for the time window that can be resolved with TRMC.

From the decay of the TRMC signal the effective charge carrier lifetime can be extracted (inset of **Figure 31**). The signal follows a mono-exponential decay function and yields an effective lifetime (τ) of ~ 27 ns, which is found to be independent on the laser intensity (see Figure S 7). From this effective lifetime and the charge carrier mobility of 0.13 cm² V⁻¹ s⁻¹, an effective charge carrier diffusion length (L_D) of ~ 95 nm is calculated under the assumption of an internal quantum yield (ϕ) of 100%.

It should be noted, that the mobility of the charge carriers in the pulsed laser deposited BiVO₄ films is nearly twice as high as the mobility of films prepared by spray pyrolysis (SP) in our institute ($\mu_{SP} = 0.07$ cm² V⁻¹ s⁻²).^[47] However, the lifetime of the charge carriers in the pulsed laser deposited films is shorter ($\tau_{SP} = 43$ ns).^[47] This results in a comparable effective diffusion length ($L_{D, SP} \sim 90$ nm) for both deposition techniques. The elucidation of the reason for this requires a detailed comparison of the crystallite sizes as well as the concentration and nature of defects and is beyond the scope of this thesis. However, the smaller lifetime in the pulsed laser deposited films might result from defects created by the high kinetic energy of the impinging species, which cannot be removed or passivated during the annealing process.^[104] A common approach to thermalize (i.e., reduce the kinetic energy) of the ablated

species and thus lower the defect concentration is to add an inert background gas (e.g., Ar). In the case of ablating a BiVO₄ target, however, this concept is not easily applicable since a background pressure also changes the V:Bi ratio of the films (see **Figure 29**).

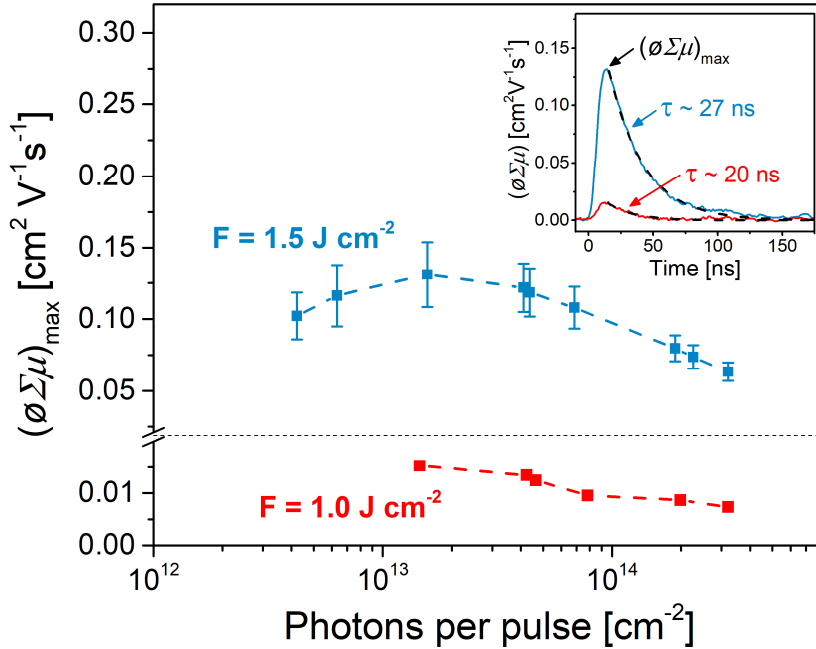


Figure 31. Maximum TRMC signal $(\phi\Sigma\mu)_{max}$ vs. photons per laser pulse ($\lambda = 355$ nm) of BiVO₄ films pulsed laser deposited on quartz substrates with a fluence of 1.0 and 1.5 J cm⁻². The error bars represent the spread from measurements of three identically prepared films. Inset: TRMC signal of the respective films at an intensity of $\sim 1.5 \times 10^{13}$ photons cm⁻².

To show the importance of carefully optimizing the process parameters, **Figure 31** also depicts the TRMC analysis of a Bi-rich film resulting from the deposition with a fluence of 1 J cm⁻² (see **Figure 28**). The charge carrier mobility in this film is nearly one order of magnitude lower than the mobility of the stoichiometric film. The peak mobility $(\phi\Sigma\mu)_{max}$ decreases from 0.015 cm² V⁻¹ s⁻¹ to 0.0074 cm² V⁻¹ s⁻¹ with increasing light intensity, indicating that non-geminate recombination dominates the behavior in this regime. It should be noted that mobilities at lower light intensities that might provide insights into trap filling processes could not be measured due to a poor signal-to-noise-ratio. The effective charge carrier lifetime of the Bi-rich film is also found to be reduced to 20 ns (see inset **Figure 31**), which results in an effective charge carrier diffusion length of only ~ 28 nm.

The poorer charge carrier transport in the Bi-rich films could either be a result of a worse crystalline quality (smaller domain size) or a higher number of defects acting as trapping and recombination centers.^[114,139] The SEM images of the films deposited on quartz, however, reveal no significant change in neither the morphology nor the coherent scattering domain size estimated using the Scherrer equation (~ 33 and ~ 39 nm for the film deposited with a fluence of 1.0 and 1.5 J cm⁻², respectively; see **Figure 32**). Therefore, the significantly poorer charge carrier transport in the Bi-rich film is attributed to additional defects resulting from its

non-stoichiometry. It should be noted that the rather small domain sizes suggest that the compact films shown in **Figure 32** consist of aggregated particles rather than single crystallites.

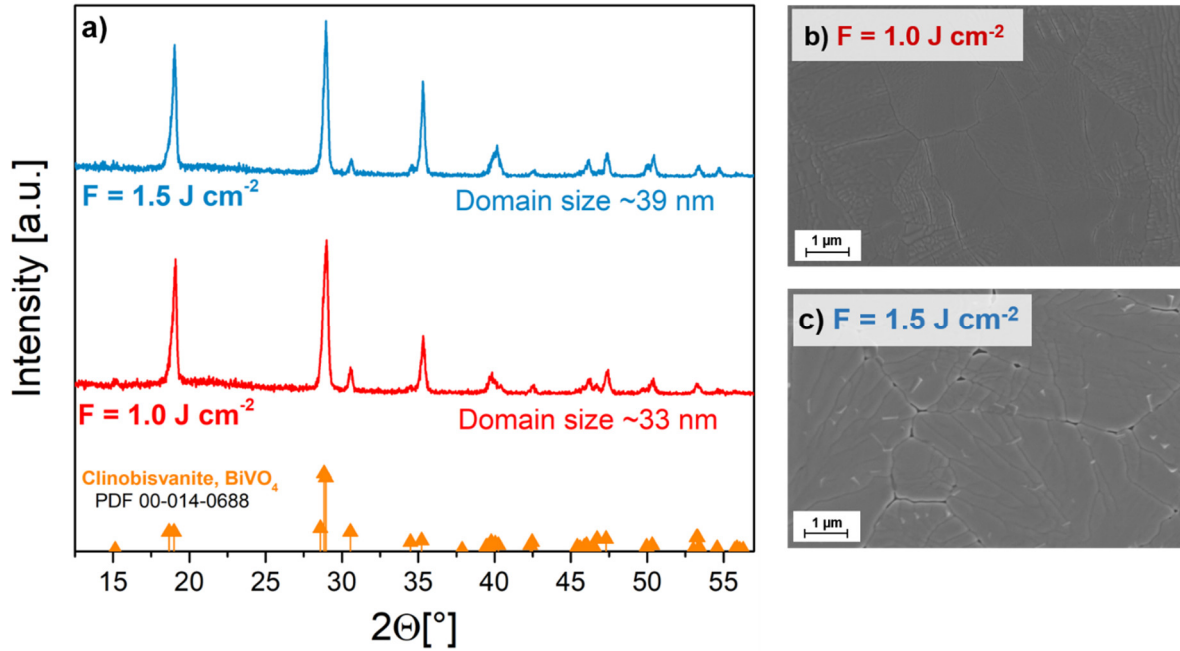


Figure 32. a) X-ray diffractograms of films deposited on quartz by ablating a BiVO_4 target in vacuum at RT with a fluence of 1.0 and 1.5 J cm^{-2} , respectively. Both films were annealed at 450°C for 2h in air. Orange lines represent the reference pattern of monoclinic BiVO_4 (PDF no. 00-014-0688). b) and c) SEM images of the respective films.

3.4 Photoelectrochemical characterization

Linear sweep voltammetry (LSV) under chopped AM1.5 illumination in a 0.5 M KP_i electrolyte (pH 7) was performed to evaluate the photoactivity of BiVO₄ films deposited on FTO. Initially, 0.5 M Na₂SO₃ was added as a hole scavenger to suppress charge transfer limitations and surface state recombination.^[74] A film thickness of ~90 nm was found to result in the highest photocurrent density due to an optimum in the trade-off between light absorption and charge carrier diffusion length (**Figure 33**). This thickness is indeed comparable to the effective charge carrier diffusion length found in the TRMC analysis of the films deposited on quartz.

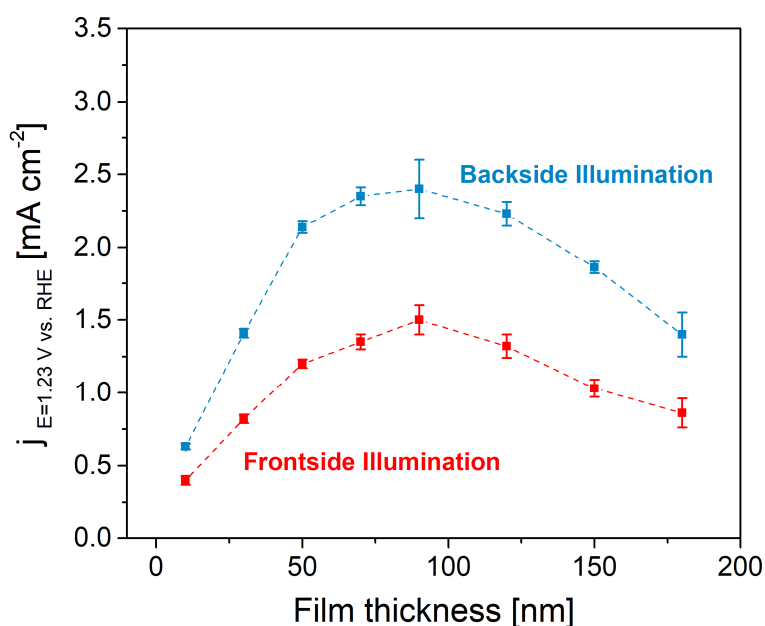


Figure 33. Photocurrent at a potential of 1.23 V vs. RHE as a function of the thickness of BiVO₄ photoanodes under AM1.5 illumination ($F = 1.5 \text{ J cm}^{-2}$, vacuum, RT, annealing in air at 450 °C for 2 h). The electrolyte was a 0.5 M KP_i-buffer (pH ~ 7) with 0.5 M Na₂SO₃ added as a hole scavenger.

The thickness-optimized BiVO₄ photoanode produces a sulfite oxidation photocurrent density of ~1.5 mA cm⁻² and ~2.5 mA cm⁻² under front and backside illumination, respectively. This is one of the highest photocurrents ever reported for undoped and low surface area (non-nanostructured) BiVO₄ photoanodes. Similar to other reports, the photocurrent onset potential is located at ~0.4 V vs. RHE (**Figure 34a**).^[47,140] The significant higher photocurrent under backside illumination suggests that majority carrier (electron) transport is limiting, consistent with earlier reports for undoped BiVO₄ photoanodes.^[33] To verify the reproducibility of the relatively high photocurrent, seven identically prepared samples were tested and an average photocurrent of $1.5 \pm 0.1 \text{ mA cm}^{-2}$ and $2.4 \pm 0.2 \text{ mA cm}^{-2}$ was found under front- and backside illumination, respectively (see inset **Figure 34a**).

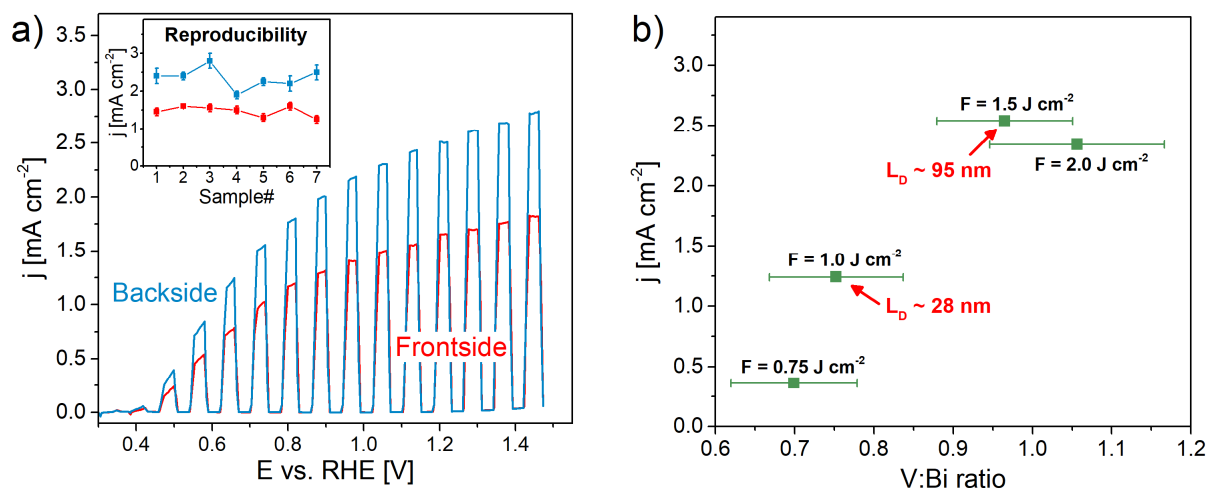


Figure 34. a) Linear sweep voltammetry scan of a BiVO₄ photoanode with a thickness of ~90 nm under chopped front- and backside AM1.5 illumination. The film was deposited with a fluence of 1.5 J cm⁻² onto FTO in vacuum at RT and annealed in air at 450 °C for 2 h. The electrolyte was a 0.5 M KPi-buffer (pH ~7) with 0.5 M Na₂SO₃ as a hole scavenger. The scan rate was 20 mV s⁻¹. Inset: Photocurrent at $E = 1.23$ V vs. RHE of seven identical prepared films on FTO under front- and backside AM1.5 illumination. **b)** Sulfite oxidation photocurrent of films (~90 nm) at a potential of 1.23 V vs. RHE under backside AM1.5 illumination as a function of their V:Bi ratio resulting from different fluences used for the deposition. The V:Bi ratio of the films was determined by RBS calibrated EDX measurements.

Figure 34b depicts the sulfite oxidation photocurrent of films with a thickness of ~90 nm ($E = 1.23$ V vs. RHE, backside AM1.5 illumination) as a function of their V:Bi ratio resulting from depositions with different laser fluences. It can be seen that films deposited with a fluence of 1.5 and 2 J cm⁻²—for which a stoichiometric ablation of the BiVO₄ target is observed in **Figure 28**—show the highest photocurrents. Films deposited with a fluence of 0.75 and 1 J cm⁻², however, only produce a photocurrent of ~0.35 and ~1.25 mA cm⁻², respectively. This is consistent with the significant smaller diffusion length found in Bi-rich films (see **Figure 31**) and with other reports on the detrimental effect of Bi-excess on the PEC performance of BiVO₄.^[140] In addition, it is also consistent with the gradually lower performance of films with a decreasing V:Bi ratio resulting from an increased oxygen pressure during the deposition (see **Figure S 9**). The film deposited in an oxygen pressure of 2.5×10^{-2} mbar (V:Bi ratio of ~0.77) only generates a sulfite oxidation photocurrent of 0.45 mA cm⁻² at $E = 1.23$ V vs. RHE under AM1.5 backside illumination.

To test the films with respect to actual water oxidation, cobalt phosphate (CoPi) was photo-electrodeposited onto the surface and linear sweep voltammetry scans were performed without any hole scavenger. The photocurrent at a potential of 1.23 V vs. RHE increases from ~0.95 mA cm⁻² to ~1.75 mA cm⁻² before and after the surface modification with CoPi (**Figure 35**). This effect is even more pronounced at a more negative potential of 0.6 V vs. RHE for which the photocurrent increases from ~0.03 to ~0.68 mA cm⁻². This improvement is attributed to a reduced surface state recombination rather than an increase in the charge transfer kinetics as recently shown in our institute.^[74] It should be noted that the photocurrents for water oxidation obtained after the surface modification with CoPi are still

lower than the photocurrents obtained when a hole scavenger is used (see **Figure 34a**). This is probably caused by a suboptimal coverage of the BiVO_4 surface by the CoP_i cocatalyst that might still allow recombination via surface states and hence lower the photocurrent.

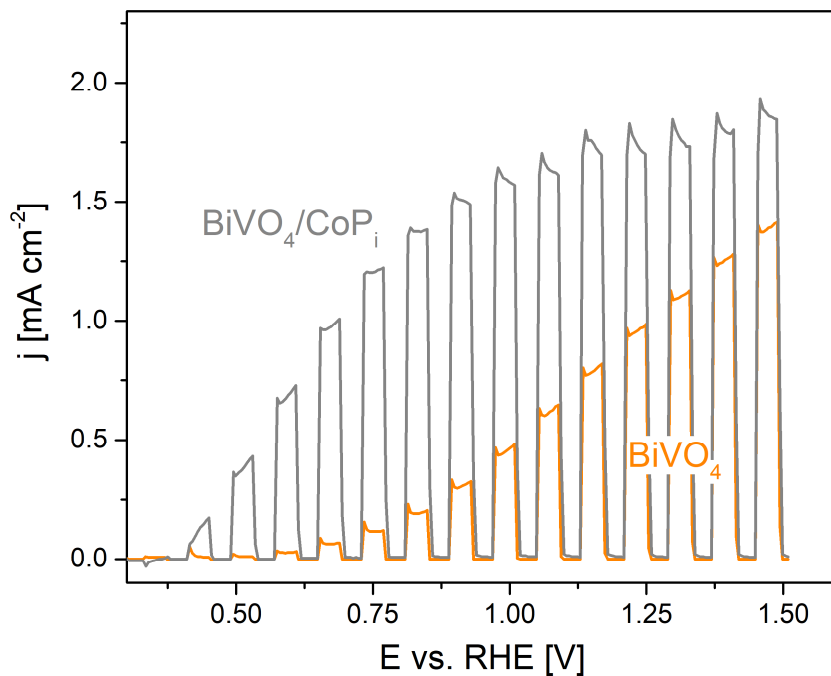


Figure 35. Linear sweep voltammetry scans of a BiVO_4 photoanode with a thickness of ~ 90 nm under chopped backside AM1.5 illumination ($F = 1.5 \text{ J cm}^{-2}$, vacuum, RT, annealing in air at 450°C for 2 h) before and after the deposition of CoP_i . The electrolyte was a 0.5 M KP_i -buffer (pH 7) and the scan rate was 20 mV s^{-1} .

3.5 Alternating target approach

PLD systems equipped with a target carousel also offer the possibility to synthesize complex metal oxide films by the alternating ablation of the respective binary oxide targets.^[107-108] The advantage over the ablation of a complex metal oxide target is that the cation stoichiometry of the film can be adjusted by the number of shots on each target without any restrictions in the PLD process parameters due to deviations from an ideal stoichiometric target-to-substrate transfer. Here, the deposition of BiVO₄ photoelectrodes by the alternating ablation of Bi₂O₃ and V₂O₅ targets is reported for the first time. The process is schematically illustrated in **Figure 36**.

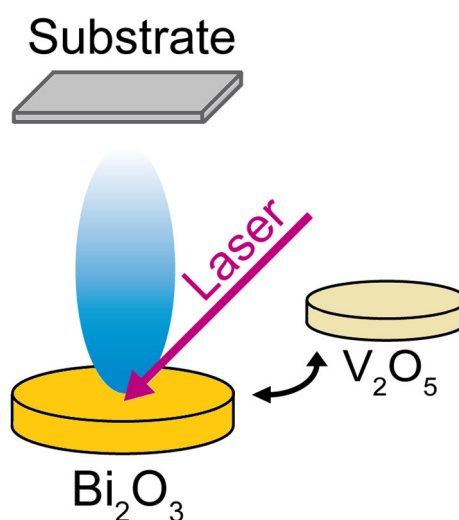


Figure 36. Schematic drawing of the PLD process of BiVO₄ photoelectrodes by the alternating ablation of Bi₂O₃ and V₂O₅ targets.

The deposition parameters were set as follows: the oxygen pressure was 5×10^{-2} mbar, the target-to-substrate distance was 60 mm, the laser fluence was 1.5 J cm^{-2} for both targets and the substrate temperature was 400 °C to allow inter-diffusion of the atoms and obtain crystalline films. To obtain stoichiometric films, the ratio of shots on the V₂O₅ and Bi₂O₃ targets has to be calibrated for this set of parameters. A V₂O₅:Bi₂O₃ shots-on-target ratio of 15 was found to reproducibly result in stoichiometric films (average V:Bi ratio of 0.98 with a standard deviation of 0.01 for four films; see **Figure S 10**). This high ratio is attributed to the faster thermalization of V in the relatively high oxygen background pressure of 5×10^{-2} mbar (see **Figure 29a**). To obtain a film with a thickness of ~90 nm, the deposition cycle of 25 and 375 laser pulses on the Bi₂O₃ and V₂O₅ target, respectively, was repeated 90 times.

Figure 37 shows the X-ray diffraction pattern of a BiVO₄ film deposited using the alternating target approach. Only the reflections belonging to the monoclinic BiVO₄ phase (clinobisvanite, PDF no. 00-014-0688) and the additional reflections from the FTO substrate

are present in the pattern. This shows the successful formation of the BiVO_4 phase by the ablation of a Bi_2O_3 and V_2O_5 target without an additional annealing step.

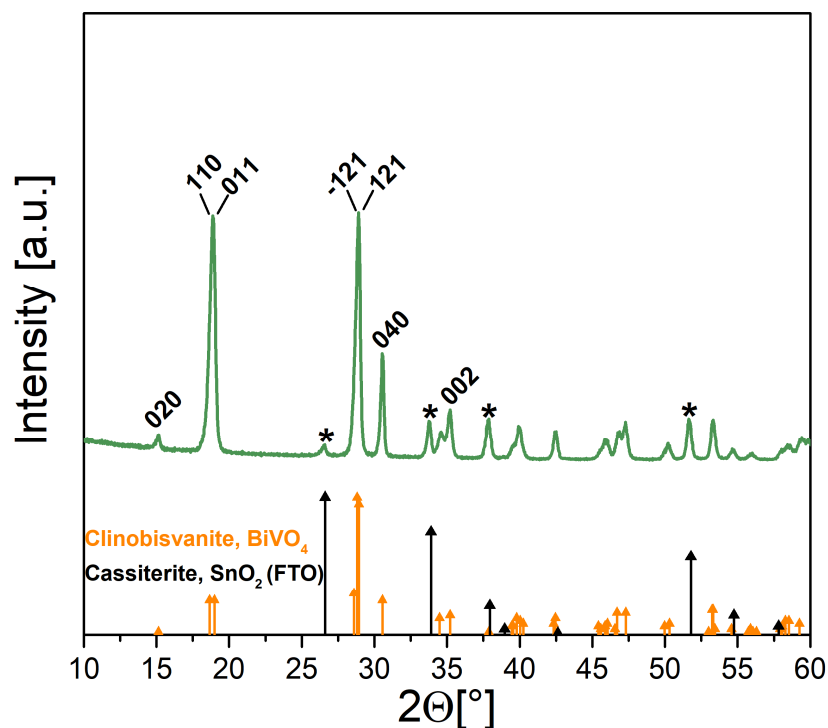


Figure 37. X-ray diffractogram of a BiVO_4 photoelectrode with a thickness of ~ 90 nm deposited on FTO by the ablation of alternating V_2O_5 and Bi_2O_3 targets ($F = 1.5 \text{ J cm}^{-2}$, $p_{\text{O}_2} = 5 \times 10^{-2} \text{ mbar}$, $T_{\text{sub}} = 400^\circ\text{C}$, $\text{V}_2\text{O}_5:\text{Bi}_2\text{O}_3$ shots-on-target ratio = 15). Orange and black lines represent the reference pattern of monoclinic BiVO_4 (PDF no. 00-014-0688) and the underlying FTO substrate (PDF no. 00-041-1445), respectively. The reflections of the FTO are additionally marked with black asterisks (*)

Linear sweep voltammograms of BiVO_4 photoelectrodes prepared by the alternating target approach are shown in **Figure 38**. At a potential of 1.23 V vs. RHE, sulfite oxidation photocurrent densities of up to $\sim 1.4 \text{ mA cm}^{-2}$ and $\sim 2.7 \text{ mA cm}^{-2}$ under front- and backside illumination are achieved, respectively. This technique also shows good reproducibility with respect to the photocurrent, as shown in the inset in **Figure 38**. Five identically prepared samples give an average photocurrent density of $2.6 \pm 0.1 \text{ mA cm}^{-2}$ and $1.2 \pm 0.1 \text{ mA cm}^{-2}$ under back- and frontside illumination, respectively. The photocurrent onset potential is located at $\sim 0.4 \text{ V}$ vs. RHE.

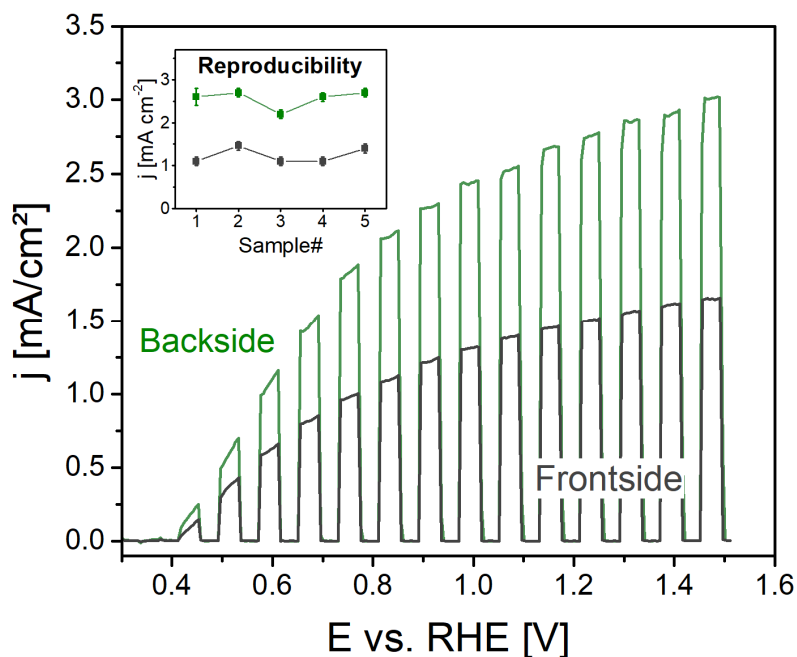


Figure 38. Linear sweep voltammograms of BiVO₄ film with a thickness of ~90 nm under chopped AM1.5 illumination prepared by the alternating ablation of V₂O₅ and Bi₂O₃ targets. ($F = 1.5 \text{ J cm}^{-2}$, $p_{O_2} = 5 \times 10^{-2} \text{ mbar}$, $T_{sub} = 400^\circ\text{C}$, V₂O₅:Bi₂O₃ shots-on-target ratio = 15) The electrolyte was a 0.5 M KPi-buffer (pH ~ 7) with 0.5 M Na₂SO₃ as a hole scavenger. The scan rate was 20 mV s⁻¹ Inset: Photocurrent at $E = 1.23 \text{ V vs. RHE}$ under front- and backside AM1.5 illumination of five identical films prepared by the alternating target approach.

If the two deposition methods to grow polycrystalline BiVO₄ films by PLD (ablating a BiVO₄ target and the alternating target approach) are now compared, it turns out that both techniques give films with similar PEC performance. To further enhance the performance of these films, Mo or W could be introduced as donor dopants to increase the conductivity and thus the charge carrier transport as already reported elsewhere.^[33,141-142] In addition, a hydrogen treatment might enhance the carrier lifetime in our BiVO₄ films via passivation or reduction of deep trap states as recently shown in our institute.^[47] Another possibility is the growth of preferentially oriented films as only recently reported by Han et al.^[50] They prepared preferentially [001]-oriented BiVO₄ photoelectrodes using PLD and achieved an AM1.5 water oxidation photocurrent of 6.1 mA cm⁻² at 1.23 V vs. RHE after roughening the surface and depositing CoPi. This impressive photocurrent for compact films with a relatively high thickness of 800 nm was attributed to an excellent intrinsic charge transport in the [001] direction dispensing the need for nanostructuring. To study this anisotropic charge carrier transport in BiVO₄ in detail, epitaxial films with different orientations are needed. For this, the pulsed laser deposition of BiVO₄ films using the alternating target approach as shown in this thesis is very suitable since the deposition parameters and the V:Bi ratio can be tailored independently.

3.6 Conclusion

In summary, the systematic investigation of the PLD process of BiVO₄ films by ablating a BiVO₄ target showed the complexity of the Bi-V-system due to the very heavy but volatile element Bi. It was found that (i) a preferential ablation of Bi occurs when the laser fluence is too low, (ii) a preferential thermalization of V takes place when an oxygen background pressure is added, and (iii) re-sputtering/re-evaporation of Bi from the substrate at elevated substrate temperatures influences the V:Bi ratio of the deposited film. Based on this, compact and stoichiometric BiVO₄ photoelectrodes with a good electronic quality ($L_D = 90$ nm) could be prepared. These undoped and compact films generated relatively high and reproducible AM1.5 sulfite oxidation photocurrent densities of 2.4 ± 0.2 mA cm⁻² ($E = 1.23$ V vs. RHE, backside illumination). Future efforts on Mo/W doping or an H₂-treatment are believed to further increase the photoactivity of the films. Moreover, the importance of tailoring the deposition parameters in the PLD process of ternary metal oxide photoelectrodes was demonstrated. Already a small difference in the fluence of $\Delta 0.5$ J cm⁻² can result in sub-stoichiometric films that possess three times lower carrier diffusion lengths and significantly lower photoactivities.

In addition, the alternating ablation of V₂O₅ and Bi₂O₃ targets was explored for the first time as an elegant route towards stoichiometric BiVO₄ photoelectrodes. Also with these films, relatively high and reproducible AM1.5 sulfite oxidation photocurrent densities of 2.6 ± 0.1 mA cm⁻² ($E = 1.23$ V vs. RHE, backside illumination) were achieved. This preparation method lays the foundation to grow differently orientated epitaxial films, since the deposition parameters can be tailored without restrictions due to a non-stoichiometric target-to-substrate transfer. These films would be of great value to investigate the anisotropic carrier transport in BiVO₄ photoanodes in detail.

Chapter 4 - α -SnWO₄: a new promising photoanode material for solar water splitting

Parts of this chapter were adapted from:

M. Kölbach, I. J. Pereira, K. Harbauer, P. Plate, K. Höflich, S. P. Berglund, D. Friedrich, R. van de Krol, F. F. Abdi, *Revealing the performance limiting factors in α -SnWO₄ photoanodes for solar water splitting*, **accepted by Chem. Mater.** (DOI: 10.1021/acs.chemmater.8b03883)

M. Kölbach, K. Harbauer, P. Plate, A. Petsiuk, H. Hempel, K. Höflich, V. Deinhart, D. Friedrich, R. Eichberger, F. F. Abdi, R. van de Krol, *Grain boundaries limit charge carrier transport in pulsed laser deposited α -SnWO₄ thin film photoabsorbers*, **in preparation**

4.1 Introduction

Recently, α -SnWO₄ attracted attention as a potential photoanode material due to its following properties: (i) the indirect bandgap is reported to be ~ 1.64 – 2.1 eV and (ii) the flatband potential is reported to be located between -0.14 and 0.05 V vs. RHE (see chapter 1.4.2).^[95-97,99] The combination of these two properties is unique in the search for photoanode materials and could potentially lead to a highly efficient tandem device ($\eta_{STH} > 20\%$), as discussed in chapter 1.3.3 in detail. Several recent studies have reported on thin film α -SnWO₄ photoactive electrodes that were prepared by magnetron sputtering^[95-96] or hydrothermal conversion of WO₃.^[97,99] Up to now, however, all reported α -SnWO₄ photoelectrodes show a very poor PEC performance (AM1.5 photocurrents of < 0.1 mA cm⁻²). This is usually attributed to the oxidation of Sn²⁺ to Sn⁴⁺ in aqueous electrolytes resulting in electron trap sites^[96], hole trapping at Sn-at-W antisite defects within the band gap^[97], and impurity phases in the bulk^[97]. However, the main factor that limits the performance of α -SnWO₄ photoelectrodes is not clear since many key PEC parameters such as the charge carrier diffusion length are still not known.

Therefore, in this chapter, pulsed laser deposited films are used to comprehensively evaluate α -SnWO₄ as a photoelectrode material. In the first part, the PLD process and post-deposition anneal treatment are optimized to obtain phase-pure films. These films are then used to confirm the nearly-ideal bandgap and band positions as reported in the literature. Secondly, the charge carrier dynamics in α -SnWO₄ are elucidated for the first time using TRMC. The charge carrier mobility is found to be increased by more than two orders of magnitude by a controlled high-temperature anneal treatment. This results in one of the highest ever measured carrier diffusion lengths in a metal oxide photoelectrode. By combining TRMC and time-resolved terahertz spectroscopy (TRTS), this improvement could be attributed to larger grain sizes in the heat treated films. Finally, the photoelectrochemical properties are thoroughly investigated. A hole-conducting pulsed laser deposited NiO_x layer is found to protect the surface of α -SnWO₄ from oxidation and thereby drastically improve the photocurrent and the stability.

4.2 PLD process, structural & optical characterization of α -SnWO₄ thin films

Control of the stoichiometry

As shown in the previous chapter, the PLD process parameters have to be carefully optimized to avoid deviations from an ideally stoichiometric target-to-substrate transfer. To investigate the ablation process of a α -SnWO₄ target, the deposited mass was measured with a quartz crystal microbalance as a function of the laser fluence (**Figure 39**). The deposited mass was found to linearly increase with the fluence in the range between 0.5 and 2.5 J cm⁻² indicating no change in the ablation mechanism. This suggests a stoichiometric ablation of the material in the considered fluence regime; a preferential ablation of one element would likely translate into two regimes with different slopes (see chapter 3.2).^[121]

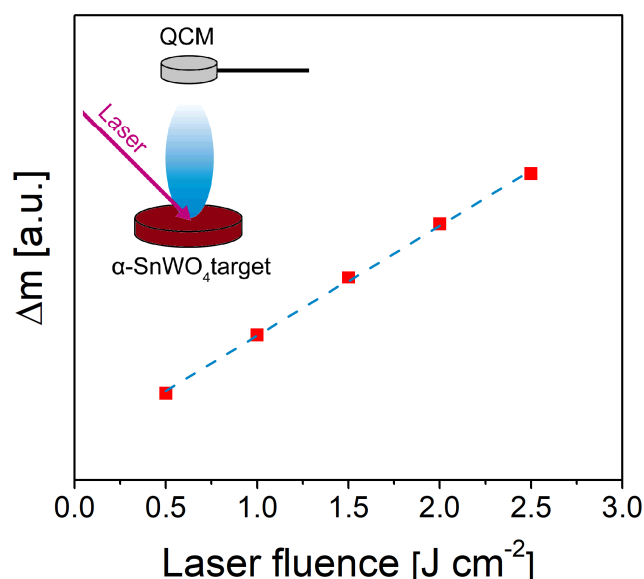


Figure 39. Deposited mass (Δm) during the ablation of a α -SnWO₄ target measured with a quartz crystal microbalance (QCM) as a function of the laser fluence. The target-to-QCM distance was 60 mm.

The preparation of a dense and crack-free α -SnWO₄ target as described in the experimental part (see chapter 2.1.2) was not straightforward. Sintering at a temperature of 650°C did not give the desired density, while a temperature of 750°C resulted in cracks in the target. The latter may be caused by stress effects from the phase transition of α -SnWO₄ to β -SnWO₄ which is reported to occur at ~670°C.^[94] By using an intermediate temperature of 700°C, however, cracking could usually be avoided. It should be noted, however, that minor phase-impurities that can be assigned to Sn_{0.11}WO₃ and SnO₂ were found in the target (**Figure S 11**).

RBS analysis of films deposited on glassy carbon in vacuum at RT shown in **Figure 40a** reveal a slight W-enrichment (Sn:W ratio of ~ 0.9), independent of the laser fluence (see **Figure S 12** and **Figure S 13** for the fitted RBS spectra). This is tentatively ascribed to re-sputtering of Sn from the film during the deposition caused by the high kinetic energy of the impinging species as already reported in other PLD processes.^[21,105,135] This hypothesis is supported by the fact that a relatively high oxygen background pressure (1×10^{-2} mbar) results in a Sn:W ratio closer to ~ 1 (**Figure 40b**). In this case, the ablated species are thermalized by the collisions with the O₂ molecules and do not have a high enough kinetic energy to cause re-sputtering of the film. An element-dependent thermalization of the species (as found in the PLD process of BiVO₄, see chapter 3.2), which would result in a concentration loss of the lighter element Sn in the film, is not observed in this pressure range. This is probably because the ratio of the atomic masses of Sn and its impact partner O₂ is still quite large (3.7).

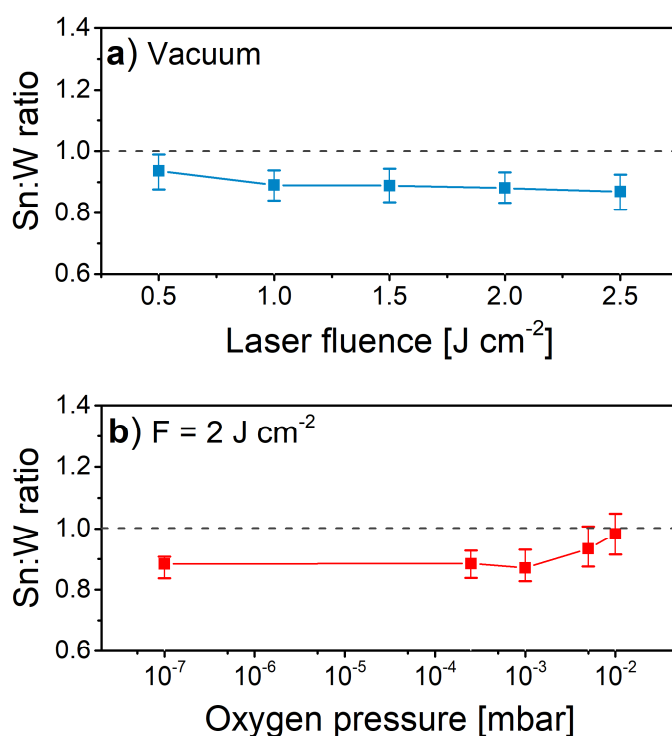


Figure 40. Sn:W ratio measured by RBS of films (~ 100 nm) deposited on glassy carbon at RT by ablating a α -SnWO₄ target in **a**) vacuum under variation of the laser fluence and **b**) in different oxygen background pressures with a fluence of 2 J cm^{-2} . The target-to-substrate distance was 60 mm in all depositions.

Crystal structure & morphology

To obtain crystalline metal oxide films, the PLD process is usually performed at elevated substrate temperatures. In the case of the deposition of α -SnWO₄, however, elevated substrate temperatures resulted in the formation of a metallic Sn phase in the film, probably due to the disproportionation reaction $2 \text{ Sn}^{2+} \rightarrow \text{ Sn}^0 + \text{ Sn}^{4+}$ (see **Figure S 14**).^[143] For this reason,

all the depositions were carried out at RT and an annealing step in an Ar atmosphere was added to crystallize the films. In the previous section, it was already shown that an oxygen pressure is needed to obtain a stoichiometric target-to-substrate transfer. However, the presence of oxygen may also cause oxidation of Sn²⁺ to Sn⁴⁺ and thus change the crystal structure of the films after annealing. To investigate this, **Figure 41** depicts X-ray diffractograms of films deposited on quartz in different oxygen pressures ranging from vacuum ($\sim 10^{-7}$ mbar) to 0.1 mbar before and after an annealing step at 600°C for 2h in an Ar atmosphere. The lower part of **Figure 41** shows that all films deposited at RT are amorphous, independent of the oxygen pressure used during the deposition. After annealing at 600°C for 2h in Ar, however, films deposited in an oxygen background pressure of $\leq 1 \times 10^{-3}$ mbar show the desired and pure α -SnWO₄ phase. It is noted that even though the films are found to be phase-pure by XRD, the films might be slightly W-rich as suggested by the RBS analysis of reference films deposited on glassy carbon (see **Figure 40b**).

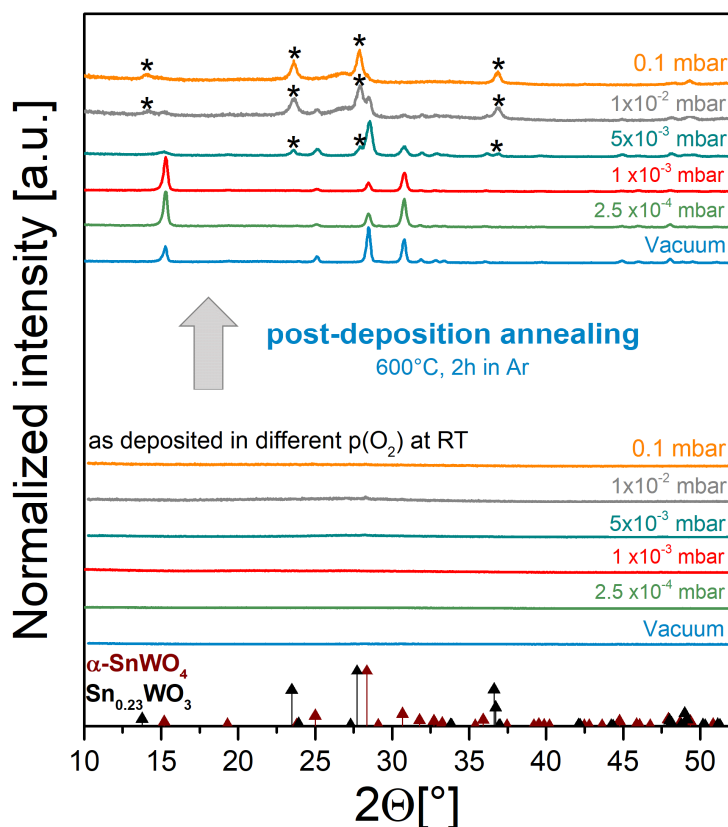


Figure 41. X-ray diffractograms of films deposited on quartz at RT with different oxygen background pressures before and after annealing at 600°C in argon for 2 h. The fluence was 2 J cm^{-2} and the target-to-substrate distance was $d = 60 \text{ mm}$. Brown and black lines represent the α -SnWO₄ (PDF 01-070-1059) and Sn_{0.23}WO₃ (IOCD 81326) reference patterns, respectively. Reflections of the Sn_{0.23}WO₃ phase are marked with black asterisks (*).

In films deposited in an oxygen pressure $\geq 5 \times 10^{-3}$ mbar an impurity phase appears, and its amount increases with increasing oxygen pressure during the deposition. This phase can be assigned to Sn_{0.23}WO₃, a tin tungstate bronze with mixed valence states. It should be noted, that this phase was also present in other reports on α -SnWO₄.^[144-146] This finding is

surprising since **Figure 40b** suggests that increasing the oxygen pressure would result in higher Sn:W ratio; thus, a Sn-rich impurity phase would be expected instead of the observed Sn_{0.23}WO₃. The target-to-substrate distance of 60 mm used during the depositions translates into a critical oxygen pressure (p_c) of 10^{-3} mbar above which gas-phase collisions would start to dominate (see chapter 3.2, equation (39)). Therefore, the formation of the Sn_{0.23}WO₃ phase is tentatively attributed to the oxidation of Sn²⁺ to Sn⁴⁺ during passage from the target to the substrate. Since the overall Sn:W ratio increases, this would then have to be accompanied by the formation of Sn-rich phases after annealing. Apparently, these phases are not detected by X-ray diffraction, probably because they are amorphous. Unfortunately, this hypothesis cannot be proven by XPS analysis, since these films are deposited on non-conducting quartz substrates required for the analysis of the charge carrier dynamics by TRMC and TRTS as shown in the next chapter.

Here it should be noted, that the growth of α -SnWO₄ films by PLD is found to be highly dependent on the choice of substrate. For example, films deposited on conducting molybdenum substrates show no traces of the Sn_{0.23}WO₃ impurity phase, even when an oxygen background pressure of 10^{-2} mbar was used during the deposition (see **Figure S 16**). Therefore, these films cannot be used as reference films to draw conclusions about the oxidation states of Sn in the films on quartz.

To investigate the effect of the annealing temperature on the crystallinity of the α -SnWO₄ films deposited on quartz, the films were annealed for 2h in Ar at temperatures ranging from 500°C to 700°C while keeping the oxygen pressure constant at 2.5×10^{-4} mbar (**Figure 42a**). Films annealed at 500°C and 600°C only show the reflections of α -SnWO₄. Increasing the annealing temperature to 625°C, however, results in the formation of the Sn_{0.23}WO₃ phase, the amount of which increases with temperature up to 700°C. When the annealing temperature is even further increased to 750°C, the film undergoes a phase transformation to β -SnWO₄—the high-temperature polymorph of α -SnWO₄—with small amounts of the Sn_{0.23}WO₃ phase.

It is intriguing that both increasing annealing temperature and high oxygen background pressure during deposition of the films results in the same impurity phase. However, the origin cannot be the same since the background pressure is kept below the pressure at which ablated ions undergo gas phase collisions before reaching the substrate (10^{-3} mbar). Interestingly, the target does not show the Sn_{0.23}WO₃ phase (**Figure S 11**), despite being sintered at 700°C under identical conditions as the films. This suggests that the impurity phase was probably formed due to strain-limited growth of the thin film when subjected to high temperature. The strain may be caused by a lattice mismatch between the quartz (SiO₂) substrate and the film. To test this hypothesis, α -SnWO₄ was deposited with different thickness on Si/SiO₂ substrates. Indeed, the amount of the impurity phase increases with decreasing film thickness (i.e., higher degree of strain, see **Figure S 15**).

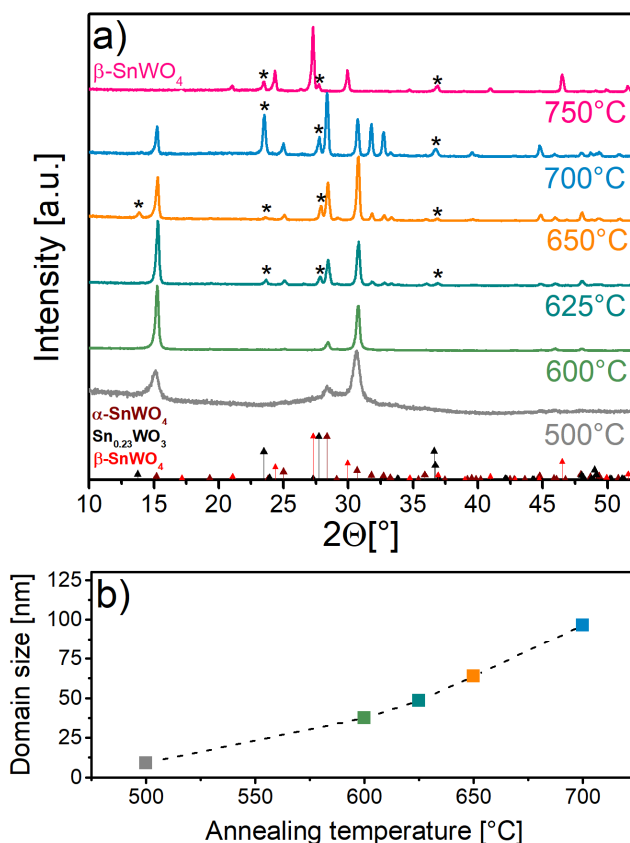


Figure 42. a) X-ray diffractograms of α -SnWO₄ films annealed at different temperatures for 2 h in Ar ($F = 2 \text{ J cm}^{-2}$, $p_{\text{O}_2} = 2.5 \times 10^{-4} \text{ mbar}$). Brown, black and red lines represent the reference pattern of α -SnWO₄ (PDF 01-070-1059), Sn_{0.23}WO₃ (ICSD 81326) and β -SnWO₄ (PDF 01-070-1497), respectively. The reflections of the Sn_{0.23}WO₃ phase are marked with black asterisks (*). b) Coherent scattering domain size of α -SnWO₄ films as a function of the annealing temperature.

The coherent scattering domain size of the α -SnWO₄ films was estimated with the Scherrer equation after fitting the diffractograms with the Le Bail-method and correcting the integral width for the instrumental width (**Figure 42b**). It can be clearly seen that the domain size of the α -SnWO₄ phase increases with increasing annealing temperature from ~9 nm to ~96 nm in films annealed at 500°C and 700°C, respectively.

Figure 43 shows the morphologies of the α -SnWO₄ films annealed at different temperatures recorded by helium ion microscopy (HIM). The as-deposited amorphous film (**Figure 43a**) has a perfectly smooth surface. Upon heat treatment at a temperature of 500°C, small crystalline grains with a size of ~60 nm start to form (**Figure 43b**). When the temperature is increased to 600°C and 625°C, the grains grow up to roughly $(170 \pm 65) \text{ nm}$ and $(180 \pm 65) \text{ nm}$, respectively, and start to coalesce with each other (**Figure 43c** and **d**). In films annealed at temperatures $\geq 625^\circ\text{C}$, the Sn_{0.23}WO₃ phase is detected by XRD (see **Figure 42a**). This phase becomes visible as platelets in the film annealed at 650°C (**Figure 43e**) and becomes even more dominant for an annealing temperature of 700°C (**Figure 43f**). The grain sizes of α -SnWO₄ increase up to $(400 \pm 230) \text{ nm}$ and $(500 \pm 250) \text{ nm}$ for annealing temperatures of 650°C and 700°C, respectively. This increase is accompanied by an

increased inhomogeneity of the size distribution and the formation of voids resulting from the coalescence of grains.

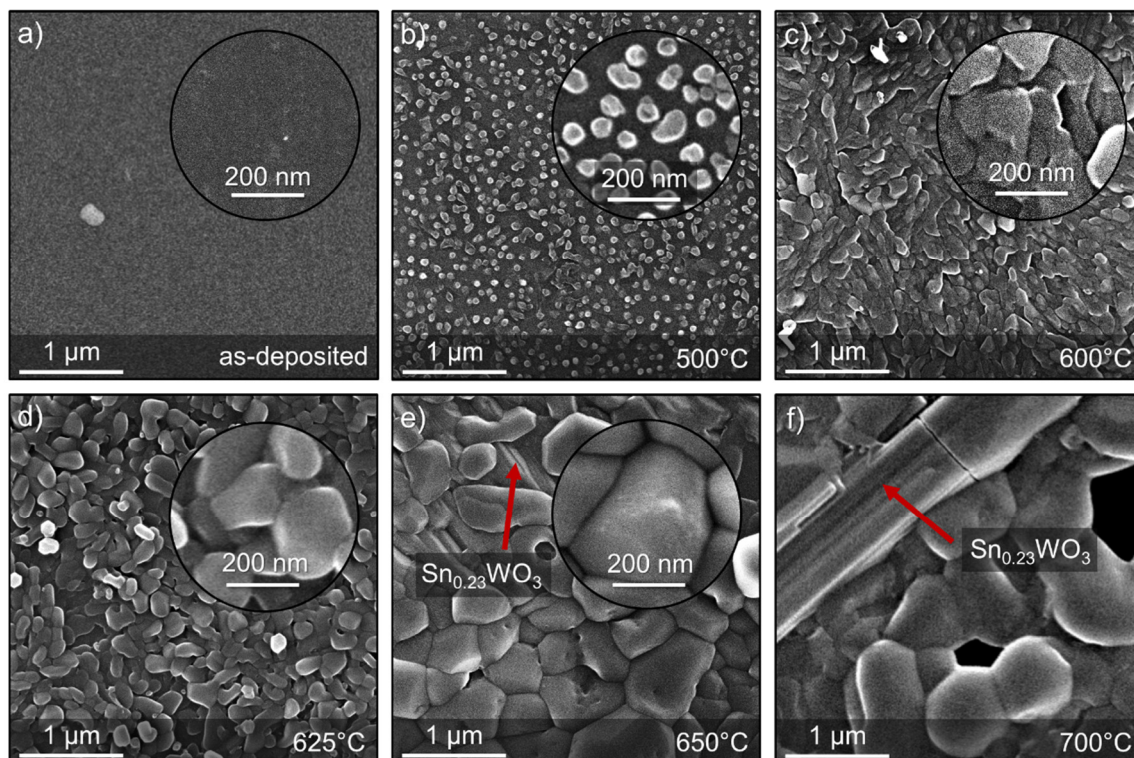


Figure 43. Helium ion microscopy images of quartz/ α -SnWO₄ thin films ($F = 2 \text{ J cm}^{-2}$, $p_{\text{O}_2} = 2.5 \times 10^{-4} \text{ mbar}$, $t = 200 \text{ nm}$). **a)** Image of the as-deposited film. **b) – f)** Images of films annealed at temperatures ranging from 500 to 700°C revealing a steady growth and coalescence of the grains. The Sn_{0.23}WO₃ phase is visible for in the films annealed at 650° and 700°C is indicated by red arrows.

The observed grain sizes by HIM are significantly larger than the coherent scattering domain sizes obtained from XRD measurements (see **Figure 42b**). This discrepancy may be caused by several factors. First, the finite film thickness of around 200 nm may restrict the vertical dimensions of the crystals. In HIM imaging, however, only the lateral dimensions can be measured. Second, hidden grain boundaries as well as stacking faults etc. may not be detected by HIM due to the strong topography of the films, resulting in very weak channeling contrast. Finally, the coherent scattering domain size determination with the Scherrer equation is restricted to sizes $< \sim 100 \text{ nm}$. For larger domain sizes, the integral width of the reflections approaches the instrumental width of our X-ray diffractometer. However, both techniques show the same trend: the crystalline quality of the α -SnWO₄ films improves (i.e., domain/grain size increases) when the annealing temperature is increased up to 700°C.

Optical characterization:

As discussed in chapter 1.3.3, the bandgap and absorption coefficient of a semiconductor are key parameters for the evaluation of new photoelectrode materials. Therefore, the optical properties of α -SnWO₄ films were investigated with UV-VIS spectroscopy. **Figure 44a** shows

the absorption coefficient of a phase-pure (i.e., annealed at 600°C, see **Figure 42a**) α -SnWO₄ film deposited on quartz as a function of the wavelength. In addition, Tauc plots are shown as insets in **Figure 44a** to determine the nature of the optical transitions. An indirect optical transition occurs at 1.9 ± 0.05 eV, which is in agreement with reports in the literature^[97,99], and a direct transition is present at 2.6 ± 0.05 eV. Based on this, α -SnWO₄ is indeed capable to absorb a significant portion of the solar spectrum. A maximum theoretical photocurrent of ~ 17 mA/cm² could theoretically be generated assuming 100% absorption for photons with an energy $E_{ph} > 1.9$ eV of the AM1.5 spectrum.

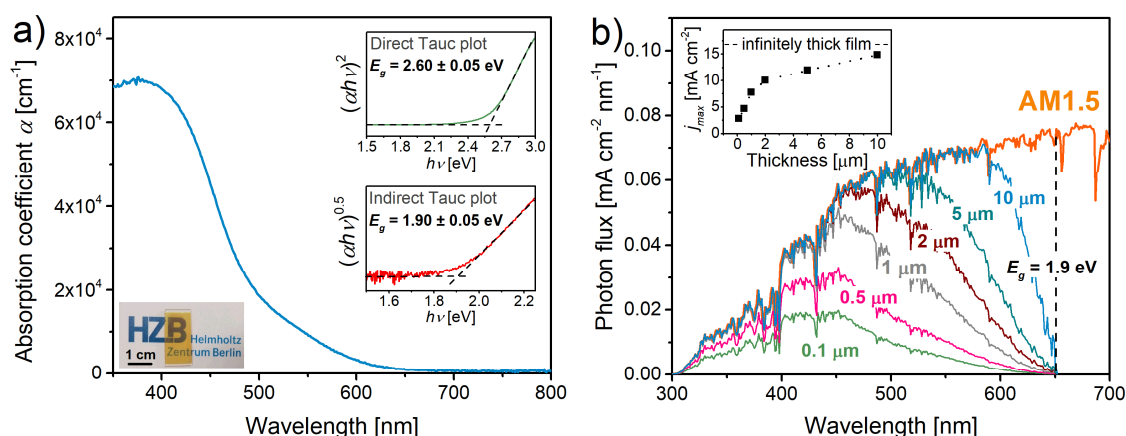


Figure 44. **a)** Absorption coefficient of phase-pure α -SnWO₄ deposited on quartz ($F = 2$ J cm⁻², $p_{O_2} = 2.5 \times 10^{-4}$ mbar, $t = 200$ nm, annealed at 600°C for 2h in Ar) as a function of wavelength. Insets: Optical photograph and direct (green) and indirect (red) Tauc plots. **b)** Absorbable part of the AM1.5 spectrum of α -SnWO₄ films with different thicknesses calculated from the absorption coefficient. The absorption coefficient at the wavelength which corresponds to the bandgap ($\lambda = 653$ nm) was set to zero for the calculation. Inset: Maximum achievable photocurrent density as a function of the α -SnWO₄ film thickness.

Despite the near-ideal bandgap of ~ 1.9 eV, relatively thick films are required to produce high AM1.5 photocurrent densities due to the relatively low absorption coefficient, especially for wavelengths > 450 nm. This is illustrated in **Figure 44b**, which shows the part of the AM1.5 spectrum that can be absorbed by α -SnWO₄ films with thicknesses between 100 nm and 10 μ m. By integrating these curves, the maximum achievable photocurrent density for each thicknesses was obtained (inset of **Figure 44b**) revealing that a film thickness of ~ 1 μ m is required to produce an AM1.5 photocurrent of 7.5 mA cm⁻², and to double the photocurrent to 15 mA cm⁻² a thickness of ~ 10 μ m is needed. Such film thicknesses, however, are one or two order of magnitudes higher than the typical charge carrier diffusion length in complex metal oxide photoelectrodes. The charge carrier dynamics in α -SnWO₄ are discussed in chapter 4.2.

Band positions:

In addition to the bandgap, the energy levels of the valence band maximum and conduction band minimum with respect to the water oxidation/reduction potentials are crucial

parameters to evaluate the potential of a new photoelectrode material (see chapter 1.3.3). Therefore, ultraviolet photoelectron spectroscopy (UPS) was performed to construct the band diagram of α -SnWO₄. As mentioned above, the growth of α -SnWO₄ films by PLD was found to be dependent on the choice of substrate. Since UPS analyses and also the PEC measurements presented in chapter 4.4 require a conducting substrate, α -SnWO₄ films were also deposited on FTO and annealed at 600°C for 2h in Ar. These films were also found to be phase-pure as can be seen in the X-ray diffractogram shown in **Figure 45**.

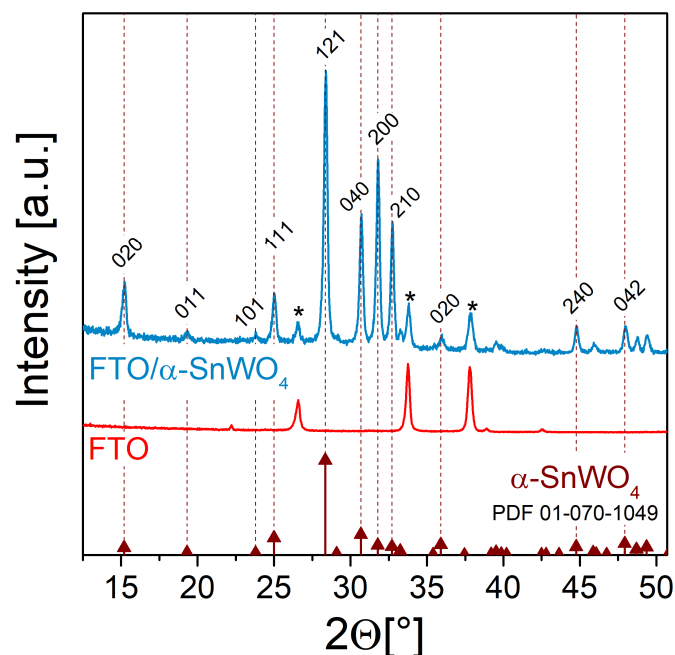


Figure 45. X-ray diffractogram of a FTO/ α -SnWO₄ film ($F = 2 \text{ J cm}^{-2}$, $p_{\text{O}_2} = 2.5 \times 10^{-4} \text{ mbar}$, annealed at 600°C for 2 h in Ar) and the FTO substrate measured with a grazing incidence geometry. The brown lines represent the reference pattern of α -SnWO₄ (PDF no. 01-070-1049). The additional reflections from the FTO substrate in the diffractogram of FTO/ α -SnWO₄ are marked with asterisks (*).

The UPS analysis of the α -SnWO₄ film shown in **Figure 46a** and **b** reveals a work function (Φ) of 4.4 eV (i.e., the Fermi level is located at $\sim 0 \text{ V}$ vs. RHE) and a valence band maximum (VBM) of $1.6 \pm 0.1 \text{ eV}$ below E_F . From these values and the bandgap of $\sim 1.9 \text{ eV}$ determined in the previous section, the band diagram of α -SnWO₄ can be constructed with respect to the redox potentials of the water oxidation and reduction reactions (**Figure 46c**). The band diagram implies that the valence and the conduction band nicely straddle the water oxidation and reduction potentials, respectively, which is in good agreement with other reports in the literature.^[97] In other words, the photogenerated electrons and holes in α -SnWO₄ are in theory thermodynamically able to reduce and oxidize water (see chapter 1.3.3). However, it should be noted that the relatively modest maximum overpotential of $0.33 \pm 0.10 \text{ V}$ available for the OER, which is defined by the position of the valence band maximum, implies that a highly efficient OER catalyst may need to be deposited on the surface of α -SnWO₄.

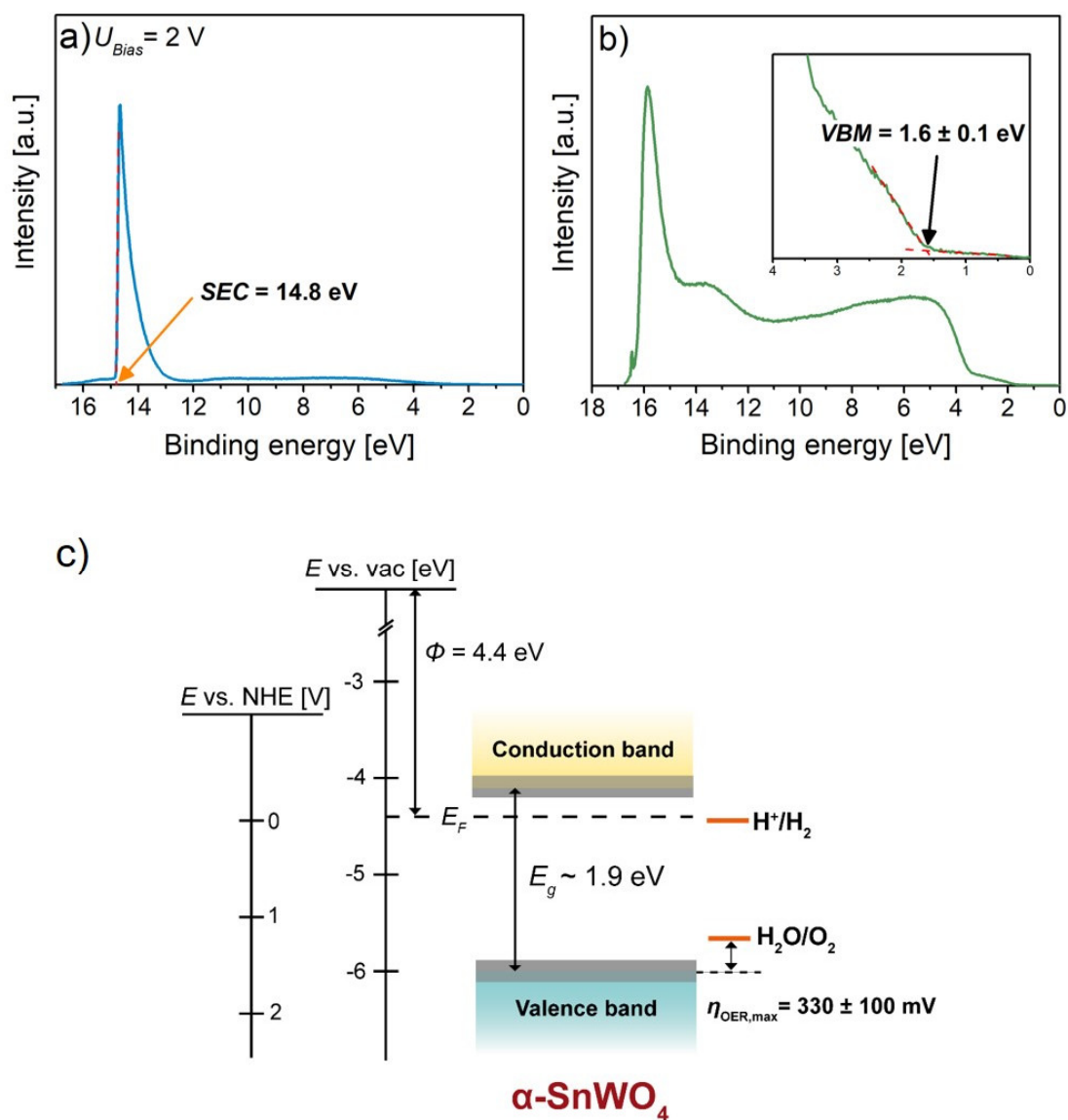


Figure 46. **a), b)** Ultraviolet photoelectron spectroscopy measurements of FTO/ α -SnWO₄ using a He I photon source ($E = 21.2$ eV). **a)** Biased measurement ($E_{bias} = 2$ V) to determine the Secondary Electron Cutoff (SEC) and the work function (ϕ). **b)** Determination of the valence band maximum (VBM) **c)** Schematic band diagram of α -SnWO₄ constructed from UPS measurements in **a)** and **b)**. The positions of the valence band maximum, Fermi level and the conduction band with respect to the vacuum level, the normal hydrogen electrode (NHE) potential, as well as the water oxidation and reduction potentials are depicted.

4.3 Charge carrier dynamics in α -SnWO₄

Another crucial requirement for potential photoelectrode materials is an efficient charge carrier separation in the bulk (see chapter 1.3.3). For n-type semiconductors, such as α -SnWO₄, this implies that the photogenerated holes and electrons must reach the semiconductor/electrolyte interface and the back contact, respectively, before they recombine. Therefore, the charge carrier mobility and lifetime are critical parameters to evaluate new potential photoelectrode materials. To investigate the influence of the PLD synthesis parameters discussed in the previous subchapter on the charge carrier transport in α -SnWO₄ films, time-resolved microwave conductivity (TRMC) measurements are performed (an introduction to this technique was given in chapter 2.2.3).

Figure 47 depicts the peak mobility $(\phi \Sigma \mu)_{max}$ obtained from the maximum of the TRMC signal as a function of the incident photons per pulse (I_0) of α -SnWO₄ films annealed at different temperatures for 2h in an Ar atmosphere. To quantify the mobility, an internal quantum yield of 100% and a dielectric constant of 62.3 were assumed.^[96] The charge carrier mobility of the films is found to improve by more than two orders of magnitude when increasing the annealing temperature from 500 °C to 700 °C. At the lowest light intensity for which a reasonable signal-to-noise ratio can still be obtained, a mobility of $1.7 \times 10^{-3} \text{ cm}^2 \text{ V}^{-1} \text{ s}^{-1}$ and $0.35 \text{ cm}^2 \text{ V}^{-1} \text{ s}^{-1}$ was measured for α -SnWO₄ films annealed at 500 °C and 700 °C, respectively. This remarkable improvement in the mobility is not a result of the Sn_{0.23}WO₃ impurity phase (see chapter 4.2, **Figure 42a**) as discussed later.

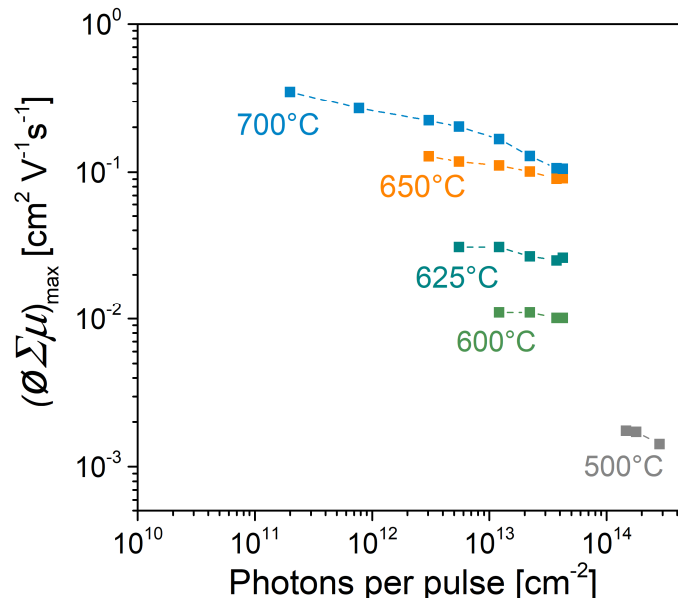


Figure 47. Peak mobility as a function of photons per pulse for α -SnWO₄ films with a thickness of ~200 nm deposited on quartz ($F = 2 \text{ J cm}^{-2}$, $p_{O_2} = 2.5 \times 10^{-4} \text{ mbar}$) annealed at different temperatures. The wavelength of the laser pulse was 355 nm.

The peak mobility of all films depends on the laser intensity and decreases as the light intensity increases, regardless of the annealing temperature (**Figure 47**). This behavior is typically attributed to higher order non-geminate recombination.^[136] For some materials the peak mobility first increases with light intensity, reaching a peak value before it starts to decrease due to non-geminate recombination. The initial increase would indicate the presence of trap states in the semiconductor.^[112,137,147] In the α -SnWO₄ films annealed at different temperatures, this behavior is not observed. While it cannot be ruled out that trap states may be present in lower concentrations (and thus be visible at much lower light intensities) and/or that the trapping process occurs much faster than the ns time scale of our TRMC experiments, the absence of a maximum in the peak mobility signal in **Figure 47** suggests that the carrier mobility values reported here are not limited by the presence of trap states.

Figure 48a shows the TRMC signals obtained at a laser pulse intensity of $2.2 \times 10^{13} \text{ cm}^{-2}$ of films annealed at different temperatures, plotted on a double logarithmic (log-log) scale. After the response time of the TRMC setup ($\sim 10 \text{ ns}$), the signals of all films decay relatively fast until $\sim 100 \text{ ns}$. After that, a much longer decay is observed that follows a power-law ($\phi \Sigma \mu \propto t^{-\gamma}$) up to the selected maximum measurement range of $\sim 9 \mu\text{s}$. The decay constant γ does not significantly change with annealing temperature, yielding values of 0.27, 0.24, 0.30 and 0.21 for the films annealed at 600°C , 625°C , 650°C and 700°C , respectively. A decay of a TRMC signal that follows a power-law behavior is usually ascribed to trap limited recombination processes, in which trapped electrons or holes are temporally unavailable for recombination. Two trap-limited recombination mechanisms have been proposed: (i) multiple trapping and de-trapping at defect states or (ii) carrier tunneling in the semiconductor.^[64,148-151] The exact mechanism of the trap-limited recombination in our α -SnWO₄ films cannot be reliably determined from this set of data and is beyond the scope of this thesis.

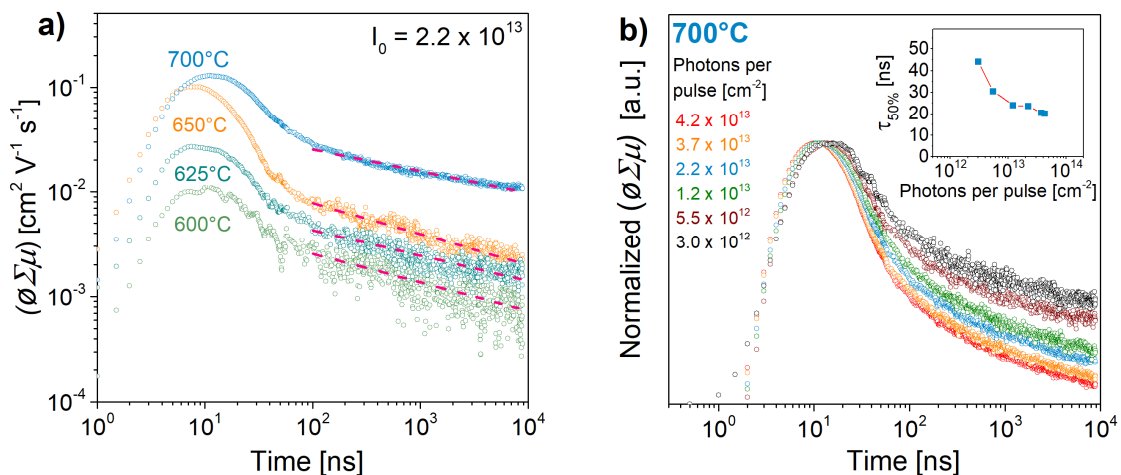


Figure 48. TRMC signals at a laser intensity of $2.2 \times 10^{13} \text{ cm}^{-2}$ ($\lambda = 355 \text{ nm}$) of α -SnWO₄ films deposited on quartz ($F = 2 \text{ J cm}^{-2}$, $p_{\text{O}_2} = 2.5 \times 10^{-4} \text{ mbar}$) and annealed at different temperatures for 2 h in Ar. Dashed lines represent the power-law fit of the signals. **b)** Normalized TRMC signals of a α -SnWO₄ film annealed at 700°C measured with varying laser pulse intensity (photons per pulse). Inset: effective carrier lifetimes ($\tau_{50\%}$) as a function of photons per pulse extracted from the signals.

From the decay of the TRMC signal, the effective carrier lifetime ($\tau_{50\%}$, defined as the time needed for the signal to decrease to 50% of its starting value) can be extracted. The effective lifetime in the α -SnWO₄ films is found to vary between 13 to 23 ns for a laser intensity of $2.2 \times 10^{13} \text{ cm}^{-2}$ and does not show a clear trend with respect to annealing temperature (see **Figure S 17d**).

Figure 48b depicts the normalized TRMC signals of the film annealed at 700°C obtained at different laser pulse intensities. The effective lifetime increases from ~20 to ~44 ns when decreasing the excitation intensity from 4.2×10^{13} to $3.0 \times 10^{12} \text{ cm}^{-2}$ (see inset **Figure 48b**). Although less pronounced, this effect is also present in films annealed at lower temperatures (see **Figure S 17**). This is attributed to the strong intensity dependence of higher order recombination processes, similar to the decrease of $(\phi \sum \mu)_{\text{max}}$ with increasing laser pulse intensity (see **Figure 47**).

From the mobility $(\phi \sum \mu)_{\text{max}}$ and the effective lifetime $\tau_{50\%}$ (each determined at the lowest intensity that still gives a reasonable signal-to-noise-ratio), the effective charge carrier diffusion lengths in our α -SnWO₄ films annealed at 600°C, 625°C, 650°C, and 700°C are calculated to be ~25 nm, ~40 nm, ~70 nm and ~200 nm, respectively.

Now we turn our attention to the identification of the cause of the dependence of the charge carrier mobility in α -SnWO₄ on the annealing temperature. The most obvious effect of higher annealing temperatures is the formation of the Sn_{0.23}WO₃ impurity phase (see **Figure 42a**). If this impurity phase possesses much higher mobility than α -SnWO₄, the increasing amount with higher temperature would indeed result in higher observed TRMC mobility. However, this can be ruled out due to the following findings: (i) TRMC analysis of the films deposited in oxygen background pressures $\geq 5 \times 10^{-3}$ mbar show a decreasing charge carrier mobility with increasing concentration of the Sn_{0.23}WO₃ phase (see **Figure S 18**), and (ii) a prolonged annealing for 32 h at 600°C in Ar also results in an increase of the Sn_{0.23}WO₃ content; the mobility, however, does not change significantly (see **Figure S 19**).

Another possible cause for the improved mobility with increasing annealing temperature could be the passivation of deep and/or shallow defects states. If this would be the case in our films, the effective carrier lifetime is expected to increase with higher annealing temperatures. As shown in **Figure S18d**, however, the effective lifetime does not show such a trend; this explanation can therefore be ruled out.

Instead, the most likely reason is the improvement of the crystalline quality (i.e., larger domain/grain sizes) of the films with increasing annealing temperature (see chapter 4.2, **Figure 42b** and **Figure 43**). Such a grain size dependence of TRMC-obtained carrier mobilities was already reported in other material systems, as for example by Kroeze et al. in TiO₂ particles^[114] and by Reid et al. in MAPbI₃ thin films.^[139] This dependence can be understood by applying the fluctuation-dissipation theorem that connects the TRMC-obtained mobilities with the mean-squared displacement of the charge carriers in a quasi-thermal

equilibrium and a weak probe electric field.^[139] When charge carriers are confined by grains so that the mean-squared displacement is reduced relative to freely diffusing charge carriers on the time scale of the microwave probe period ($T_{\text{TRMC}} = 118$ ps), the measured mobility will be affected.

Collisions of the charge carriers with the grain boundaries, which may lower the mobility, is affected by the random diffusion motion of the charge carriers as well as the field-induced carrier oscillation by the microwave probe. In our TRMC setup, the maximum electric field of the microwave probe ($f = 8.5$ GHz) is 6 V cm^{-2} . With the highest measured carrier mobility in our α -SnWO₄ films of $\sim 0.35 \text{ cm}^2 \text{ V}^{-1} \text{ s}^{-1}$, this translates into a field-induced charge carrier oscillation of only ~ 2.5 pm in one period of the microwave probe (~ 118 ps). This is orders of magnitude smaller than the random diffusion motion of the charge carriers in ~ 118 ps (estimated to be ~ 10 nm); random diffusion is therefore the dominant mechanism here.

To confirm this hypothesis of the detrimental effect of grain boundaries on the carrier mobility in our α -SnWO₄ films, time-resolved terahertz spectroscopy (TRTS) was also performed.^[152] In comparison to TRMC measurements, charge carriers in TRTS are generated with a 150 fs laser pulse and are probed with a THz pulse. Therefore, the diffusion length of the charge carriers in our α -SnWO₄ films in one oscillation ($T_{\text{TRTS}} = 1$ ps) is more than one order of magnitude lower than in one oscillation of the microwave probe in TRMC measurements ($T_{\text{TRMC}} = 118$ ps). The difference is illustrated in **Figure 49a**. As a consequence, the TRTS-obtained charge carrier mobilities are much less affected by the grain size of the film.^[153-154] In other words, if grain boundaries really limit the carrier transport in our α -SnWO₄ films, no (or a smaller) dependence of the TRTS-obtained mobilities on the annealing temperature should be observed. It should be noted that even though the electric field of the THz probe is higher ($\sim 1000 \text{ V/cm}$), it still induces only a small charge carrier oscillation of 0.07 nm ($\mu = 0.35 \text{ cm}^2 \text{ V}^{-1} \text{ s}^{-1}$) in one period of the THz probe compared to the random diffusion motion of the charge carriers in TRMC measurements.

Figure 49b and **c** show the TRTS photoconductivity transient of films annealed at 600°C and 700°C (analysis of the data is shown in **Figure S 20**). After only ~ 5 ps the signal already decayed to $\sim 30\%$ of its starting value and stays constant up to 100 ps. The elucidation of the underlying mechanism of this initial decay (e.g., trapping or polaron formation) is out of the scope of this work and requires further study. Despite this decay and the relatively poor signal-to-noise ratio, a mobility (after 5 ps) of $\sim 0.09 \text{ cm}^2 \text{ V}^{-1} \text{ s}^{-1}$ and $\sim 0.22 \text{ cm}^2 \text{ V}^{-1} \text{ s}^{-1}$ can be estimated for the films annealed at 600°C and 700°C , respectively. This difference in the mobility is indeed much smaller than the one order of magnitude difference found in the TRMC-obtained mobilities for these temperatures. This comparison is illustrated in **Figure 49d**, which depicts both the TRMC- and TRTS-obtained mobilities as a function the domain size determined with XRD (see **Figure 42b**). Therefore, it can be concluded that grain boundaries are limiting the charge carrier transport in our α -SnWO₄ films and that the heat treatment does not significantly increase the intrinsic (intragrain) mobility.

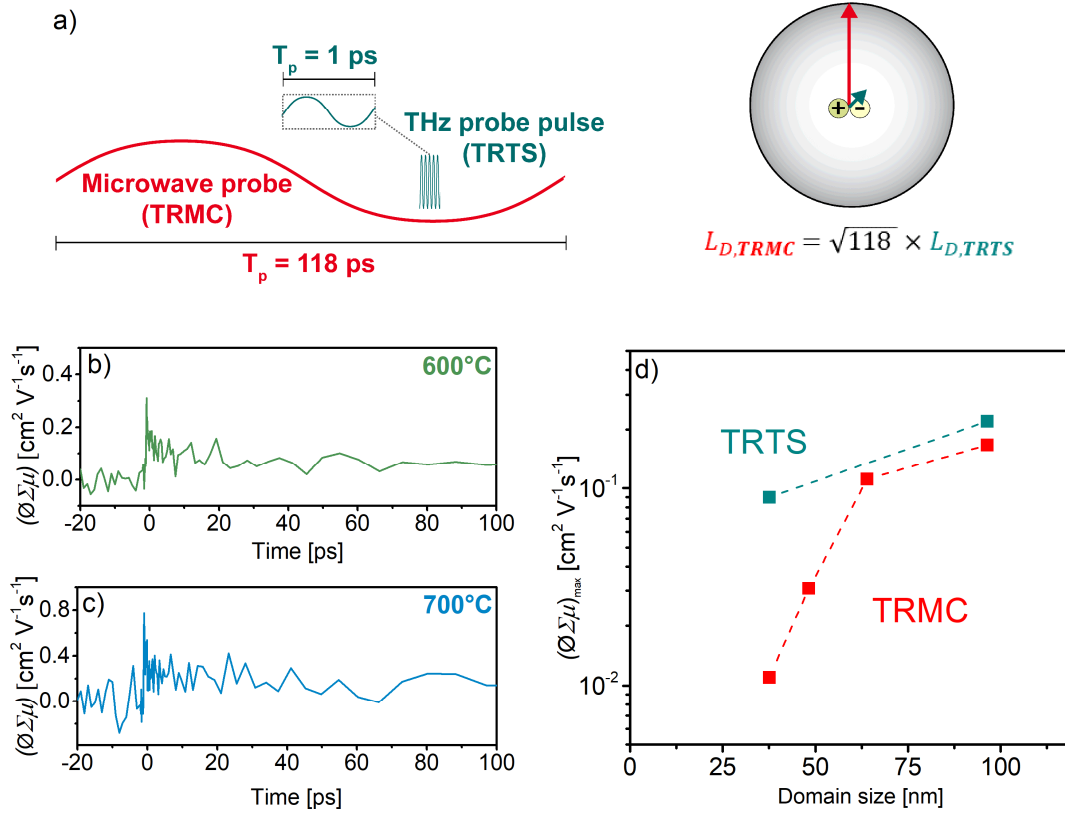


Figure 49. a) Comparison of the probe in TRMC (microwave) and TRTS (THz pulse) measurements and the resulting difference in the random diffusion motion (L_D) of confined charge carriers in a grain during one oscillation of each probe. b), c) TRTS signals obtained for α -SnWO₄ films annealed at 600°C and 700°C in Ar for 2 h. The excitation laser pulse intensity was $7.0 \times 10^{13} \text{ cm}^{-2}$ and the wavelength was 400 nm. d) TRMC- and TRTS-obtained carrier mobilities of α -SnWO₄ films as a function of the domain size resulting from annealing at different temperatures. The laser intensity was $2.2 \times 10^{13} \text{ cm}^{-2}$ ($\lambda = 355 \text{ nm}$) and $7.0 \times 10^{13} \text{ cm}^{-2}$ ($\lambda = 400 \text{ nm}$) in the TRMC and TRTS analysis, respectively.

To benchmark the carrier transport properties of α -SnWO₄ found in this thesis with other metal oxide photoelectrode candidates, the carrier mobilities and lifetimes of various complex metal oxide photoelectrodes obtained by TRMC are summarized in **Figure 50**. The contour lines represent the calculated effective charge carrier diffusion length as a function of carrier lifetime and mobility. It should be noted that this overview only provides a rough comparison, since it does not address light intensity dependence, trap filling behavior, different film qualities (grain size/defect concentration), and different charge transport mechanisms. Compared to other metal oxide photoelectrode materials, the carrier mobility of $0.35 \text{ cm}^2 \text{V}^{-1} \text{s}^{-1}$ in α -SnWO₄ (annealed at 700°C) is very high, while the effective charge carrier lifetime of 44 ns is rather modest. The resulting value of the carrier diffusion length of 200 nm is in the same order as the diffusion length of the promising photocathode material CuFeO₂, outperforms BiVO₄, and is 1-2 order of magnitudes higher than that of metal oxides with comparable bandgaps, such as α -Fe₂O₃ ($E_g \sim 2.1 \text{ eV}$), FeVO₄ ($E_g \sim 2.0 \text{ eV}$) or CuBi₂O₄ ($E_g \sim 1.8 \text{ eV}$).

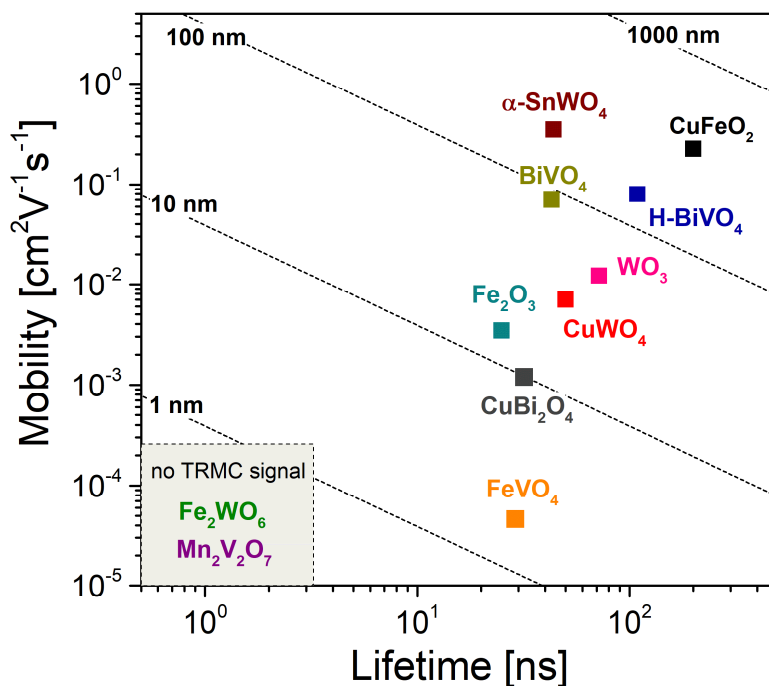


Figure 50. Mobility vs. lifetime plot of various metal oxide photoelectrodes measured with TRMC: α -SnWO₄ (this work), CuFeO₂^[155], BiVO₄^[47], hydrogen-doped BiVO₄ (H-BiVO₄)^[47], WO₃^[156], Fe₂O₃^[157], CuWO₄^[157], CuBi₂O₄^[158], FeVO₄^[64], Fe₂WO₆^[69] and Mn₂V₂O₇^[157]. Contour lines represent the calculated effective charge carrier diffusion length.

Despite the relatively good carrier transport properties of α -SnWO₄ (for a metal oxide semiconductor), these results clearly show that there is a significant mismatch between the film thickness needed to obtain high AM1.5 photocurrent densities (see **Figure 44b**) and the effective carrier diffusion length of \sim 200 nm. Several strategies exist to overcome this mismatch. First, modification of the bulk material by doping or hydrogen treatment has been shown to increase the electronic conductivity, passivate defects, and/or increase the carrier diffusion length in metal oxide photoelectrodes.^[33,43-47] Second, a nanostructured morphology can be fabricated in order to orthogonalize the direction of carrier transport and light absorption. For example, a nanostructured scaffold or nanostructured bottom absorber can be coated with a thin layer of α -SnWO₄ so that enough photons can be absorbed in the nanostructured α -SnWO₄ yet the carriers need to travel only very short distance to the interfaces. Third, the application of plasmonic resonators could also help to increase the optical absorption in α -SnWO₄ films as already shown for other metal oxide photoelectrodes.^[92,159-160] Finally, the preparation of α -SnWO₄ might also be further optimized. As shown in **Figure 40a**, the films seem to be slightly W-rich which could result in defects acting as efficient recombination centers. Here, the alternating target approach as discussed in chapter 3.5 could be used to grow highly stoichiometric films which might improve the carrier transport. In addition, since carrier transport in α -SnWO₄ is believed to be anisotropic^[96], epitaxial films with well-chosen orientations could be prepared, which may lead to a higher effective carrier diffusion length as was recently shown for preferentially [001]-oriented BiVO₄ photoelectrodes.^[50]

4.4 Photoelectrochemical characterization & NiO_x protection layer

To test the photoelectrochemical performance of α -SnWO₄ films deposited on FTO substrates, a constant voltage of 1.23 V vs. RHE was applied under chopped AM1.5 illumination in a KP_i (pH 7) buffer solution containing 0.5 M Na₂SO₃. The results are shown in **Figure 51a**. Since stability was reported to be an issue in α -SnWO₄ photoelectrodes,^[96-97,99] this chronoamperometry measurement was chosen instead of a typical cyclic voltammetry analysis to better distinguish between photocorrosion and a photocurrent resulting from a charge injection in to the electrolyte. In addition, Na₂SO₃ was added as a hole scavenger to the electrolyte to avoid kinetic limitations due to the oxygen evolution reaction (OER) in the first place.

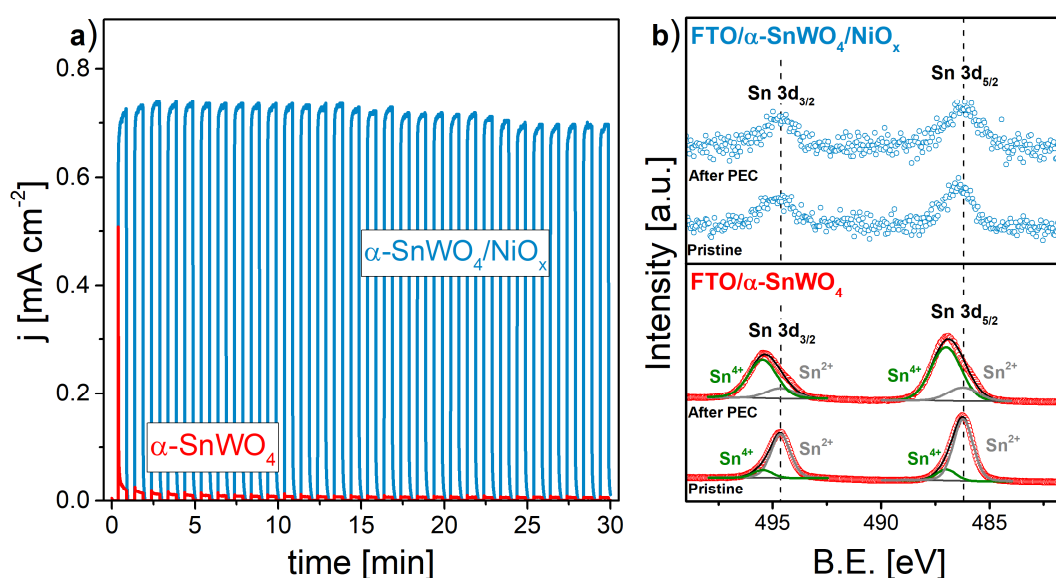
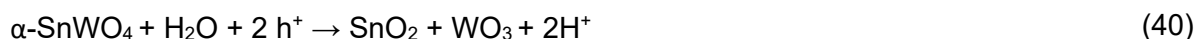


Figure 51. **a)** Sulfite oxidation stability measurement of 100 nm thick FTO/ α -SnWO₄ photoelectrodes ($F = 2 \text{ J cm}^{-2}$, $p_{\text{O}_2} = 2.5 \times 10^{-4} \text{ mbar}$, annealed at 600°C for 2h in Ar; XRD data is shown in **Figure 45**) with and without a 20 nm NiO_x protection layer at a potential of 1.23 V vs. RHE under chopped AM1.5 illumination (dark currents are subtracted). The electrolyte was 0.5 M KP_i-buffer solution (pH 7) and 0.5 M Na₂SO₃. **b)** XPS analysis of the Sn 3d region of the respective films before and after the stability measurement. B.E. = binding energy.

Figure 51a reveals that as soon as the potential is applied to the α -SnWO₄ photoanode, a rapid drop of the photocurrent to values $< 10 \mu\text{A cm}^{-2}$ is observed (red curve). This is attributed to the oxidation of Sn²⁺ in the film according to the following equation as already reported elsewhere^[97]:



This is supported by the XPS analysis of the Sn 3d_{5/2} and Sn 3d_{3/2} doublet peaks of the films before and after the PEC measurement, as shown in **Figure 51b** (bottom panel). The surface of the pristine α -SnWO₄ film shows mostly Sn²⁺ (B.E. of 486.2 eV for 3d_{5/2} and 494.6 eV 3d_{3/2}) and a small amount of Sn⁴⁺ (B.E. of 487.0 eV for 3d_{5/2} and 495.5 eV 3d_{3/2}). The ratio of

$\text{Sn}^{4+}:\text{Sn}^{2+}$ in the film was estimated to be 0.17. The binding energies of the fitted peaks are in good agreement with other reports on the XPS analysis on Sn3d region in the literature.^[97-98,161] After the PEC measurement, the surface mostly shows Sn^{4+} species as evident from the clear shift of the Sn 3d_{5/2} and Sn 3d_{3/2} peaks towards higher binding energies.

No apparent difference can be observed in the W 4f spectra of the film before and after the PEC measurement (see Figure S 22). However, the Sn:W ratio in the film increases significantly from ~1.1 to ~1.5 after the PEC measurement. This is in accordance with equation (40), since WO₃ is only stable in acidic pH^[162] and it may simply dissolve after it is formed during the measurement.

It should be noted that the Sn^{4+} peak observed in the pristine film may not originate from the underlying FTO (SnO₂:F) substrate (pinholes in the 100 nm thick α -SnWO₄ film) since a reference film prepared on a molybdenum substrate also shows the presence of Sn^{4+} species (see **Figure S21**). The exact origin of the Sn^{4+} species and their influence on the PEC properties is not entirely clear at this point. However, it is suspected that the presence of Sn^{4+} is a result of the presence of the SnO₂ impurity phase in the target (**Figure S 11**).

Despite the oxidation of Sn^{2+} to Sn^{4+} and the significant decrease of the photocurrent, no film degradation is visible by eye after PEC measurements (see inset **Figure S 23**). In addition, high-resolution scanning electron microscopy (HRSEM) images of the pristine and PEC tested surface reveal no morphological changes (**Figure 52b**). This suggests that after a certain time, the SnO₂ layer at the surface passivates the film and protects it from water exposure and further oxidation. Assuming that only the current spike **Figure 51a** is attributed to the oxidation of Sn^{2+} to Sn^{4+} , the thickness of the SnO₂ layer passivation layer can be estimated to be ~6 nm (see **Figure S 23**). This is in agreement with the fact that Sn^{2+} can still be detected with XPS after the PEC measurement (detection depth of Sn through SnO₂ is calculated to be ~5.4 nm with the QUASES software package^[163]), which strongly supports the hypothesis that the oxidation of Sn^{2+} stops after a certain point.

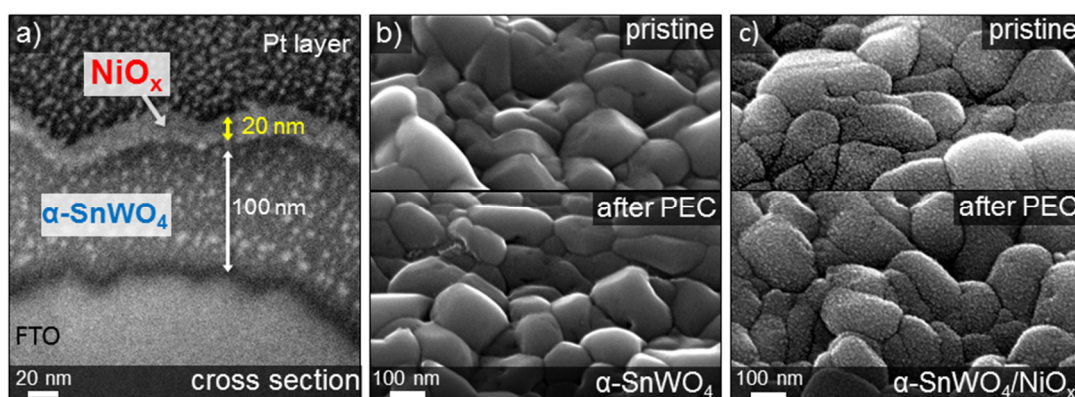


Figure 52. HRSEM images of α -SnWO₄ photoelectrodes. **a)** Cross section of a pristine α -SnWO₄/NiO_x photoanode. The double arrows indicate the layer thicknesses in tilted view projection. The platinum layer on top was deposited to protect the film from ion-induced damage during the preparation of the cross section. **b,** **c)** Surface morphology of the α -SnWO₄ photoanodes before and after PEC measurements **b)** with and **c)** without a NiO_x protection layer.

The poor PEC performance of the α -SnWO₄ probably results from the SnO₂ layer. The valence band edge of SnO₂ is much more positive than the valence band of α -SnWO₄ (see **Figure S 24**). Therefore, the SnO₂ acts as a barrier for the photogenerated holes in α -SnWO₄ preventing them from reaching the electrolyte. Such a hole blocking layer is commonly utilized in n-type metal oxide photoelectrodes where SnO₂ is deposited as a 'hole mirror' in between for example BiVO₄ and the FTO back contact. As a result, electron-hole recombination at the FTO/photoelectrode interface is prevented and the photocurrent is increased.^[164-165]

In order to protect the surface of the α -SnWO₄ films from oxidation, a 20 nm hole conducting NiO_x layer was pulsed laser deposited on top on the films as can be seen in the SEM cross section (**Figure 52a**). **Figure 51a** shows that the NiO_x layer has a drastic effect on the PEC performance of α -SnWO₄. The photocurrent at a potential of 1.23 V vs. RHE increases from several $\mu\text{A cm}^{-2}$ to $\sim 0.75 \text{ mA cm}^{-2}$. The reproducibility of this improvement has been confirmed by measuring 7 identically prepared α -SnWO₄/NiO_x photoelectrodes resulting in an average photocurrent of $0.73 \pm 0.05 \text{ mA cm}^{-2}$ (**Figure 53**). This value is the highest photocurrent ever reported for α -SnWO₄ photoelectrodes.

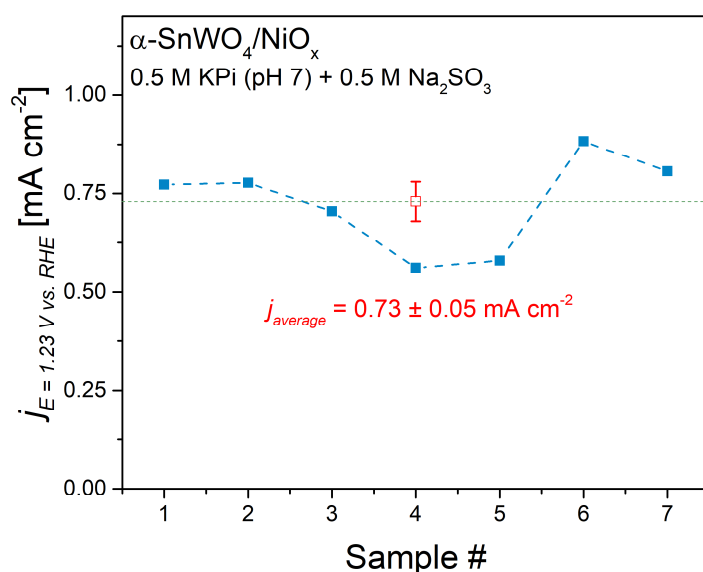


Figure 53. Reproducibility of the photoelectrochemical performance of α -SnWO₄/NiO_x photoelectrodes. The photocurrent at a potential of 1.23 V vs. RHE in 0.5 M KPi (pH 7) with 0.5 M Na₂SO₃ under AM1.5 frontside illumination was chosen as a figure of merit.

The chronoamperometry of the α -SnWO₄/NiO_x film also reveals a very good stability (**Figure 51a**). After the first ~ 100 s of the measurement, a total charge of 40 mC cm^{-2} has passed through the film, which is already enough to fully oxidize all the Sn²⁺ in the film. Considering that a steady chopped photocurrent of $\sim 0.75 \text{ mA cm}^{-2}$ is maintained for ~ 30 min, a Faradaic efficiency of more than 90% towards SO₃²⁻ oxidation can be estimated. In addition, HRSEM images shown in **Figure 52c** of the protected films reveal no morphology differences before and after the PEC measurement. The XPS analysis of the Sn 3d region of

the α -SnWO₄/NiO_x film before and after PEC measurement shown in **Figure 51b** (top panel) indeed indicates that the NiO_x prevents the oxidation of Sn²⁺ to Sn⁴⁺. Although the signals are relatively noisy (the detection depth of Sn²⁺ through the NiO_x is only ~ 5.1 nm^[163]), it is clear that the peak positions are unchanged, in contrast to what is observed for the unprotected film. It should be noted that the fact that Sn²⁺ can still be detected through the ~ 20 nm NiO_x layer indicates a non-conformal growth of the NiO_x film.

Figure 54 depicts linear sweep voltammograms (LSV) of α -SnWO₄/NiO_x with different redox couples under chopped AM1.5 illumination. The LSV of α -SnWO₄/NiO_x with Na₂SO₃ added as a hole scavenger reveals a very negative photocurrent onset potential ~ -0.1 V vs. RHE. This is consistent with the energy level of the conduction band minimum of ~ -0.3 V vs. RHE as obtained from UPS measurements (see chapter 4.2, **Figure 46c**). However, the sulfite oxidation photocurrent remains low, in the range of several $\mu\text{A cm}^{-2}$, at potentials below ~ 0.8 V vs. RHE, after which both the dark current and the photocurrent increase significantly. The high dark current is attributed to the presence of pinholes in the α -SnWO₄ film, resulting in direct contact between the NiO_x film and the FTO substrate. Indeed, NiO_x-coated FTO shows a much higher sulfite oxidation dark current as compared to the bare FTO (see **Figure S 25**). The reason for the sharp increase at potentials positive of $0.8 V_{\text{RHE}}$ will be discussed below.

To distinguish between electron or hole transport limitations, front- and backside illumination experiments were also performed.^[164] However, no significant difference in the photocurrent is observed (see **Figure S 26**), simply because the decay of the AM1.5 intensity for photons with energy higher than the bandgap of α -SnWO₄ ($E_{ph} > 1.9$ eV) in our 100 nm films does not result in substantial light intensity gradient (see inset **Figure S 26**). Therefore, no conclusions with respect to electron or hole transport limitations can be drawn from this experiment.

To show that α -SnWO₄/NiO_x films are also capable of oxidizing species with a more positive oxidation potential than SO₃²⁻ ($E_{ox} \sim 0.65$ V vs. RHE, see **Figure S 27a**), RuCl₃ ($E_{ox} \sim 1.16$ V vs. RHE, see **Figure S 27b**) was also used as a hole scavenger (**Figure 54a**). Interestingly, significant photocurrents are only present for potentials more positive than ~ 0.8 V vs. RHE, as was also observed in the LSV using Na₂SO₃ as a hole scavenger. A photocurrent onset potential that is much more positive than the flatband potential is usually attributed to hole accumulation at the surface resulting from a poor charge transfer kinetics into the electrolyte.^[9] However, since a hole scavenger is used, it is more likely that trap states at the α -SnWO₄/NiO_x interface at an energy level corresponding to ~ 0.8 V vs. RHE are the reason. For potentials $< \sim 0.8$ V vs. RHE, these states pin the Fermi level and are partially occupied with electrons. Presumably, these states also act as recombination centers for the photo-generated holes. For potentials $> \sim 0.8$ V vs. RHE, the Fermi level drops below these states, lower the occupation probability and thus lower the recombination rate. Similar behavior has been recently reported for charged surface states in GaN photoanodes.^[166]

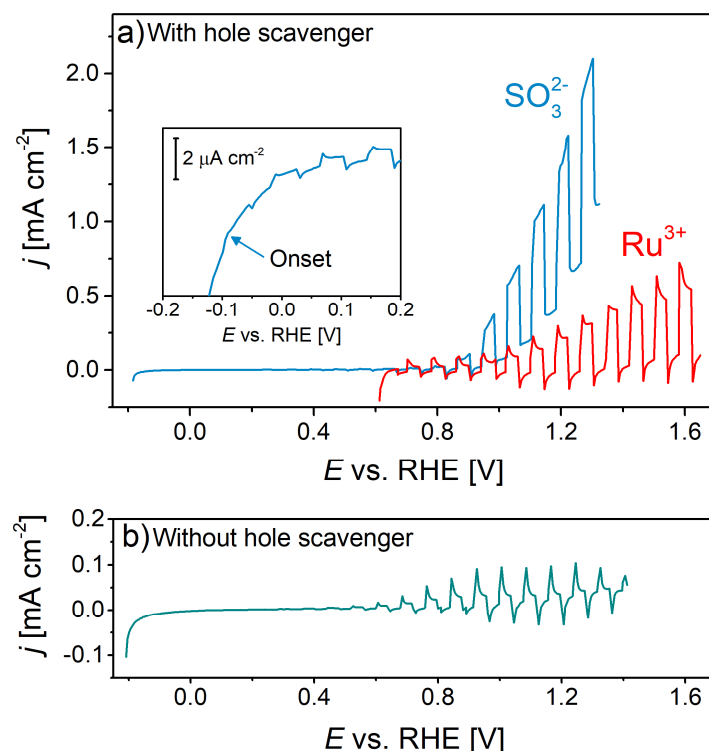


Figure 54. Linear sweep voltammograms of α -SnWO₄/NiO_x films in 0.5 M KPi (pH7) under backside AM1.5 illumination with **a)** 0.5 M Na₂SO₃ or 5 mM RuCl₃ added as a hole scavenger and **b)** without any sacrificial agent. The scan rate was 20 mV s⁻¹.

Corroborating evidence for Fermi level pinning in α -SnWO₄/NiO_x photoanodes was obtained by measuring the intensity-dependent change of the open circuit potential (ΔOCP) in the dark and under illumination (see **Figure S 28**). For α -SnWO₄ films without a NiO_x protection layer, the ΔOCP saturates at the highest illumination intensities resulting in a maximum value of ~ 0.23 V. This is a typical value for band bending in an n-type semiconductor. The ΔOCP of the α -SnWO₄/NiO_x film, however, could not be saturated and the ΔOCP is limited to ~ 0.12 V. This behavior is consistent with Fermi level pinning due to the presence of trap states at the α -SnWO₄/NiO_x interface. Therefore, even though NiO_x significantly improves the stability and photocurrent of α -SnWO₄, it may not be the optimal protection layer for this material.

LSV measurements of α -SnWO₄/NiO_x photoelectrodes were also performed without using any hole scavenger (**Figure 54b**). Unfortunately, almost no photocurrent for the oxygen evolution reaction is observed, except for the transients present at potentials more positive than 0.7 V vs. RHE indicating surface recombination processes and/or slow OER kinetics.^[116] This may be caused by the fact that NiO_x has a poor OER activity in pH-neutral electrolytes.^[167-168] The reference NiO_x film deposited on FTO indeed produces an OER current density of only 0.5 mA cm⁻² at a relatively large overpotential of $\eta = 0.53$ mV (see **Figure S 29**). Another possible reason could be the relatively negative potential of the valence band maximum in α -SnWO₄, which limits the available overpotential for the OER to ~ 0.33 V (see chapter 4.2, **Figure 46c**).

The wavelength-dependent incident photon-to-current efficiency (IPCE) of α -SnWO₄/NiO_x films at a potential of 1.23 V vs. RHE with Na₂SO₃ added as hole scavenger is shown in **Figure 55a**. Consistent with the absorption coefficient (see chapter 4.2, **Figure 44a**), the IPCE gradually increases from 3.8% at 605 nm to up to a value of 38% at 355 nm. The maximum IPCE of 38% is more than one order of magnitude higher than values reported in the literature for unprotected α -SnWO₄ films.^[97] Integrating the measured IPCE over the AM1.5 spectrum, a photocurrent density of > 1.8 mA cm⁻² at $E = 1.23$ V vs. RHE under AM1.5 illumination should be generated by the α -SnWO₄/NiO_x photoelectrodes. However, only a value of ~ 0.75 mA cm⁻² is measured (**Figure 51a**). This difference is attributed to the nonlinear dependence of the photocurrent on the light intensity, since the wavelength-dependent IPCE in **Figure 55a** was measured with relatively low light intensities (~ 0.1 to 0.6 mW cm⁻²; see **Figure S 30**) compared to the AM1.5 spectrum (~ 100 mW cm⁻²). As shown in **Figure 55b**, the IPCE indeed decreases with increasing light density which confirms the nonlinear dependence (a linear dependence would translate in a constant IPCE with light intensity) and is most likely a consequence of hole trapping at the α -SnWO₄/NiO_x interface, as discussed above.

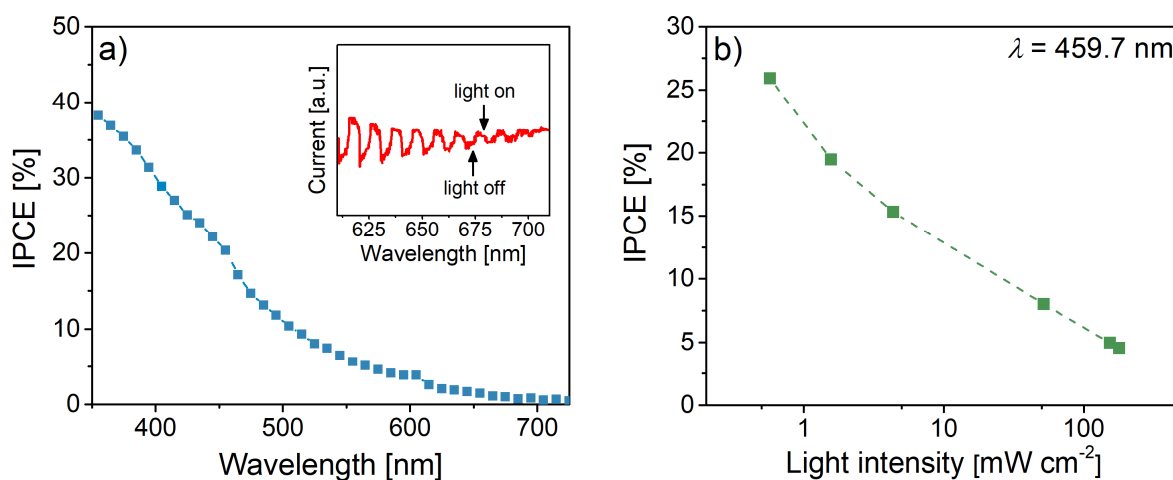


Figure 55. **a)** IPCE as function of wavelength of α -SnWO₄/NiO_x photoelectrode. Inset: IPCE raw data showing the onset wavelength range of the photocurrent. **b)** IPCE as function of incident light intensity at a wavelength of $\lambda = 459.7$ nm. In both measurements, the film was illuminated from the frontside and a constant potential of 1.23 V vs. RHE was applied. The electrolyte was a 0.5 M KPi-buffer solution (pH 7) with 0.5 M Na₂SO₃ added as a hole scavenger.

4.5 Conclusion

In this chapter, pulsed laser deposited α -SnWO₄ films were used to identify important opto-electronic and photoelectrochemical key parameters of the material: absorption coefficient, band positions, carrier mobility, carrier lifetime, carrier diffusion length and PEC stability (see **Table 2**).

The complex pulsed laser deposition process of α -SnWO₄ was elucidated and the optimized phase-pure films were used to confirm both the nearly optimum band positions that straddle the water oxidation and reduction potentials and the nearly ideal bandgap of 1.9 eV of the material.

The charge carrier transport in α -SnWO₄ films was systematically investigated as a function of the PLD process parameters and the conditions of the post-deposition anneal treatment. By a combination of TRTS and TRMC measurements, it was shown that the presence of grain boundaries limits the charge carrier transport in this material. After increasing the domain/grain size via a high-temperature treatment, the carrier mobility measured with TRMC was found to be enhanced by two orders of magnitude up to a value of 0.35 cm² V⁻¹s⁻¹. With an effective carrier lifetime of ~44 ns, this translates into an effective carrier diffusion length of ~200 nm. Although this diffusion length is one of the highest ever measured for a metal oxide photoelectrode candidate, it is still much smaller than the thickness of ~10 μ m needed to generate an AM1.5 photocurrent of 15 mA cm⁻². Therefore, strategies to overcome this mismatch such as doping, hydrogen treatment, the growth of epitaxial films, and nanostructuring have to be explored. Furthermore, the influence of the Sn_{0.23}WO₃ impurity phase, the slight W-enrichment and possible amounts of Sn⁴⁺ on the charge carrier transport should be investigated, which might lead to further improvement of the charge carrier transport. It should be noted that the combination of TRTS and TRMC measurements offer a powerful tool for the identification of charge carrier transport limitations arising from grain boundaries in thin film photoabsorbers.

Another limitation of α -SnWO₄ was found to be its poor (photo)electrochemical stability. When exposed to water and illumination, the Sn²⁺ at the surface is oxidized resulting in a thin SnO₂ layer. Even though this oxidation appears to be self-limited, its thickness is sufficient to prevent the photogenerated holes from reaching the electrolyte and therefore suppressing the photocurrent. By depositing a NiO_x protection layer, the sulfite oxidation photocurrent was increased by more than two orders of magnitude and a record AM1.5 photocurrent of ~0.75 mA cm⁻² at 1.23 V vs. RHE was obtained.

Oxygen evolution at α -SnWO₄/NiO_x photoelectrodes, however, remains challenging due to the combination of sluggish OER kinetics of NiO_x in a neutral electrolyte and a relatively negative valence band maximum of α -SnWO₄. In addition, the possible presence of trap states at the α -SnWO₄/NiO_x interface limits the photocurrent to several $\mu\text{A cm}^{-2}$ for potentials < 0.8 V vs. RHE. Future efforts should therefore be directed towards exploring different OER catalysts, protection layers (e.g., “leaky” TiO₂), and interfacial layers to further improve the photoconversion efficiency of α -SnWO₄.

If the proposed strategies are successfully implemented, a combination of α -SnWO₄ with a suitable bottom absorber (e.g., Si) can potentially result in a solar water splitting device with an efficiency higher than 20%.

Table 2. Summary of key PEC parameters of α -SnWO₄

Parameter	Value
Band gap energy, E_g	1.90 \pm 0.05 eV (indirect), 2.60 \pm 0.05 (direct)
Absorption coefficient at 500 nm, α	$1.9 \times 10^4 \text{ cm}^{-1}$
Thickness for $j_{\text{AM1.5}} = 10 / 15 \text{ mA cm}^{-2}$, t	2 / 10 μm
Carrier mobility, $\sigma \Sigma \mu$	$\sim 0.35 \text{ cm}^2 \text{ V}^{-1} \text{ s}^{-1}$
Carrier lifetime, $\tau_{50\%}$	$\sim 44 \text{ ns}$
Carrier diffusion length, L_D	$\sim 200 \text{ nm}$
Work function, Φ	-0.04 V vs. NHE
Valence band maximum, V_{BM}	1.46–1.66 V vs. NHE
PEC stability	Passivation by photo-induced formation of SnO ₂

Summary

Global warming is a major threat to humanity and ecosystems on our planet. If it cannot be limited to $\sim 1.5^\circ\text{C}$, the consequences will be disastrous (e.g., extreme weather events, famines, political instability). The major driving force of climate change is the combustion of fossil fuels for energy production releasing the greenhouse gas CO_2 . Therefore, a transition to a sustainable energy system based on renewable energies is an essential step to stop climate change. Among the renewable energy sources, solar energy is by far the most abundant source and is therefore indispensable to meet the steadily growing world energy demand in any fossil-fuel free energy scenario.

The potential to store solar energy in the form of chemical bonds within the so-called *solar fuels* has attracted attention because it solves the problem of the intermittent nature of solar power. Here, one possible pathway is the production of hydrogen via photoelectrochemical water splitting. The key element in this approach is a semiconducting photoelectrode immersed in an aqueous solution that converts sunlight into electrons and holes which then split water into hydrogen and oxygen, respectively. This renewable hydrogen can be used as a fuel by itself or can serve as a feedstock element for large scale industrial chemical processes to produce other valuable chemicals (e.g., Fischer-Tropsch and Haber-Bosch for the production of hydrocarbons and ammonia, respectively). However, the photoelectrode material that meets all the stringent requirements such as a suitable bandgap, an efficient charge carrier transport, low-cost and stability on the time scale of years is still elusive.

Semiconducting metal oxides are a promising class of photoelectrode materials since they are in general cheaper and more stable in aqueous solution than conventional Si-based and III-V semiconductors. Among this group, BiVO_4 is an outstanding example for the development of an efficient metal oxide photoelectrode. However, the rather poor charge carrier transport as well as the bandgap of 2.4 eV that translates into a maximum solar-to-hydrogen (STH) efficiency of 9% preclude practical applications. Therefore, pulsed laser deposition (PLD)—a powerful tool for the preparation of dense metal oxide films of high electronic quality—was used in this thesis to deposit compact and efficient BiVO_4 and $\alpha\text{-SnWO}_4$ photoelectrodes and to study their fundamental opto-electronic and PEC properties.

In Chapter 3, the complex pulsed laser deposition process of efficient BiVO_4 photoelectrodes by ablating a BiVO_4 target was elucidated with a special focus on the deviations from an ideal stoichiometric-target-to-substrate transfer. Several effects were shown to influence the V:Bi ratio of the deposited film: (i) a preferential ablation of Bi when the laser fluence is too low, (ii) a preferential thermalization of V when an oxygen background pressure is added and (iii) re-sputtering/re-evaporation of Bi from the substrate at elevated substrate temperatures. Based on these results, compact and stoichiometric BiVO_4 photoelectrodes with a good electronic quality ($L_D = 95\text{ nm}$) were prepared that generated relatively high and reproducible sulfite oxidation AM1.5 photocurrent densities of $2.4 \pm 0.2\text{ mA cm}^{-2}$ ($E = 1.23\text{ V vs. RHE}$, backside illumination). Future efforts in Mo/W doping

or H₂-treatment of the films are likely to lead to further performance enhancements. Moreover, the importance of tailoring the PLD process parameters was demonstrated: a small fluence difference of only 0.5 J cm⁻² results in sub-stoichiometric films with three times shorter carrier diffusion lengths and thus significantly lower photoactivities.

In addition, an alternative preparation route for efficient BiVO₄ photoelectrodes by the alternating ablation of Bi₂O₃ and V₂O₅ targets was presented for the first time. This approach lays the foundation for growing different orientated epitaxial films, since the deposition parameters can be tailored without restrictions related to a non-stoichiometric target-to-substrate transfer. These films would be of great value to investigate the anisotropic charge carrier transport in BiVO₄ photoanodes in detail.

Chapter 4 discussed the promising α -SnWO₄, a metal oxide that attracted attention in the field as a potential photoelectrode material due to its nearly optimum bandgap and its early photocurrent onset potential. However, at the beginning of this thesis research, the photoelectrochemical performance was very poor and little was known on the important PEC parameters, such as the carrier mobility, lifetime, and diffusion length. Therefore, one major objective of this thesis was to elucidate important PEC parameters and study the limitations of this material in detail.

After optimizing the PLD process and post-treatment parameters, phase-pure α -SnWO₄ films were obtained that were initially used to confirm the nearly ideal bandgap (~1.9 eV) and band alignment ($V_{BM} = 1.46$ – 1.66 V vs. NHE) as reported in the literature.

The charge carrier mobility measured by time-resolved microwave conductivity (TRMC) was found to be enhanced by more than two orders of magnitude by a high-temperature treatment. As a result, an effective carrier diffusion length of ~200 nm was achieved in α -SnWO₄ films—one of the highest ever measured for a metal oxide photoelectrode candidate. To understand the reason for this improvement, a complimentary analysis by time-resolved terahertz spectroscopy (TRTS) was performed. It was found that the increase of the mobility is due to larger grain/domain sizes of the heat-treated films. In other words, grain boundaries limit the charge carrier transport in α -SnWO₄ films. The combination of TRMC and TRTS used in this thesis offers a powerful and generally applicable tool to identify grain-boundary limited charge carrier transport in thin film photoabsorbers.

Photoelectrochemical characterization of bare α -SnWO₄ films revealed a similar behavior as reported in literature. As soon as a potential is applied, the photocurrents drops to several $\mu\text{A cm}^{-2}$ after a short initial spike. X-ray photoelectron spectroscopy (XPS) analysis of the surface after PEC measurements revealed the formation of a thin SnO₂ layer (~6 nm). This layer is believed to act as a hole blocking layer due to the much more positive valence band edge of SnO₂ as compared to α -SnWO₄ and pushes the photocurrent to nearly zero. However, no further film degradation and morphology change was observed suggesting that this SnO₂ film protects the surface from water exposure and further oxidation. To solve this

surface stability issue, a hole-conducting NiO_x protection layer was pulsed laser deposited onto the α-SnWO₄ films which drastically improved the stability and the photocurrent, setting a new benchmark for the AM1.5 photocurrent (0.75 mA cm⁻² at $E = 1.23$ V) and the IPCE values (38% at $\lambda = 355$ nm) with Na₂SO₃ added as a hole scavenger.

The comprehensive evaluation of α-SnWO₄ in this thesis allows to propose several strategies to further improve its performance. Even though the effective carrier diffusion length was found to be relatively high, it is still much lower than the film thickness needed to generate an AM1.5 photocurrent of 15 mA cm⁻². Here, well established strategies such as doping, hydrogen treatment and nanostructuring may be used to overcome this mismatch and should be explored for α-SnWO₄. In addition, overcoming the presence of trap states at the α-SnWO₄/NiO_x interface and demonstrating the still challenging oxygen evolution reaction (OER) should be attempted, for example by depositing different co-catalysts that also act as a protection layer.

If these proposed strategies can be successfully implemented, a combination of α-SnWO₄ with a silicon solar cell as a bottom absorber can potentially result in a solar water spitting device with a STH efficiency higher than 20%.

Appendix

a) Supplemental information

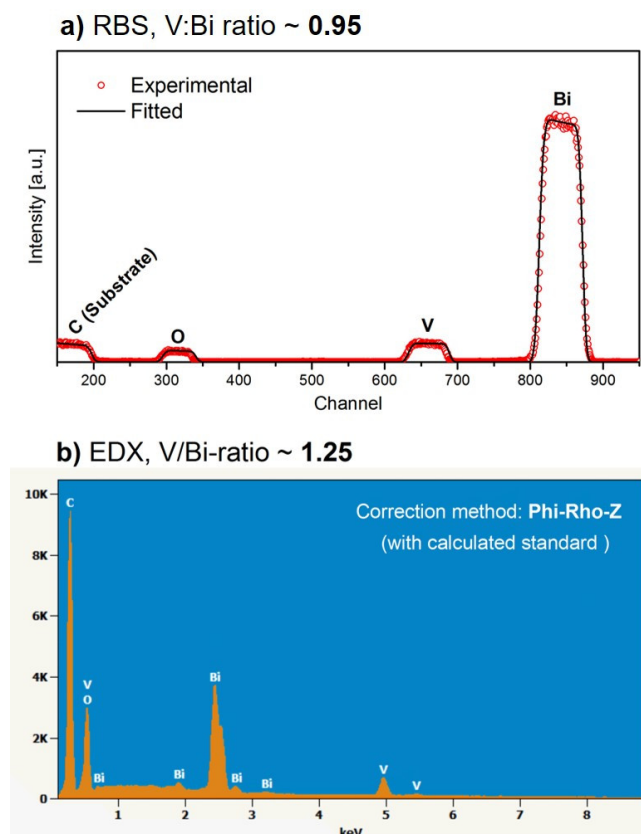


Figure S 1. a) RBS analysis of a $\text{Bi}_x\text{V}_y\text{O}_z$ film (~150 nm) deposited on glassy carbon prepared by the alternating ablation of V_2O_5 and Bi_2O_3 targets b) EDX analysis of the same film ($U_{acc} = 10$ kV). The quantitative elemental analysis was performed with the Phi-Rho-Z method.

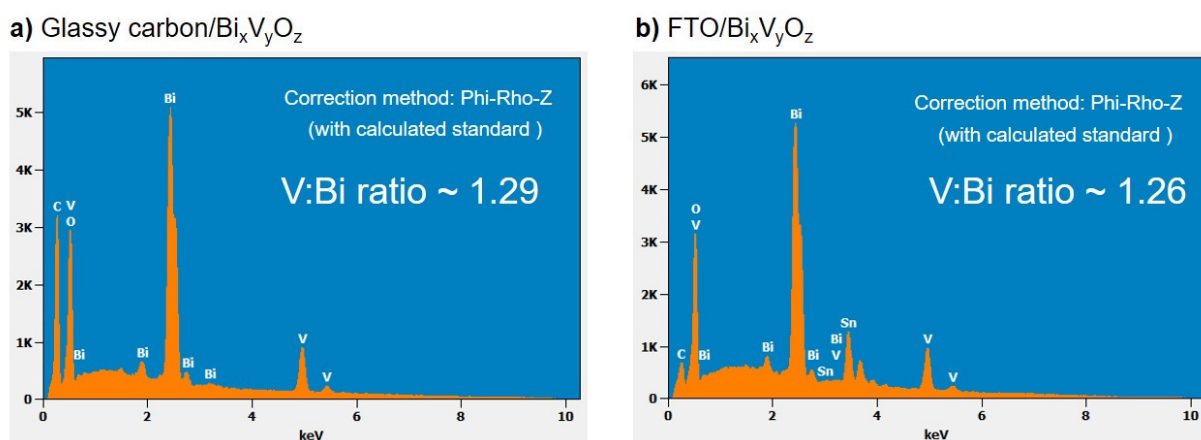


Figure S 2. EDX analysis of identical $\text{Bi}_x\text{V}_y\text{O}_z$ films deposited on a) glassy carbon and b) FTO by the ablation of a BiVO_4 target. The quantitative elemental analysis was performed with the Phi-Rho-Z method.

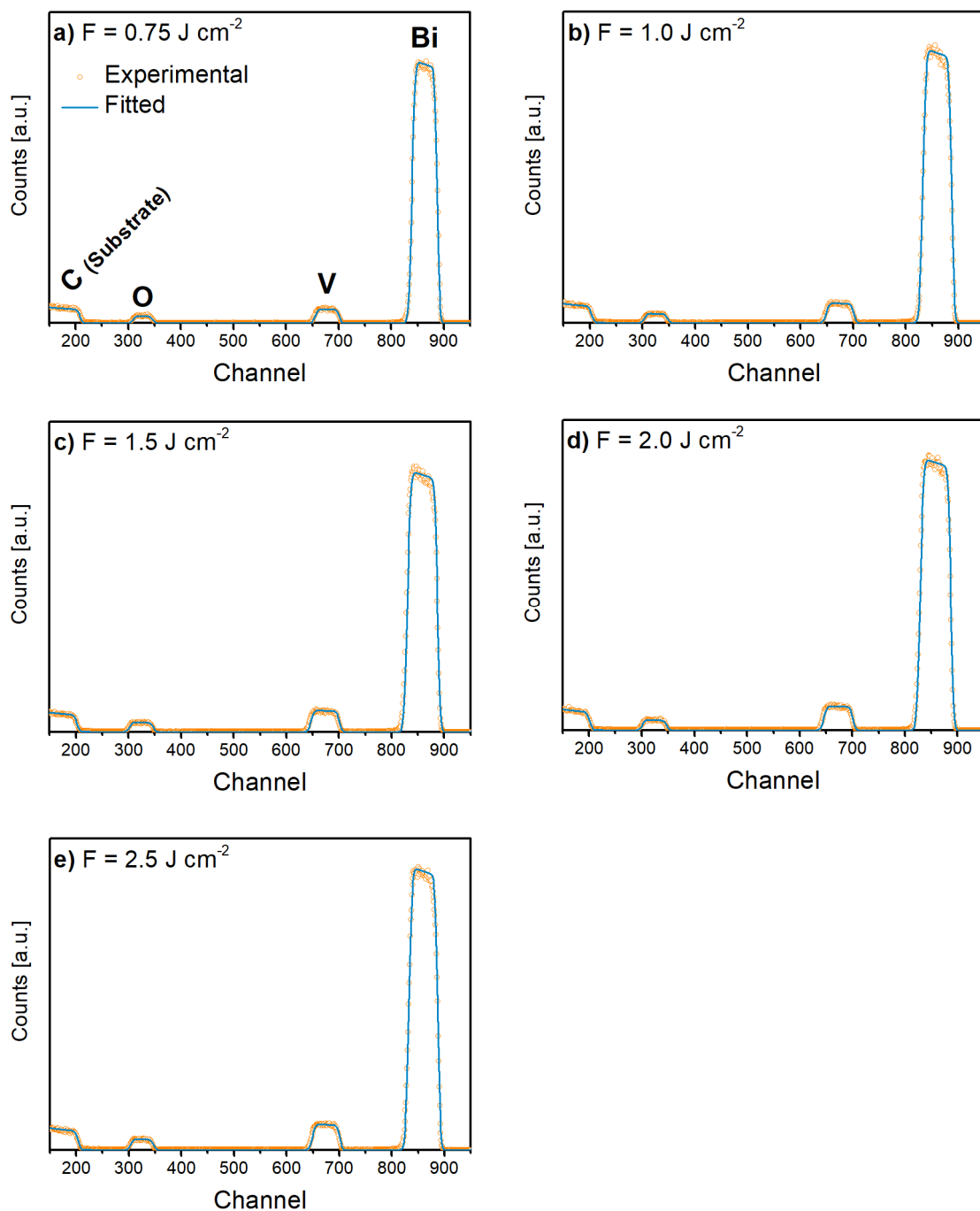


Figure S 3. RBS analysis of films deposited by ablating a BiVO_4 target with different laser fluences on glassy carbon at RT in vacuum.

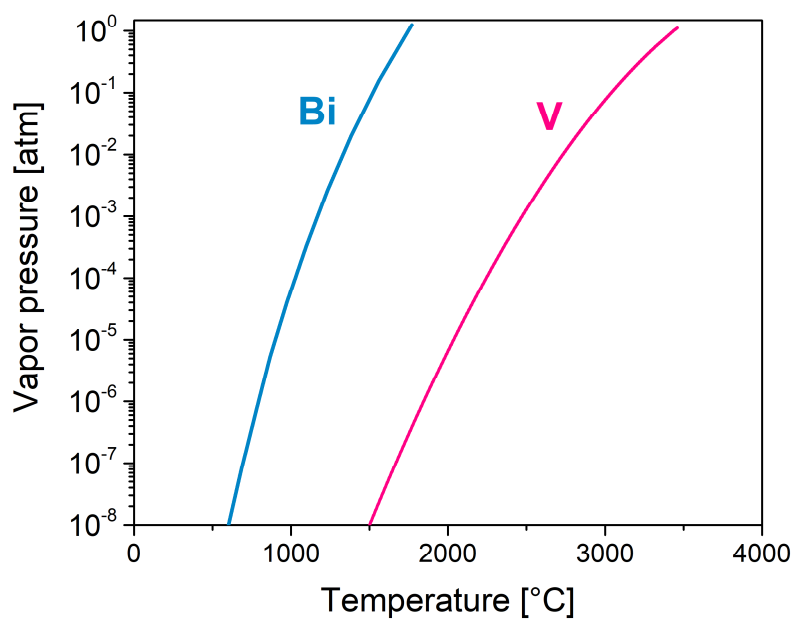


Figure S 4. Vapor pressures of Bi and V as a function of temperature (Adapted from Honig, R.E., "Vapor pressure data for the more common elements" RCA Review, 1957, 18, 195-204).

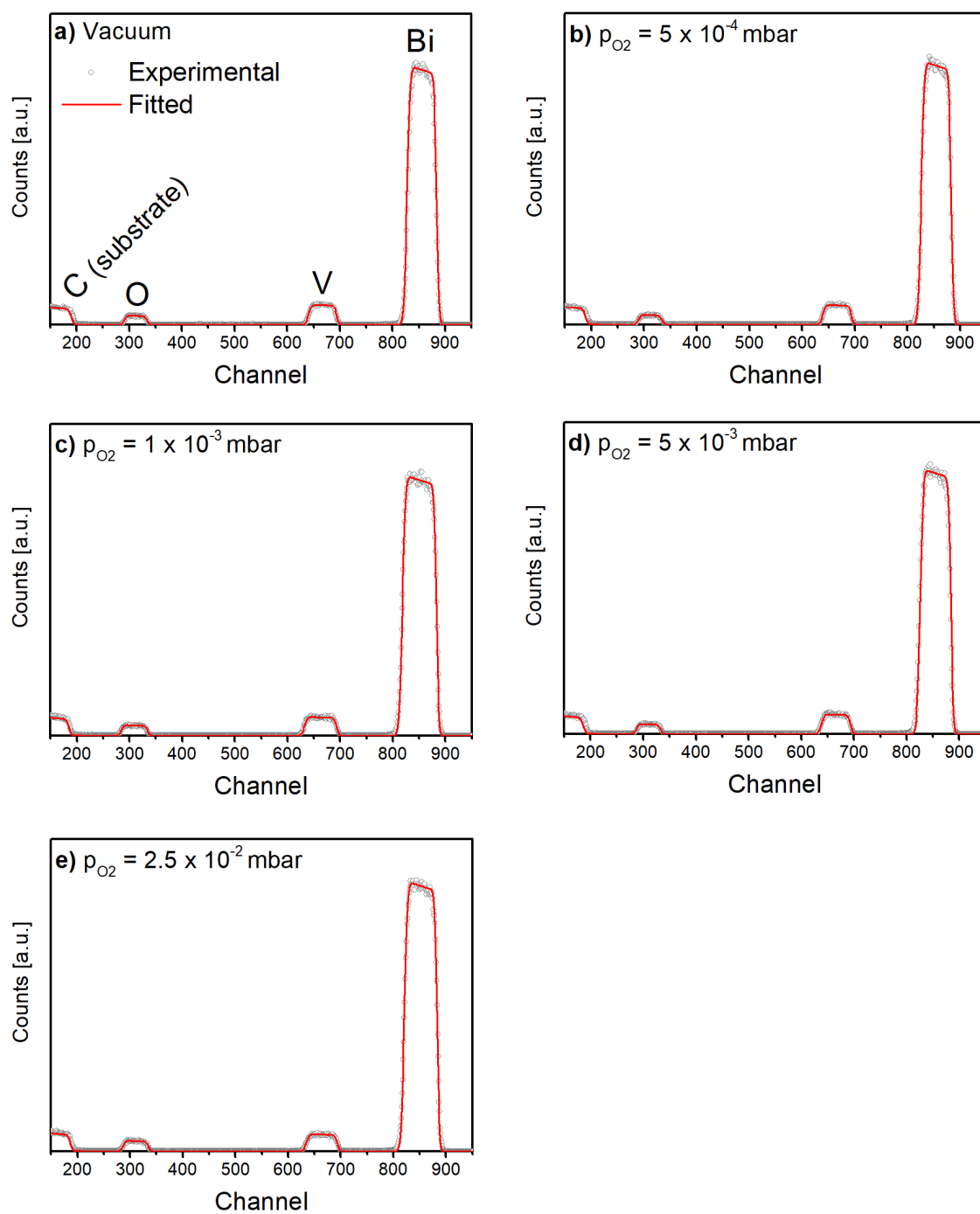


Figure S 5. RBS analysis of films deposited by ablating a BiVO_4 target in different oxygen background pressures on glassy carbon substrates at RT. The fluence was 1.5 J cm^{-2} .

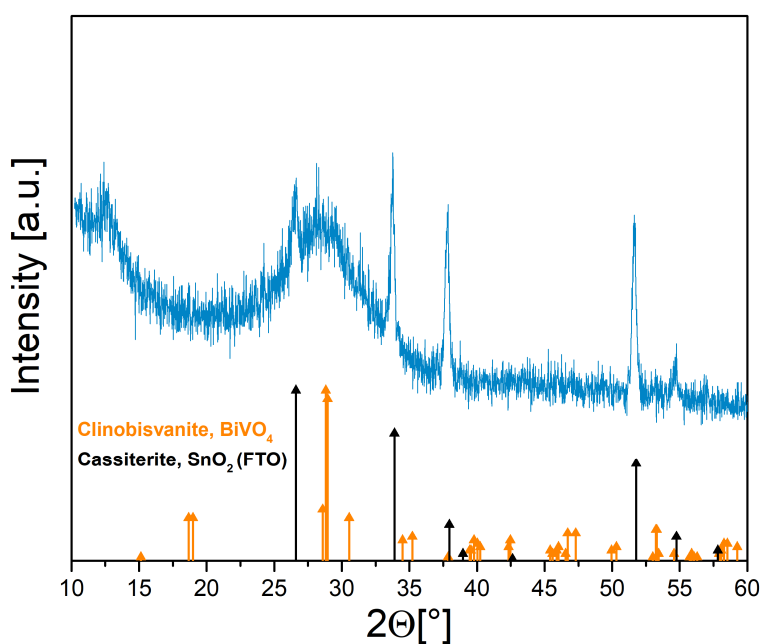


Figure S 6. X-ray diffractogram of an as-deposited BiVO₄ on FTO ($F=1.5 \text{ J cm}^{-2}$, vacuum, RT) only showing the reflections of the underlying substrate (cassiterite, SnO₂, PDF no. 00-041-1445). Orange lines represent the reference pattern of monoclinic BiVO₄ (PDF no. 00-014-0688).

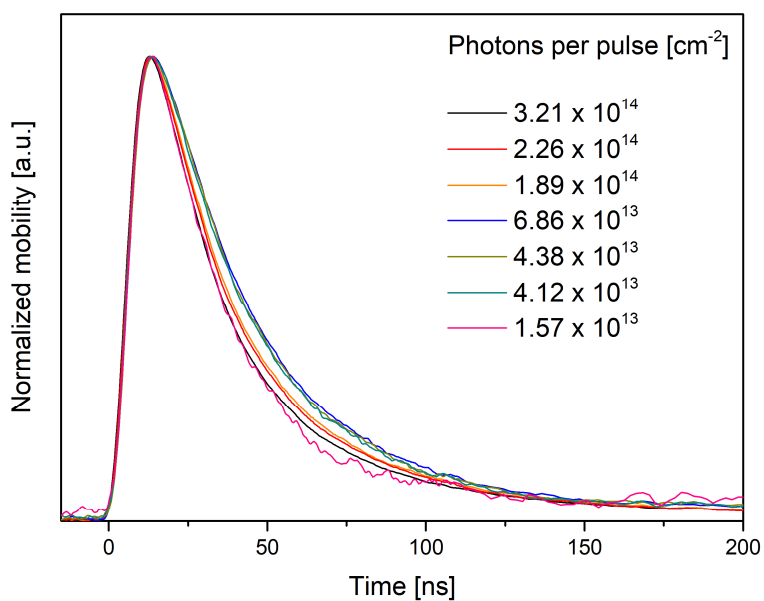


Figure S 7. Normalized TRMC signals of a BiVO₄ film deposited on quartz (BiVO₄-target, $F = 1.5 \text{ J cm}^{-2}$, vacuum, RT, annealed in air at 450°C for 2 h) at different light intensities.

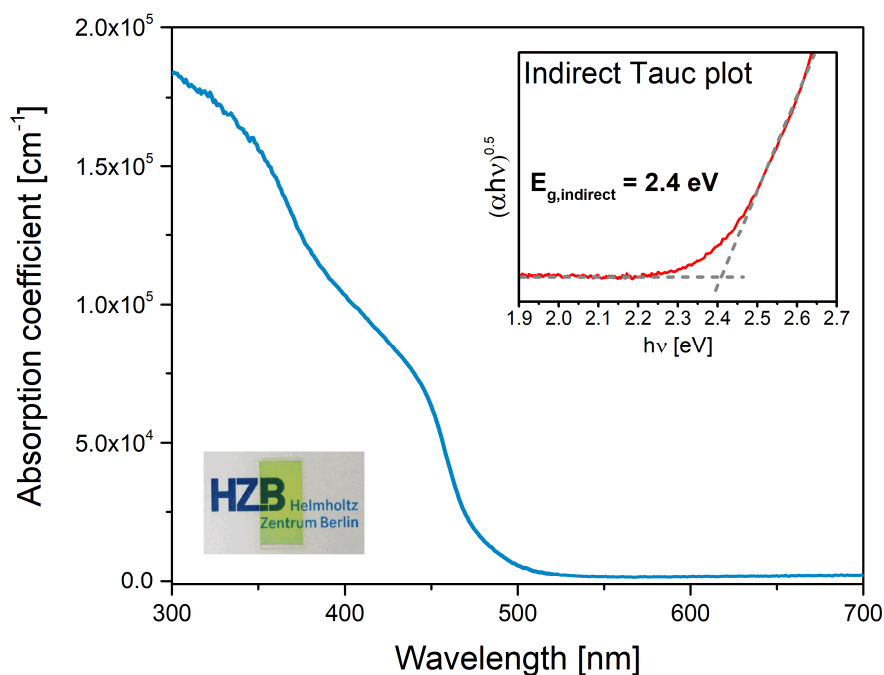


Figure S 8. Absorption coefficient (α) of a pulsed laser deposited BiVO_4 film on quartz (BiVO_4 -target, vacuum, RT, $F = 1.5 \text{ J cm}^{-2}$, annealed in air at $450 \text{ }^\circ\text{C}$ for 2h) measured with UV-VIS spectroscopy. Inset: Indirect Tauc plot & optical photograph.

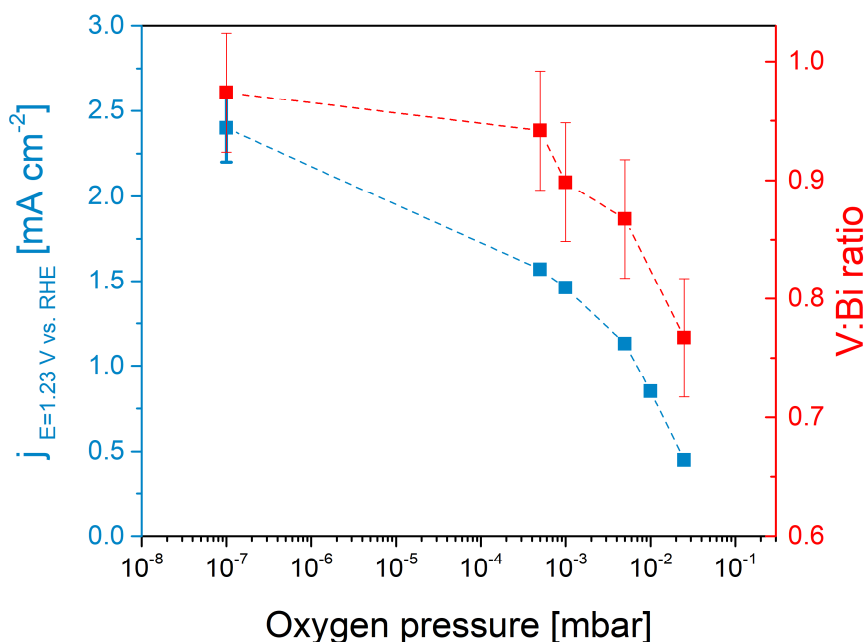


Figure S 9. Left y-axis: Photocurrent of BiVO_4 films ($\sim 90 \text{ nm}$) at a potential of 1.23 V vs. RHE under backside AM1.5 illumination as a function of the oxygen background pressure used during the deposition (BiVO_4 -target, RT, $F = 1.5 \text{ J cm}^{-2}$, annealed in air at $450 \text{ }^\circ\text{C}$ for 2h) The electrolyte was a 0.5 M KPi -buffer ($\text{pH} \sim 7$) with $0.5 \text{ M Na}_2\text{SO}_3$. Right y-axis: V:Bi ratio of reference films deposited on glassy carbon determined with RBS.

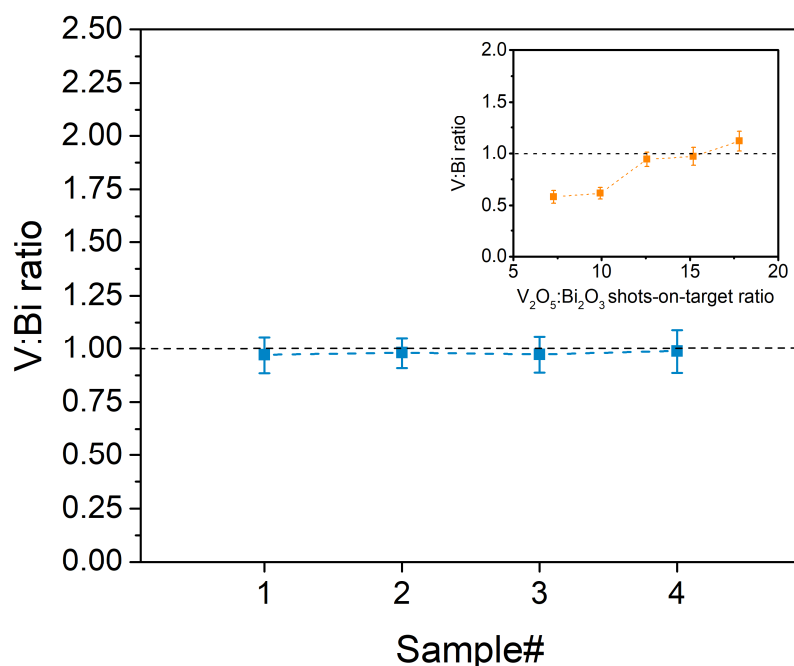


Figure S 10. V:Bi ratio determined with RBS corrected EDX measurements of identically prepared BiVO₄ films prepared by the alternating ablation of V₂O₅ and Bi₂O₃ targets ($F = 1.5 \text{ J cm}^{-2}$, $p_{O_2} = 5 \times 10^{-2} \text{ mbar}$, $T_{sub} = 400^\circ\text{C}$, V₂O₅:Bi₂O₃ shots-on-target ratio = 15). Inset: V:Bi-ratio determined with EDX corrected RBS measurements as a function of the V₂O₅:Bi₂O₃ shots-on-target ratio. The shots on the Bi₂O₃-target were set to 25 and the shots on the V₂O₅-target were varied.

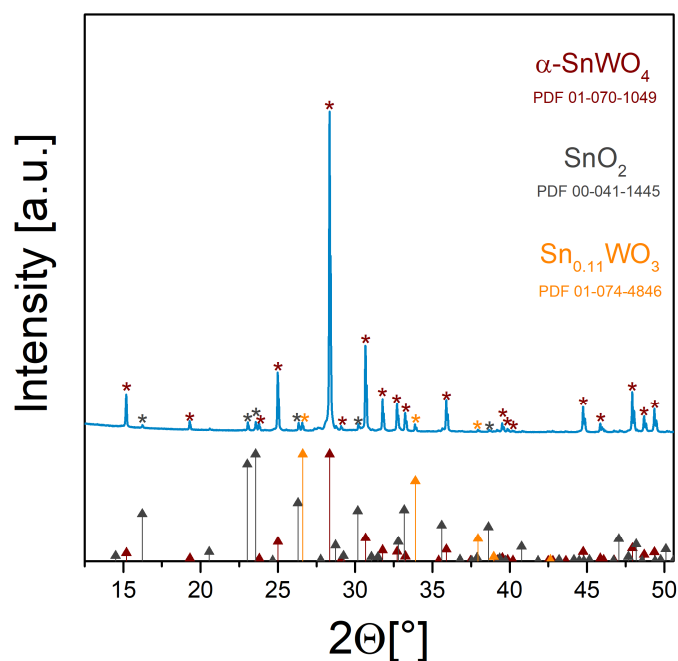


Figure S 11. X-ray diffractogram of the $\alpha\text{-SnWO}_4$ target measured in Bragg-Brentano geometry. Brown lines and asterisks (*) represent the reference pattern of $\alpha\text{-SnWO}_4$ (PDF no. 00-027-0902). Grey and orange lines and asterisks represent the additional reflexes from impurity phases SnO₂ (PDF no. 00-041-01445) and Sn_{0.11}WO₃ (PDF no. 01-074-4846).

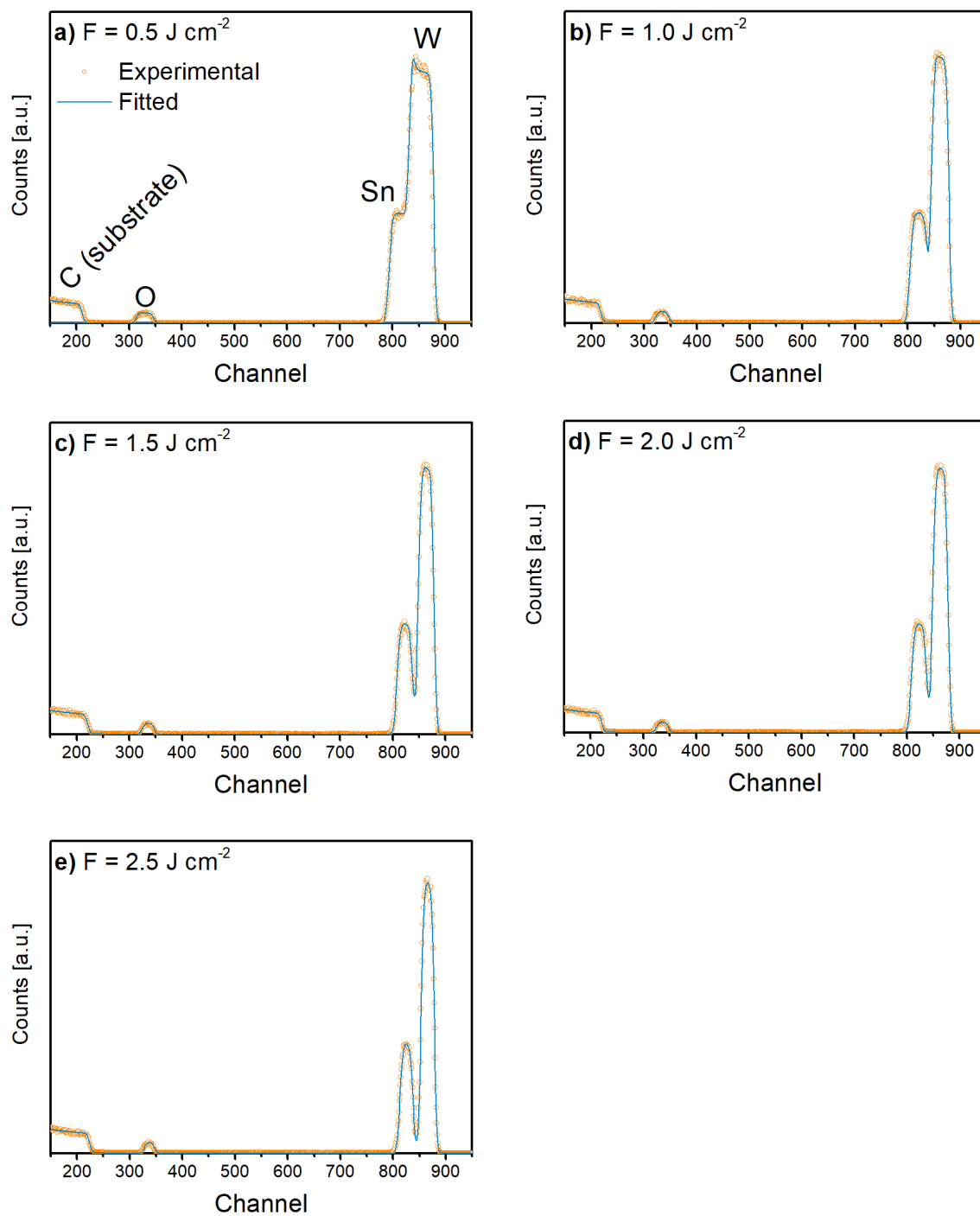


Figure S 12. Rutherford backscattering spectrometry analysis of films deposited on glassy carbon by ablating a α - SnWO_4 target with different laser fluences in vacuum at RT. The target-to-substrate distance was 60 mm in all depositions.

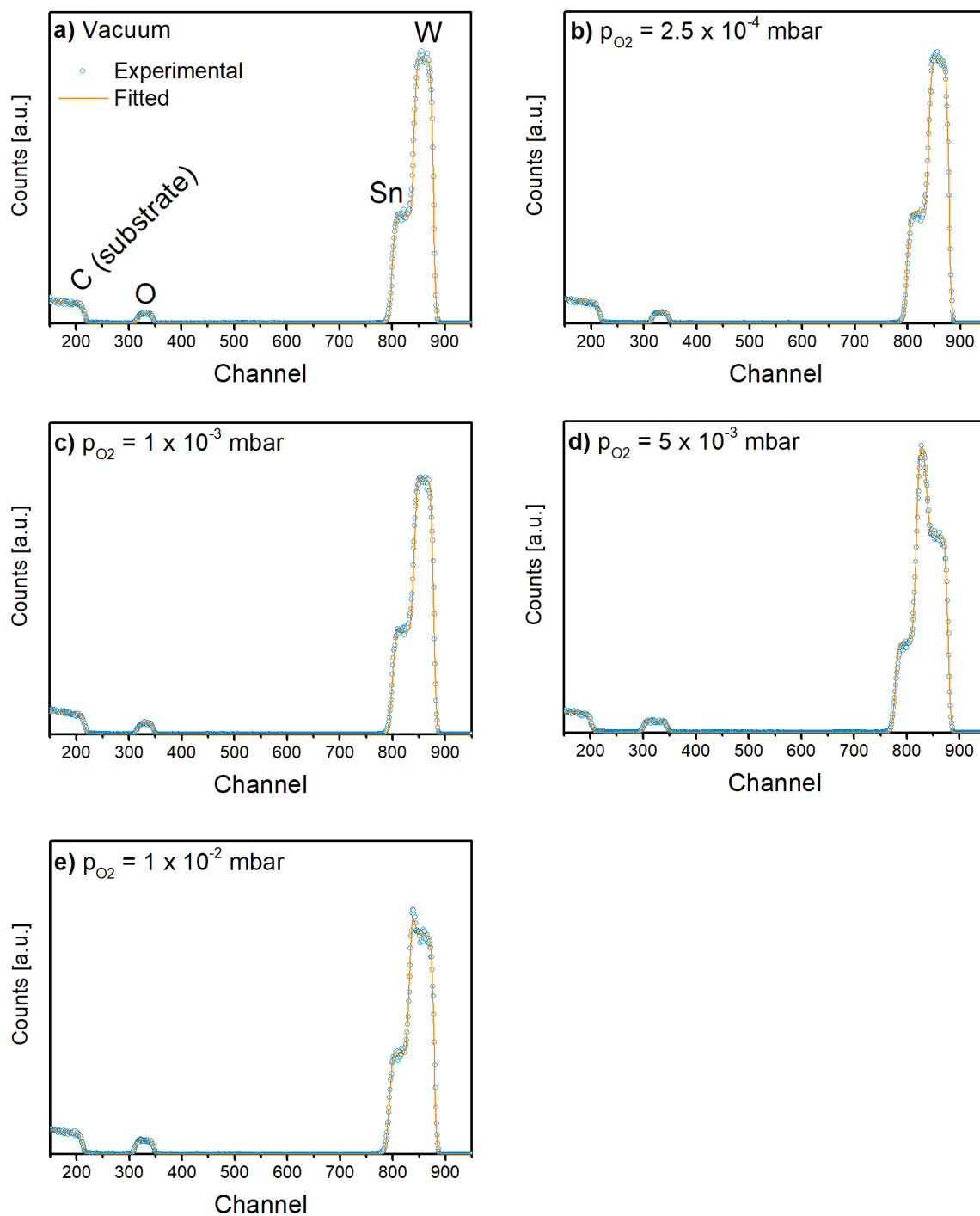


Figure S 13. Rutherford backscattering spectrometry analysis of films deposited on glassy carbon by ablating a α - SnWO_4 target in different oxygen background pressures at RT. The target-to-substrate distance was 60 mm and the fluence was 2 J cm^{-2} in all depositions.

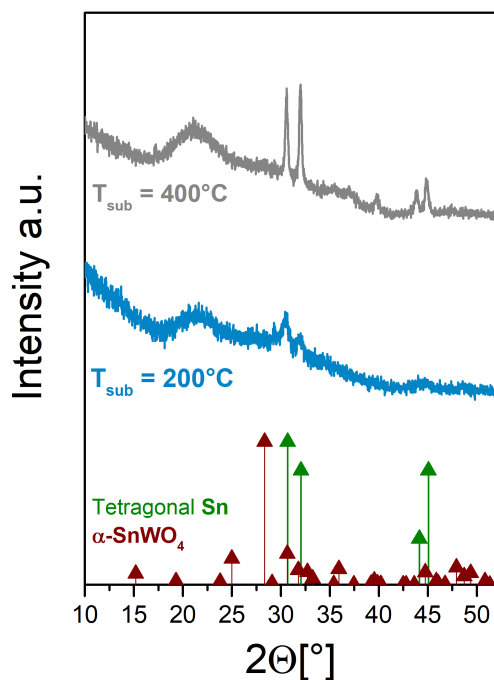


Figure S 14. X-ray diffractograms of films deposited on quartz substrates by ablating a $\alpha\text{-SnWO}_4$ target with an oxygen pressure of 1×10^{-3} mbar and a substrate temperature of 200°C and 400°C , respectively. The fluence was 2 J cm^{-2} and the target-to-substrate distance was 60 mm.

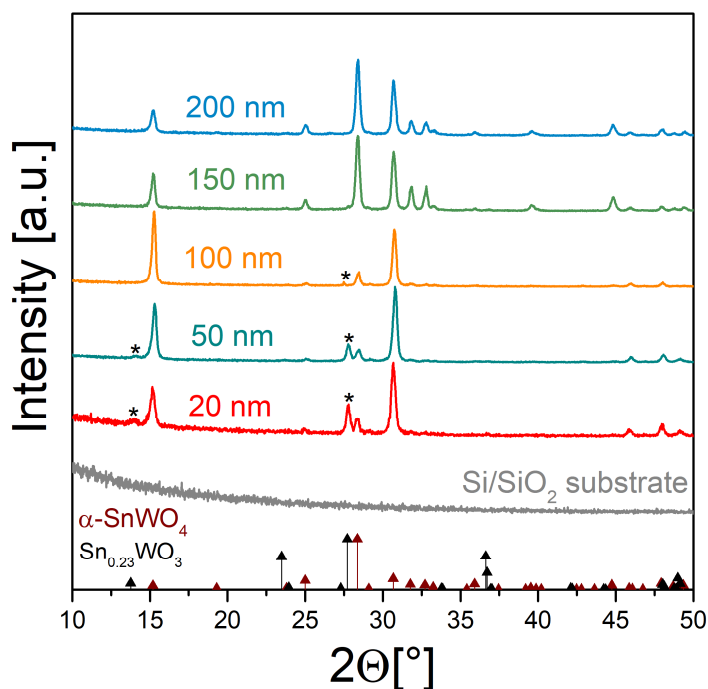


Figure S 15. X-ray diffractograms of $\alpha\text{-SnWO}_4$ films deposited on Si/SiO_2 ($F = 2 \text{ J cm}^{-2}$, $p_{\text{O}_2} = 2.5 \times 10^{-4}$ mbar) with different thicknesses and annealed at 600°C for 2 h in Ar. Brown and black lines represent the reference pattern of $\alpha\text{-SnWO}_4$ (PDF 01-070-1059) and $\text{Sn}_{0.23}\text{WO}_3$ (IOCD 81326), respectively. Reflections of the $\text{Sn}_{0.23}\text{WO}_3$ phase are additionally marked with a black asterisks (*).

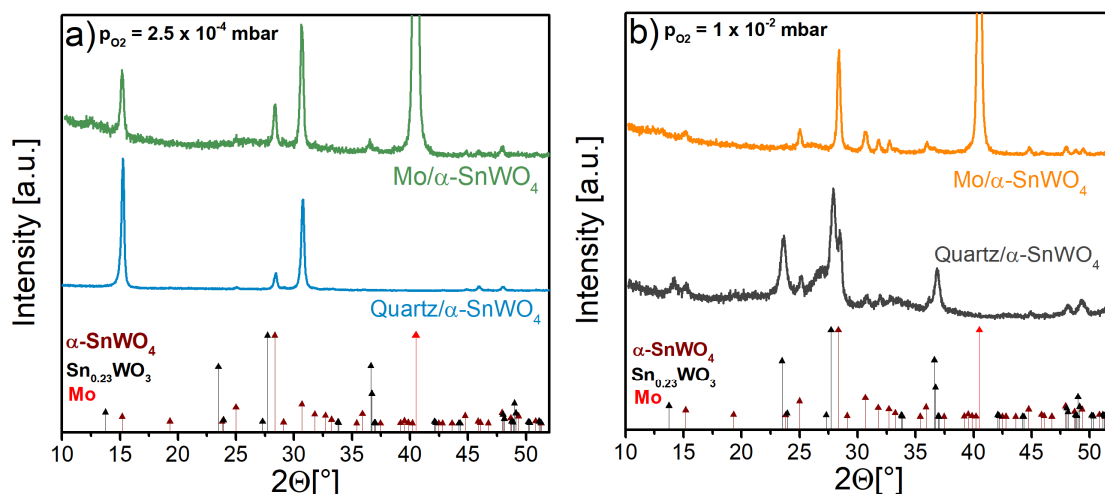


Figure S 16. X-ray diffractograms of α -SnWO₄ films prepared under the same deposition conditions, but on two different substrates: quartz and molybdenum. The oxygen background pressure was 2.5×10^{-4} mbar in **a)** and 1×10^{-2} mbar in **b)**. All films were annealed at 600°C in Ar for 2h. The fluence was 2 J cm^{-2} and the target-to-substrate distance was 60 mm. Brown, black and red lines represent the reference pattern of α -SnWO₄ (PDF 01-070-1059), Sn_{0.23}WO₃ (IOCD 81326) and Mo (PDF 00-042-1120), respectively.

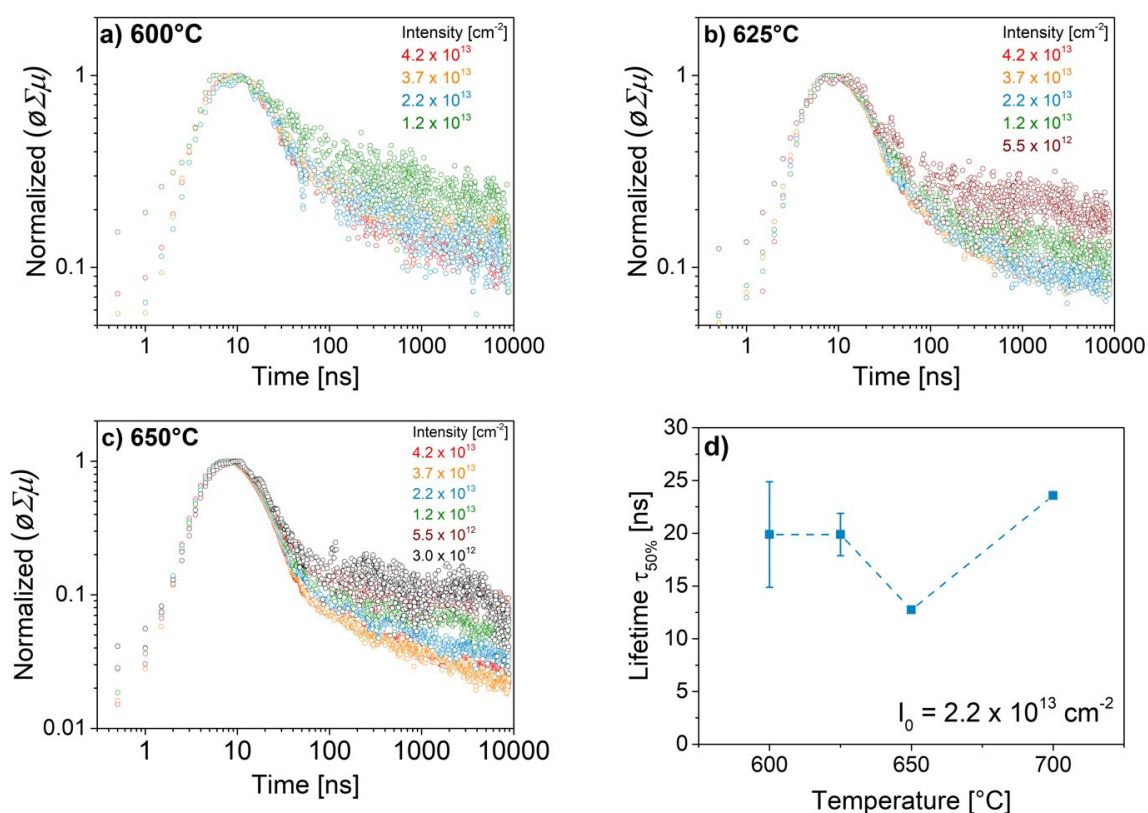


Figure S 17. Normalized TRMC signal of α -SnWO₄ films deposited on quartz ($F = 2 \text{ J cm}^{-2}$, $p_{O_2} = 2.5 \times 10^{-4}$ mbar) annealed at **a)** 600°C, **b)** 625°C and **c)** 650°C at different laser intensities. The wavelength of the excitator laser was 355 nm. **d)** Effective charge carrier lifetime ($\tau_{50\%}$) as a function of annealing temperature at a laser intensity of $2.2 \times 10^{13} \text{ cm}^{-2}$.

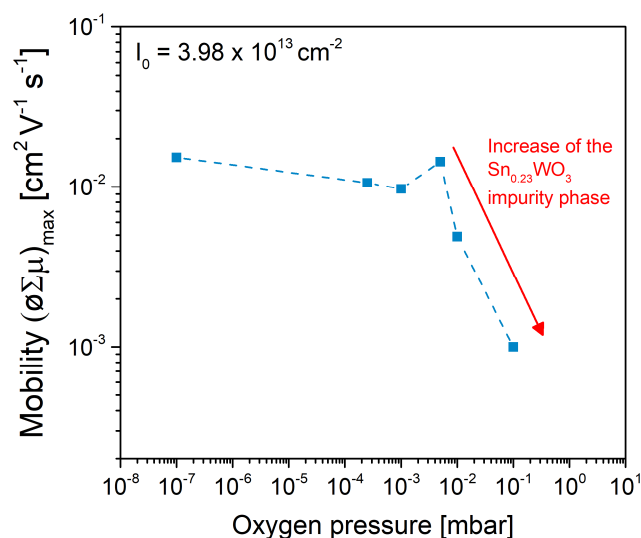


Figure S 18. Peak mobility measured with TRMC for films deposited on quartz ($F = 2 \text{ J cm}^{-2}$, annealed at 600°C in Ar for 2 h) as a function of oxygen pressure used during the deposition. The respective X-ray diffractograms of the films are shown in **Figure 41**. It is noted that no change in the dielectric constant of $\alpha\text{-SnWO}_4$ (62.3) was assumed for the analysis for all films.

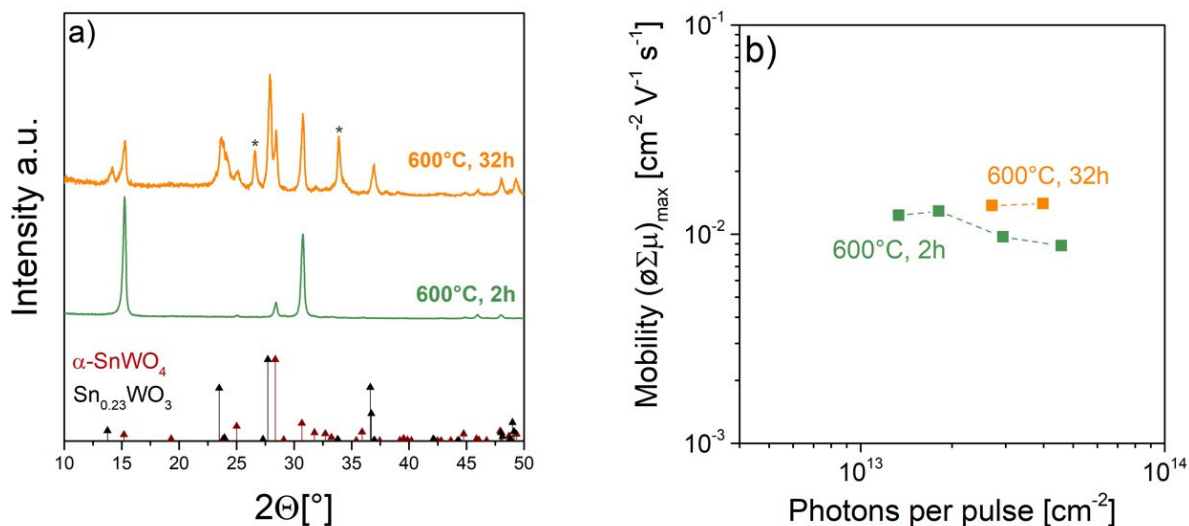


Figure S 19. a) X-ray diffractograms of films annealed at 600°C for different times in Ar. Brown and black lines represent the reference pattern of $\alpha\text{-SnWO}_4$ (PDF 01-070-1059) and $\text{Sn}_{0.23}\text{WO}_3$ (IOCD 81326), respectively. Reflections that cannot be assigned to both phases are marked with grey asterisks (*). **b)** TRMC-obtained peak mobility as a function of photons per pulse of the respective films. The dielectric constant of $\alpha\text{-SnWO}_4$ (62.3) was used for the analysis for both films.

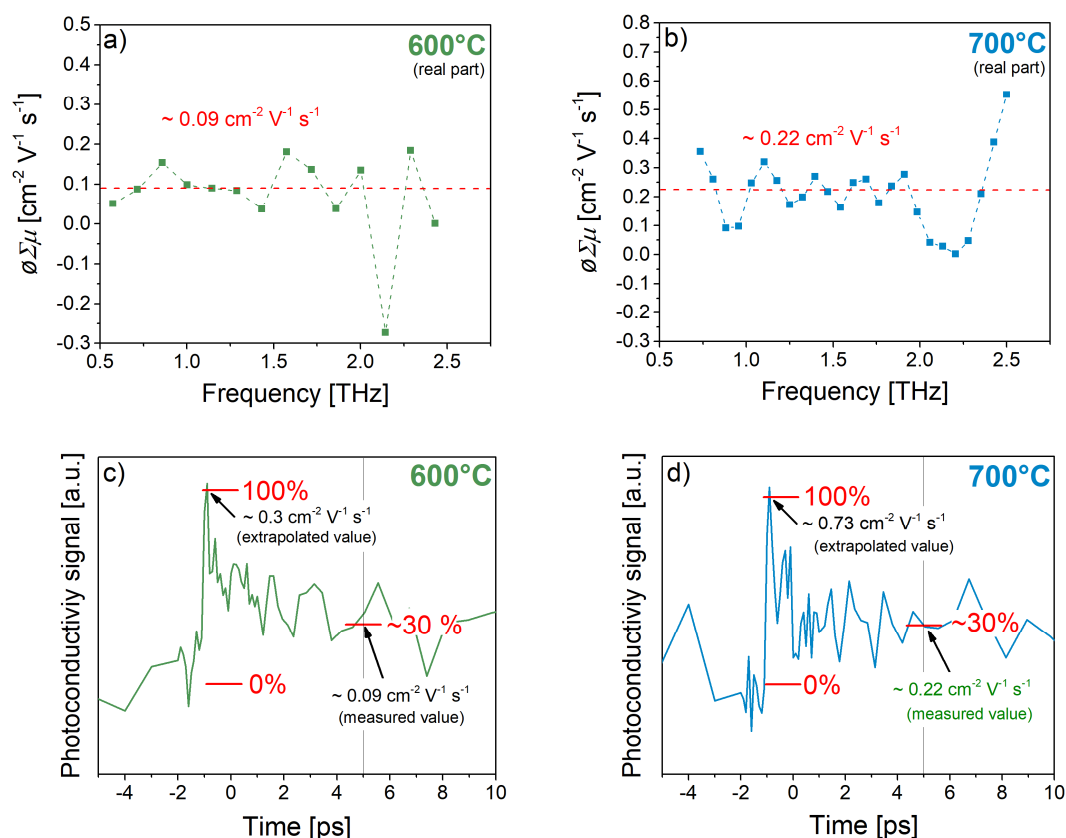


Figure S20. TRTS-obtained mobility spectra (real part) measured at a delay time of 5 ps of films deposited on quartz ($F = 2.0 \text{ J cm}^{-2}$, $p_{\text{O}_2} = 2.5 \times 10^{-4} \text{ mbar}$) and annealed at **a)** 600°C and **b)** at 700°C revealing combined electron-hole mobilities of ~ 0.09 and $\sim 0.22 \text{ cm}^2 \text{V}^{-1} \text{s}^{-1}$, respectively. **c)** and **d)** Photoconductivity transients of the respective films. The peak mobilities were extrapolated using the measured mobilities at a delay time of 5 ps and assuming a decay of the signal to $\sim 30\%$ of its starting value.

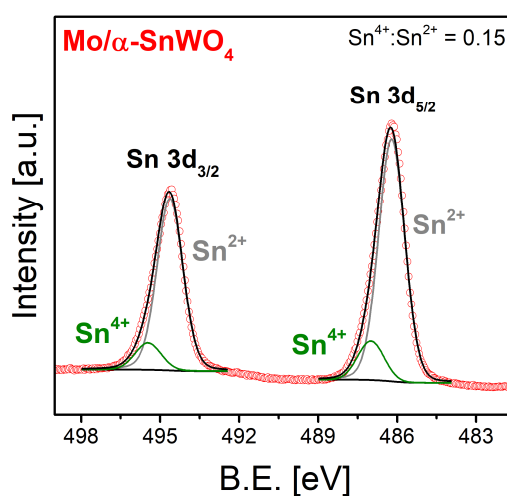


Figure S21. XPS analysis of the Sn 3d region of $\alpha\text{-SnWO}_4$ film deposited on a molybdenum substrate ($F = 2 \text{ J cm}^{-2}$, $p_{\text{O}_2} = 2.5 \times 10^{-4} \text{ mbar}$) annealed at 600°C in Ar for 2 h.

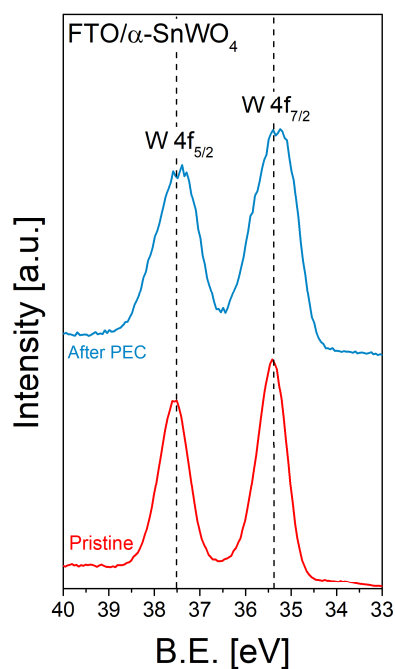


Figure S 22. XPS spectra of the W 4f region of α -SnWO₄ deposited on FTO ($F = 2 \text{ J cm}^{-2}$, $p_{\text{O}_2} = 2.5 \times 10^{-4} \text{ mbar}$, annealed at 600°C in Ar for 2 h) before and after PEC measurements.

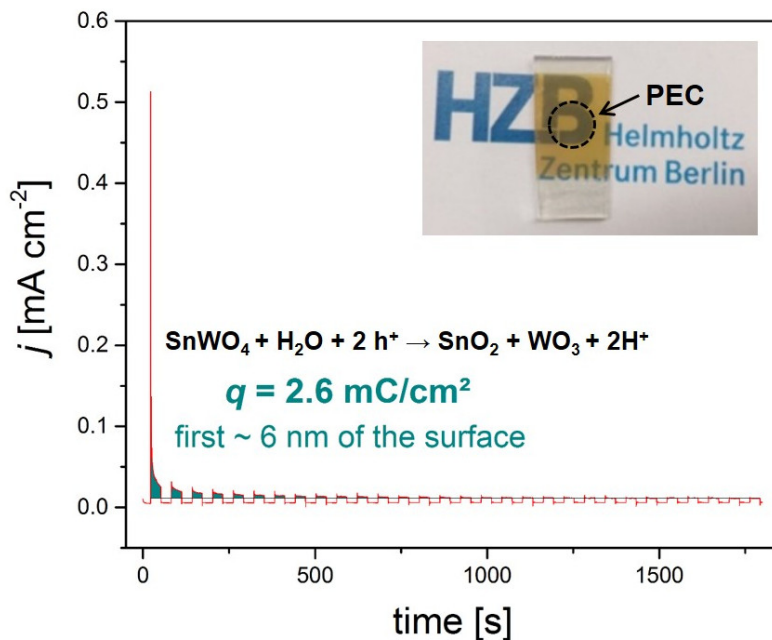


Figure S 23. Sulfite oxidation stability measurement of unprotected α -SnWO₄ photoelectrodes at a potential of $E = 1.23 \text{ V}$ vs. RHE under chopped AM1.5 illumination. The electrolyte was 0.5 M KPi-buffer solution (pH 7) and 0.5 M Na₂SO₃ added as a hole scavenger. The cyan colored area under the curve was used to estimate the thickness of the oxidized layer. Inset: Optical photograph of a FTO/ α -SnWO₄ photoelectrode after PEC measurement revealing no visible corrosion by eye.

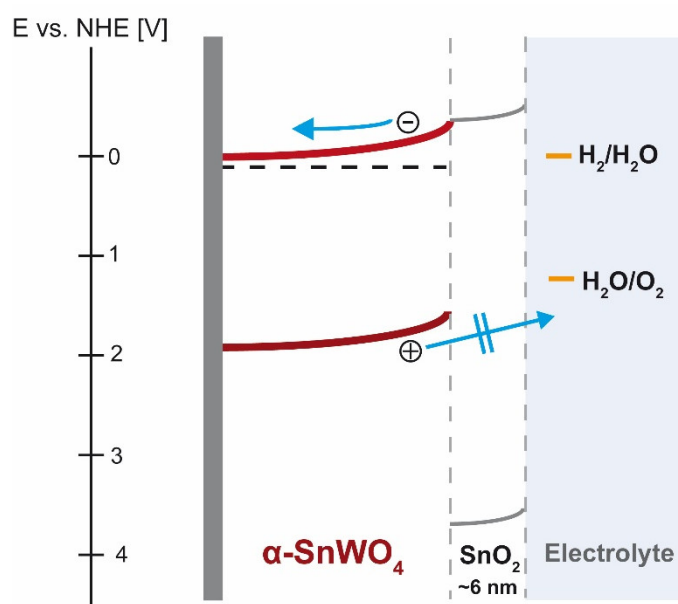


Figure S 24. Schematic band diagram of unprotected $\alpha\text{-SnWO}_4$ films after formation of the SnO_2 surface layer during PEC measurements.

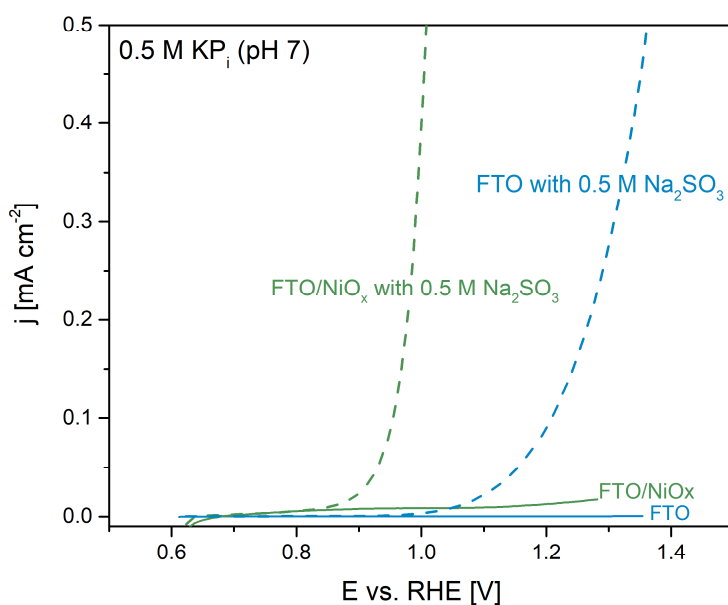


Figure S 25. LSV of FTO and FTO/ NiO_x in 0.5 M KPi (pH 7) buffer with (dashed lines) and without (solid lines) 0.5 M Na_2SO_3 .

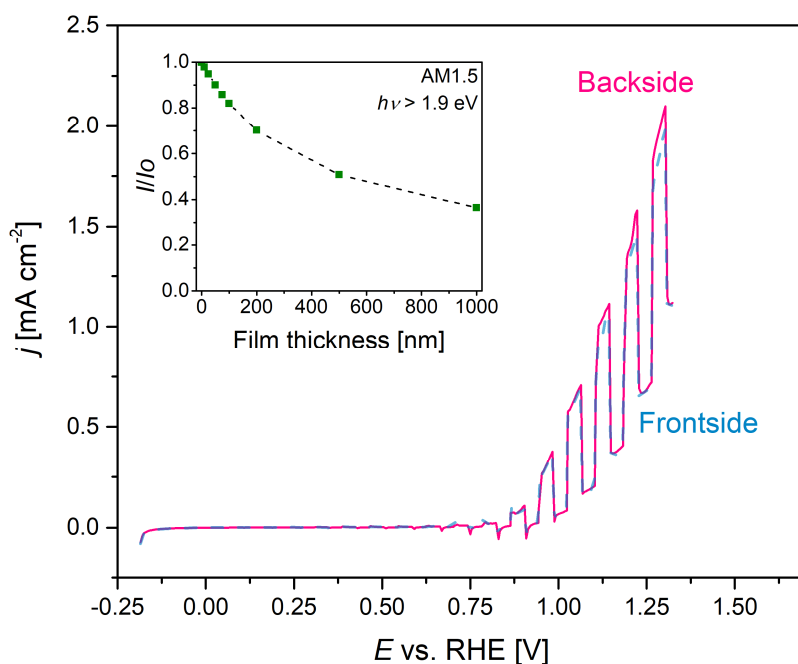


Figure S 26. Linear sweep voltammograms of α -SnWO₄/NiO_x films in 0.5 M KPi (pH 7) under frontside and backside AM1.5 illumination with 0.5 M Na₂SO₃ added as a hole scavenger. The scan rate was 20 mV s⁻¹. Inset: Absorption decay of the AM1.5 spectrum in α -SnWO₄ with photons $E_{ph} > 1.9$ eV based on UV/VIS measurements of α -SnWO₄ deposited on quartz.

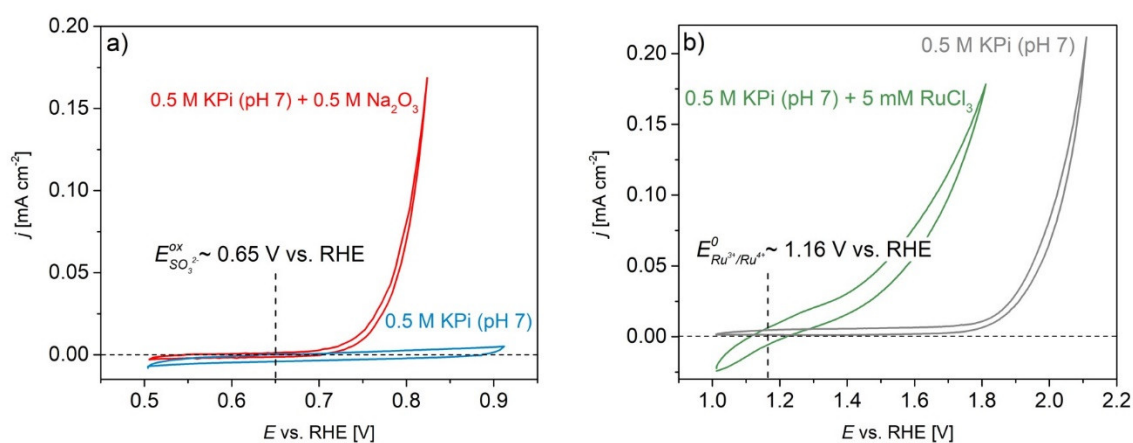


Figure S 27. **a)** Cyclic voltammograms on a Pt wire in 0.5 M KPi (pH 7) with and without 0.5 M Na₂SO₃. **b)** Cyclic voltammograms on FTO in 0.5 M KPi (pH 7) with and without RuCl₃. The scan rate was 20 mV s⁻¹ in all measurements.

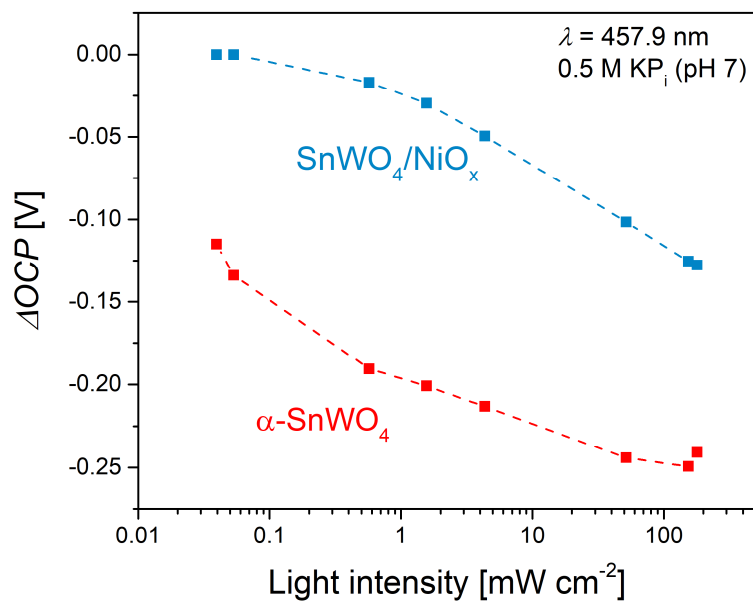


Figure S 28. Difference of the open circuit potential ΔOCP of $\alpha-SnWO_4$ and $\alpha-SnWO_4/NiO_x$ films in the dark and under illumination as a function of the light intensity ($\lambda = 457.9\ nm$). The electrolyte was $0.5\ M\ KPi$ ($pH\ 7$) with $0.5\ M\ Na_2SO_3$.

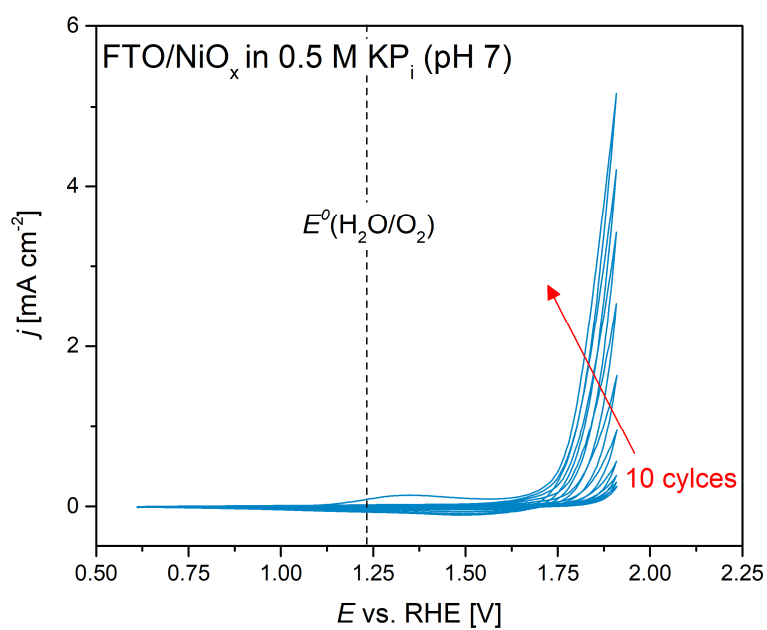


Figure S 29. Cyclic voltammograms of a $20\ nm\ NiO_x$ film pulsed laser deposited onto FTO in $0.5\ M\ KPi$ ($pH\ 7$) with a scan rate of $20\ mV\ s^{-1}$.

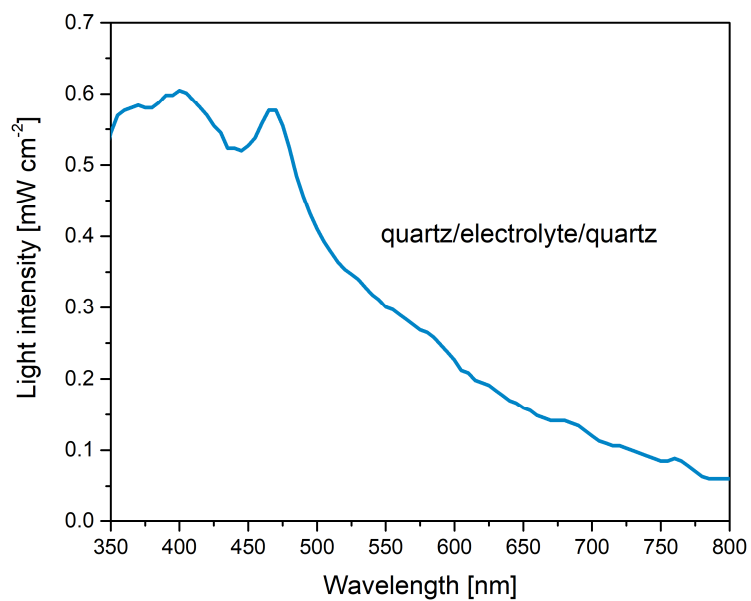


Figure S 30. Power spectrum of the lamp used for frontside illuminated and wavelength dependent IPCE measurements. The power was measured through the PEC cell (quartz/electrolyte/quartz).

b) List of abbreviations

Abbreviation	Definition
<i>A</i>	Absorptance
<i>ALD</i>	Atomic layer deposition
<i>AM1.5</i>	Air mass 1.5 (terrestrial solar spectrum where the sun is $\sim 41^\circ$ above the horizon)
<i>CBM</i>	Conduction band minimum
<i>CE</i>	Counter electrode
<i>C_{HL}</i>	Capacitance of the Helmholtz layer
<i>C_{SC}</i>	Capacitance of the space charge layer
<i>d</i>	Target-to-substrate distance
<i>d_{ds}</i>	Coherent scattering domain size
<i>DFT</i>	Density functional theory
<i>DOS</i>	Density of states
<i>E</i>	Potential
<i>EA</i>	Electron affinity
<i>E_{binding}</i>	Binding energy of the electrons
<i>EDX</i>	Energy-dispersive X-ray spectroscopy
<i>E_F</i>	Fermi level
<i>E_{F,n}</i>	Quasi Fermi level of the electrons
<i>E_{F,p}</i>	Quasi Fermi level of the holes
<i>E_g</i>	Bandgap
<i>E_{ph}</i>	Photon energy
<i>E_{vac}</i>	Vacuum energy level
<i>F</i>	Laser fluence (energy per area)
<i>FTO</i>	Fluorine-doped tin oxide
<i>h</i>	Planck's constant
<i>HER</i>	Hydrogen evolution reaction
<i>HIM</i>	Helium ion microscopy
<i>HRSEM</i>	High-resolution scanning electron microscopy
<i>I₀</i>	Light intensity
<i>IE</i>	Ionization energy level

<i>IPCE</i>	Incident-photon-to-current efficiency
j_{op}	Operating photocurrent density
j_{ph}	Photocurrent
k_b	Boltzmann constant
N_D	Density of ionized donors
ϕ	Internal quantum yield
<i>OER</i>	Oxygen evolution reaction
<i>PEC</i>	Photoelectrochemical
<i>PLD</i>	Pulsed laser deposition
p_{O_2}	Oxygen background pressure
<i>QCM</i>	Quartz crystal microbalance
<i>RBS</i>	Rutherford backscattering spectrometry
<i>REF</i>	Reference electrode
<i>RHE</i>	Reversible hydrogen electrode
<i>SEC</i>	Secondary electron cutoff
<i>SEM</i>	Scanning electron microscopy
<i>T</i>	Temperature
<i>t</i>	Film thickness
<i>TR</i>	Transflectance
<i>TRMC</i>	Time-resolved microwave conductivity
<i>TRTS</i>	Time-resolved terahertz spectroscopy
T_{sub}	Substrate temperature
U_{bias}	Bias voltage
<i>UPS</i>	Ultraviolet photoelectron spectroscopy
<i>VBM</i>	Valence band maximum
V_{ph}	Photovoltage
<i>WE</i>	Working electrode
W_{HL}	Width of the Helmholtz layer
W_{SC}	Width of the space charge layer
<i>XPS</i>	X-ray photoelectron spectroscopy
<i>XRD</i>	X-ray diffraction
α	Absorption coefficient
$\Delta\phi_{max}$	Potential difference between the flatband potential and the redox potential of the water oxidation (for photoanodes) and reduction (for photocathodes)

ϵ_0	Dielectric permittivity
ϵ_r	Relative dielectric permittivity
η_{STH}	Solar-to-hydrogen efficiency
θ	Angle of incidence of the X-ray beam in XRD measurements
λ	Wavelength
μ_{HER}	Overpotential for the hydrogen evolution reaction
μ_{OER}	Overpotential for the oxygen evolution reaction
ν	Frequency
σ	Conductivity
ϕ	Work function
ϕ_{FB}	Flatband potential
ϕ_{SC}	Potential drop in the space charge layer

c) List of figures

- Figure 1. a)** Global CO₂ emissions from 1850 up until now adapted from reference [3]. Inset: CO₂ concentration in the earth's atmosphere according to reference [5]. **b)** Global annual mean surface air temperature change from 1880 until now revealing a global warming of 0.9°C (base period: 1951-1980) adapted from reference [6]. 2
- Figure 2.** World map with the location of potential tipping cascades with estimated threshold temperatures (change of the global surface temperature) adapted from reference [7]. 3
- Figure 3.** Global power capacities of sustainable energy resources adapted from references [9,11]. Inset: Area of the earth's surface needed to be covered with 10% efficient solar cells to generate a power of 20 TW adapted from reference [9]. 4
- Figure 4.** Future sustainable energy infrastructure with hydrogen produced by solar energy as a key element. 6
- Figure 5.** Schematic illustration of a photoelectrochemical water splitting device based on an n-type semiconducting photoelectrode and a metal counter electrode, both immersed in an aqueous electrolyte adapted from reference [28]. 9
- Figure 6. a)** Classification of materials based on their bandgap energy in metals, semiconductors and insulators. **b)** Photon flux of AM1.5 irradiation as a function of the wavelength (low x-axis) and photon energy (upper x-axis). 11
- Figure 7.** Energy diagram of a semiconductor including the definitions of the vacuum level (E_{vac}), energy of the valence band maximum (E_{VBM}), energy of the conduction band minimum (E_{CBM}), Fermi level (E_F), ionization energy (IE), work function (Φ), and electron affinity (EA). 12
- Figure 8.** Energy diagrams of a **a)** n-type semiconductor and **b)** p-type semiconductor. 14
- Figure 9. a)** Energy diagrams of an isolated n-type semiconductor and electrolyte. **b)** After getting in contact, charges flow from the semiconductor to the electrolyte until the Fermi level equilibrated with redox potential of the electrolyte. As a result, a space charger layer (W_{sc}) with a potential drop (Φ_{sc}) is formed in the semiconductor. **c)** Semiconductor/electrolyte interface under operating conditions. Upon illumination, a photovoltage (V_{ph}) is generated defined as the difference between the quasi Fermi levels of the holes ($E_{F,p}$) and electrons ($E_{F,n}$). 15
- Figure 10.** Energy diagram of PEC water splitting device based on an n-type semiconductor connected to a metal counter electrode via an external circuit, with both electrodes immersed in an aqueous electrolyte. Upon illumination, electron-hole pairs are generated in the semiconductor. The photovoltage (V_{ph}) equals to the difference of the quasi Fermi levels of the electrons and holes ($E_{F,n}$ and $E_{F,p}$). Due to the electric field in the space charge layer the holes are swept towards the semiconductor-liquid junction and drive the water oxidation reaction whereas the electrons in the conduction band travel to the metal counter electrode via an external circuit and drive the water reduction reaction. The membrane ensures the product separation of the two half-cell reactions. 17
- Figure 11. a)** Cumulative photocurrent as a function of the bandgap of the semiconductor. Inset: STH-efficiency of a single absorber device as a function of its bandgap estimated under the assumption of an energy loss of 0.49 eV, perfect band alignment and the current-voltage characteristics of RuO_x (OER) and Pt (HER) catalysts (adapted from reference [31]). 19
- Figure 12.** Schematic energy diagram of a tandem device for solar water splitting consisting of a photoanode and photocathode as a top and bottom absorber, respectively, with both electrodes immersed in an aqueous electrolyte. Upon illumination, electrons-hole pairs and a photovoltage are generated in the top absorber. The transmitted photons ($E_{ph} < E_{g, top}$) generate electron-hole pairs and a photovoltage in the bottom absorber. The photogenerated holes in the photoanode drive the OER, while the photogenerated electrons in the conduction band of the photocathode drive the HER. The electrons in the conduction band of the photoanode travel to the photocathode via the external circuit and recombine with the holes in the valence band. The membrane ensures the separation of the produced O₂ and H₂ gas. 20

- Figure 13. a)** Contour plot of the solar to hydrogen efficiency of a stacked dual absorber tandem device as a function of the bandgap of the top and bottom absorber assuming a free energy loss of 0.49 eV, perfectly aligned bands and the current–voltage characteristics of Pt (HER) and RuO_x (OER) catalysts adapted from reference [31]. The white triangle indicates the area with a STH efficiency of > 10%. **b)** Overlaid photocurrents of a photoanode and photocathode as a function of the applied potential indicating the operation point of the tandem device. The $\Delta\phi_{\max}$ values for both absorbers are illustrated. 21
- Figure 14.** Schematic energy diagram of a PV-biased photoelectrochemical cell. In contrast to the tandem device consisting of two photoelectrodes (see **Figure 12**), the additional photovoltage needed for overall water splitting is provided by the PV cell. 22
- Figure 15.** Device concepts for photoelectrochemical solar water splitting based on **a)** III-V compound semiconductors adapted from reference [32] and **b)** metal oxide photoelectrodes adapted from reference [33]. 23
- Figure 16.** Maximum theoretical AM1.5 photocurrent (defined by the bandgap) vs. $\Delta\phi_{\max}$ of **a)** p-type and **b)** n-type complex metal oxide photoelectrode materials adapted from reference [28]. Grey areas indicate a $j_{\max, AM1.5} < 10\%$. The colored areas indicate the most suitable tandem configuration for the respective photoelectrode material. (Magenta \triangleq photocathode/–anode or single junction Si; yellow \triangleq photocathode/–anode or multi junction Si; and green \triangleq multijunction Si) 25
- Figure 17. a)** Crystal structure of monoclinic BiVO₄ (clinobisvanite) shown along the (*b*-axis). Oxygen, vanadium and Bi ions are colored in red, blue and yellow, respectively. **b)** Electronic band structure of monoclinic BiVO₄ (clinobisvanite) as obtained by DFT calculations as well as X-ray absorption spectroscopy (XAS), X-ray emission spectroscopy (XES) and X-ray emission spectroscopy (XPS) measurements adapted from reference [76]. 26
- Figure 18. a)** Crystal structure of orthorhombic α -SnWO₄ shown along the (*c*-axis). Oxygen, tin and W ions are colored in red, purple and gray, respectively. **b)** DFT calculation of the density of states (DOS) of α -SnWO₄ adapted from reference [98]. 28
- Figure 19. a)** Schematic drawing of a PLD system consisting of a target carousel and a heatable substrate holder both equipped with a scanning system in vacuum chamber. A high power pulsed laser (typically KrF-Excimer or Nd:YAG) is focused on a target resulting in the ablation of the material. Partially ionized by the laser, the ablated species form a luminous plasma plume that expands away from the target and are collected on a substrate, on which a thin film is grown. During the deposition gas inlets allow the use of different background pressures such as oxygen, argon or hydrogen. **b)** Optical photograph of our PLD chamber from PREVAC (Poland). 31
- Figure 20.** Overview of the target preparation. **a)** Ball mill used for grinding and mixing of powders. **b)** Pressing tool used for pressing the powders into a pellet. **c)** Hydraulic press with the homebuilt vacuum recipient. **d)** Finished BiVO₄ target. 33
- Figure 21. a)** Schematic representation of Rutherford backscattering spectrometry (RBS) analysis adapted from reference [111]. Light ions are accelerated (1–3 MeV) and focused on the specimen in a vacuum chamber while measuring the energy distribution and yield of the elastically backscattered ions at a certain angle. **b)** Typical RBS spectrum of a thin film (in this case BiVO₄) on a glassy carbon substrate. The height of the signal determines the concentration of the element in the films whereas the width of the signal provides information about the film thickness and the depth profile. 35
- Figure 22.** Schematic illustration of X-ray diffraction by a crystalline material. Constructive interference occurs when the difference in the optical path of scattered X-ray waves by two crystalline planes with a distance d_{hkl} ($2d_{hkl} \sin\theta$) is equal to an integer multiple of the wavelength of the incident X-ray (λ) (Bragg's law). 37
- Figure 23.** Measurement geometries for X-ray diffraction. **a)** $\theta/2\theta$ geometry in which X-ray tube and the detector have the same angle (θ) with respect to the sample during the whole measurement. **b)** Grazing incidence geometry commonly used for thin film samples. Here, the X-ray tube is fixed at a small angle (ω) and only the detector moves during the measurement increasing the surface sensitivity. 38

Figure 24. a) Time-resolved microwave conductivity (TRMC) measurement setup with an optical photograph of the cavity. **b)** Typical TRMC signal of a semiconducting material depicting the peak mobility ($\sigma_{\Sigma\mu}_{max}$) and the effective lifetime (τ). 39

Figure 25. a) Photoelectrochemical cell with a three electrode arrangement: reference electrode (REF), counter electrode (CE) and the photoelectrode as the working electrode (WE). The cell can be filled with an electrolyte and has a transparent window to allow illumination during the measurements. **b)** PEC measurement setup consisting of an AM1.5 solar simulator, a shutter, and the PEC cell connected to a potentiostat. In addition, a typical photocurrent measurement is shown indicating the onset potential of the photocurrent. 41

Figure 26. a) Wavelength-dependent IPCE measurement setup consisting of a Xe lamp coupled to monochromator, a longpass filter and a PEC cell connected to a potentiostat. **b)** Light intensity dependent IPCE measurement setup using an Ar ion laser and different optical density filters as an excitation source. Typical measurement results for both methods are shown. 42

Figure 27. Schematic drawing of the three main PLD processes that occur during the preparation of BiVO₄ thin films by ablating a BiVO₄ target 49

Figure 28. a) Impact of the laser fluence (F) on the V:Bi ratio of the deposited film measured with RBS (top), on the V:Bi ratio of the target surface qualitatively measured with EDX (middle) and on the deposited mass (Δm) determined with a quartz crystal microbalance (bottom). Films with a thickness of ~100 nm were deposited on glassy carbon in vacuum at RT. The target-to-substrate and target-to-QCM distances were both set to 60 mm. **b)** Scanning electron microscopy images of the BiVO₄ target surface after irradiation with different laser fluences. . 50

Figure 29. a) V:Bi ratio of films deposited on glassy carbon as a function of the oxygen background pressure measured with RBS. Films were deposited in vacuum at RT. Inset: V:Bi ratio of films deposited onto FTO with a substrate temperature of 400 °C as a function of the oxygen background pressure determined with RBS corrected EDX measurements. **b)** Qualitative Stopping-Range-of-Ions-in-Matter (SRIM) simulations for Bi and V atoms in an oxygen pressure of $p_{O_2} = 2.5 \times 10^{-2}$ mbar with a starting kinetic energy of 50 eV. **c)** V:Bi ratio of films deposited in vacuum onto FTO-glass as a function of the substrate temperature determined with RBS corrected EDX measurements. The laser fluence 1.5 J cm⁻² and the target-to-substrate distance was 60 mm for all shown depositions. 51

Figure 30. a) X-ray diffractograms of the BiVO₄ target and the BiVO₄ film with a thickness of 90 nm deposited on a FTO substrate ($F = 1.5$ J cm⁻², vacuum, RT, annealing in air at 450 °C for 2 h). Orange lines represent the reference pattern of monoclinic BiVO₄ (PDF no. 00-014-0688). The reflections of the underlying FTO substrate are marked with black asterisks (cassiterite, SnO₂, PDF no. 00-041-1445). **b)** SEM cross section of the respective BiVO₄ film. Inset: optical photograph. 54

Figure 31. Maximum TRMC signal ($\sigma_{\Sigma\mu}_{max}$) vs. photons per laser pulse ($\lambda = 355$ nm) of BiVO₄ films pulsed laser deposited on quartz substrates with a fluence of 1.0 and 1.5 J cm⁻². The error bars represent the spread from measurements of three identically prepared films. Inset: TRMC signal of the respective films at an intensity of $\sim 1.5 \times 10^{13}$ photons cm⁻². 56

Figure 32. a) X-ray diffractograms of films deposited on quartz by ablating a BiVO₄ target in vacuum at RT with a fluence of 1.0 and 1.5 J cm⁻², respectively. Both films were annealed at 450 °C for 2h in air. Orange lines represent the reference pattern of monoclinic BiVO₄ (PDF no. 00-014-0688). **b)** and **c)** SEM images of the respective films. 57

Figure 33. Photocurrent at a potential of 1.23 V vs. RHE as a function of the thickness of BiVO₄ photoanodes under AM1.5 illumination ($F = 1.5$ J cm⁻², vacuum, RT, annealing in air at 450 °C for 2 h). The electrolyte was a 0.5 M KP_r-buffer (pH ~ 7) with 0.5 M Na₂SO₃ added as a hole scavenger. 58

Figure 34. a) Linear sweep voltammetry scan of a BiVO₄ photoanode with a thickness of ~90 nm under chopped front- and backside AM1.5 illumination. The film was deposited with a fluence of 1.5 J cm⁻² onto FTO in vacuum at RT and annealed in air at 450 °C for 2 h. The electrolyte was a 0.5 M KP_r-buffer (pH ~7) with 0.5 M Na₂SO₃ as a hole scavenger. The scan rate was 20 mV s⁻¹. Inset: Photocurrent at $E = 1.23$ V vs. RHE of seven identical prepared films on FTO under front- and backside AM1.5 illumination. **b)** Sulfite oxidation photocurrent of

films (~90 nm) at a potential of 1.23 V vs. RHE under backside AM1.5 illumination as a function of their V:Bi ratio resulting from different fluences used for the deposition. The V:Bi ratio of the films was determined by RBS calibrated EDX measurements. 59

Figure 35. Linear sweep voltammetry scans of a BiVO₄ photoanode with a thickness of ~90 nm under chopped backside AM1.5 illumination ($F=1.5 \text{ J cm}^{-2}$, vacuum, RT, annealing in air at 450 °C for 2 h) before and after the deposition of CoPi. The electrolyte was a 0.5 M KP_i-buffer (pH 7) and the scan rate was 20 mV s⁻¹. 60

Figure 36. Schematic drawing of the PLD process of BiVO₄ photoelectrodes by the alternating ablation of Bi₂O₃ and V₂O₅ targets. 61

Figure 37. X-ray diffractogram of a BiVO₄ photoelectrode with a thickness of ~90 nm deposited on FTO by the ablation of alternating V₂O₅ and Bi₂O₃ targets ($F = 1.5 \text{ J cm}^{-2}$, $p_{O_2} = 5 \times 10^{-2} \text{ mbar}$, $T_{sub} = 400^\circ\text{C}$, V₂O₅:Bi₂O₃ shots-on-target ratio = 15). Orange and black lines represent the reference pattern of monoclinic BiVO₄ (PDF no. 00-014-0688) and the underlying FTO substrate (PDF no. 00-041-1445), respectively. The reflections of the FTO are additionally marked with black asterisks (*). 62

Figure 38. Linear sweep voltammograms of BiVO₄ film with a thickness of ~90 nm under chopped AM1.5 illumination prepared by the alternating ablation of V₂O₅ and Bi₂O₃ targets. ($F = 1.5 \text{ J cm}^{-2}$, $p_{O_2} = 5 \times 10^{-2} \text{ mbar}$, $T_{sub} = 400^\circ\text{C}$, V₂O₅:Bi₂O₃ shots-on-target ratio = 15) The electrolyte was a 0.5 M KP_i-buffer (pH ~ 7) with 0.5 M Na₂SO₃ as a hole scavenger. The scan rate was 20 mV s⁻¹ Inset: Photocurrent at $E = 1.23 \text{ V vs. RHE}$ under front- and backside AM1.5 illumination of five identical films prepared by the alternating target approach. 63

Figure 39. Deposited mass (Δm) during the ablation of a α -SnWO₄ target measured with a quartz crystal microbalance (QCM) as a function of the laser fluence. The target-to-QCM distance was 60 mm. 67

Figure 40. Sn:W ratio measured by RBS of films (~100 nm) deposited on glassy carbon at RT by ablating a α -SnWO₄ target in **a**) vacuum under variation of the laser fluence and **b**) in different oxygen background pressures with a fluence of 2 J cm⁻². The target-to-substrate distance was 60 mm in all depositions. 68

Figure 41. X-ray diffractograms of films deposited on quartz at RT with different oxygen background pressures before and after annealing at 600°C in argon for 2 h. The fluence was 2 J cm⁻² and the target-to-substrate distance was $d = 60 \text{ mm}$. Brown and black lines represent the α -SnWO₄ (PDF 01-070-1059) and Sn_{0.23}WO₃ (IOCD 81326) reference patterns, respectively. Reflections of the Sn_{0.23}WO₃ phase are marked with black asterisks (*). 69

Figure 42. a) X-ray diffractograms of α -SnWO₄ films annealed at different temperatures for 2 h in Ar ($F = 2 \text{ J cm}^{-2}$, $p_{O_2} = 2.5 \times 10^{-4} \text{ mbar}$). Brown, black and red lines represents the reference pattern of α -SnWO₄ (PDF 01-070-1059), Sn_{0.23}WO₃ (IOCD 81326) and β -SnWO₄ (PDF 01-070-1497), respectively. The reflections of the Sn_{0.23}WO₃ phase are marked with black asterisks (*). **b)** Coherent scattering domain size of α -SnWO₄ films as a function of the annealing temperature. 71

Figure 43. Helium ion microscopy images of quartz/ α -SnWO₄ thin films ($F = 2 \text{ J cm}^{-2}$, $p_{O_2} = 2.5 \times 10^{-4} \text{ mbar}$, $t = 200 \text{ nm}$). **a**) Image of the as deposited film. **b) – f)** Images of films annealed at temperatures ranging from 500 to 700°C revealing a steady growth and coalescence of the grains. The Sn_{0.23}WO₃ phase is visible for in the films annealed at 650° and 700°C is indicated by red arrows. 72

Figure 44. a) Absorption coefficient of phase-pure α -SnWO₄ deposited on quartz ($F = 2 \text{ J cm}^{-2}$, $p_{O_2} = 2.5 \times 10^{-4} \text{ mbar}$, $t = 200 \text{ nm}$, annealed at 600°C for 2h in Ar) as a function of wavelength. Insets: Optical photograph and direct (green) and indirect (red) Tauc plots. **b)** Absorbable part of the AM1.5 spectrum of α -SnWO₄ films with different thicknesses calculated from the absorption coefficient. The absorption coefficient at the wavelength which corresponds to the bandgap ($\lambda = 653 \text{ nm}$) was set to zero for the calculation. Inset: Maximum achievable photocurrent density as a function of the α -SnWO₄ film thickness. 73

Figure 45. X-ray diffractogram of a FTO/ α -SnWO₄ film ($F = 2 \text{ J cm}^{-2}$, $p_{O_2} = 2.5 \times 10^{-4} \text{ mbar}$, annealed at 600°C for 2 h in Ar) and the FTO substrate measured with a grazing incidence geometry. The brown lines represent the reference pattern of α -SnWO₄ (PDF no. 01-070-1049). The additional reflections from the FTO substrate in the diffractogram of FTO/ α -SnWO₄ are marked with asterisks (*). 74

- Figure 46. a), b)** Ultraviolet photoelectron spectroscopy measurements of FTO/ α -SnWO₄ using a He I photon source ($E = 21.2$ eV). **a)** Biased measurement ($E_{bias} = 2$ V) to determine the Secondary Electron Cutoff (SEC) and the work function (Φ). **b)** Determination of the valence band maximum (VBM) **c)** Schematic band diagram of α -SnWO₄ constructed from UPS measurements in **a)** and **b)**. The positions of the valence band maximum, Fermi level and the conduction band with respect to the vacuum level, the normal hydrogen electrode (NHE) potential, as well as the water oxidation and reduction potentials are depicted..... 75
- Figure 47.** Peak mobility as a function of photons per pulse for α -SnWO₄ films with a thickness of ~ 200 nm deposited on quartz ($F = 2$ J cm⁻², $p_{O_2} = 2.5 \times 10^{-4}$ mbar) annealed at different temperatures. The wavelength of the laser pulse was 355 nm. 76
- Figure 48.** TRMC signals at a laser intensity of 2.2×10^{13} cm⁻² ($\lambda = 355$ nm) of α -SnWO₄ films deposited on quartz ($F = 2$ J cm⁻², $p_{O_2} = 2.5 \times 10^{-4}$ mbar) and annealed at different temperatures for 2 h in Ar. Dashed lines represent the power-law fit of the signals. **b)** Normalized TRMC signals of a α -SnWO₄ film annealed at 700°C measured with varying laser pulse intensity (photons per pulse). Inset: effective carrier lifetimes ($\tau_{50\%}$) as a function of photons per pulse extracted from the signals. 77
- Figure 49. a)** Comparison of the probe in TRMC (microwave) and TRTS (THz pulse) measurements and the resulting difference in the random diffusion motion (L_D) of confined charge carriers in a grain during one oscillation of each probe. **b), c)** TRTS signals obtained for α -SnWO₄ films annealed at 600°C and 700°C in Ar for 2 h. The excitation laser pulse intensity was 7.0×10^{13} cm⁻² and the wavelength was 400 nm. **d)** TRMC- and TRTS-obtained carrier mobilities of α -SnWO₄ films as a function of the domain size resulting from annealing at different temperatures. The laser intensity was 2.2×10^{13} cm⁻² ($\lambda = 355$ nm) and 7.0×10^{13} cm⁻² ($\lambda = 400$ nm) in the TRMC and TRTS analysis, respectively. 80
- Figure 50.** Mobility as a function of lifetime of various metal oxide photoelectrodes measured with TRMC: α -SnWO₄ (this work), CuFeO₂^[155], BiVO₄^[47], Hydrogen doped BiVO₄ (H-BiVO₄)^[47], WO₃^[156], Fe₂O₃^[157], CuWO₄^[157], CuBi₂O₄^[158], FeVO₄^[64], Fe₂WO₆^[69] and Mn₂V₂O₇^[157]. Contour lines represent the calculated effective charge carrier diffusion length. 81
- Figure 51. a)** Sulfite oxidation stability measurement of 100 nm thick FTO/ α -SnWO₄ photoelectrodes ($F = 2$ J cm⁻², $p_{O_2} = 2.5 \times 10^{-4}$ mbar, annealed at 600°C for 2h in Ar; XRD data is shown in **Figure 45**) with and without a 20 nm NiO_x protection layer at a potential of 1.23 V vs. RHE under chopped AM1.5 illumination (dark currents are subtracted). The electrolyte was 0.5 M KPi-buffer solution (pH 7) and 0.5 M Na₂SO₃. **b)** XPS analysis of the Sn 3d region of the respective films before and after the stability measurement. B.E. = binding energy..... 82
- Figure 52.** HRSEM images of α -SnWO₄ photoelectrodes. **a)** Cross section of a pristine α -SnWO₄/NiO_x photoanode. The double arrows indicate the layer thicknesses in tilted view projection. The platinum layer on top was deposited to protect the film from ion-induced damage during the preparation of the cross section. **b), c)** Surface morphology of the α -SnWO₄ photoanodes before and after PEC measurements **b)** with and **c)** without a NiO_x protection layer. 83
- Figure 53.** Reproducibility of the photoelectrochemical performance of α -SnWO₄/NiO_x photoelectrodes. The photocurrent at a potential of 1.23 V vs. RHE in 0.5 M KPi (pH 7) with 0.5 M Na₂SO₃ under AM1.5 frontside illumination was chosen as a figure of merit. 84
- Figure 54.** Linear sweep voltammograms of α -SnWO₄/NiO_x films in 0.5 M KPi (pH7) under backside AM1.5 illumination with **a)** 0.5 M Na₂SO₃ or 5 mM RuCl₃ added as a hole scavenger and **b)** without any sacrificial agent. The scan rate was 20 mV s⁻¹. 86
- Figure 55. a)** IPCE as function of wavelength of α -SnWO₄/NiO_x photoelectrode. Inset: IPCE raw data showing the onset wavelength range of the photocurrent. **b)** IPCE as function of incident light intensity at a wavelength of $\lambda = 459.7$ nm. In both measurements, the film was illuminated from the frontside and a constant potential of 1.23 V vs. RHE was applied. The electrolyte was a 0.5 M KPi-buffer solution (pH 7) with 0.5 M Na₂SO₃ added as a hole scavenger. 87

d) List of tables

Table 1: Gravimetric and volumetric energy densities of various energy storage technologies 5
Table 2. Summary of key PEC parameters of α -SnWO₄ 89

e) Publications

1. M. Kölbach, K. Harbauer, K. Ellmer, R. van de Krol, *Elucidating the pulsed laser deposition process of efficient BiVO₄ photoelectrodes for solar water splitting*, **in preparation**
2. M. Kölbach, I. J. Pereira, K. Harbauer, P. Plate, K. Höflich, S. P. Berglund, D. Friedrich, R. van de Krol, F. F. Abdi, *Revealing the performance limiting factors in α -SnWO₄ photoanodes for solar water splitting*, **accepted by Chem. Mater.** (DOI: 10.1021/acs.chemmater.8b03883)
3. M. Kölbach, K. Harbauer, P. Plate, A. Petsiuk, H. Hempel, K. Höflich, V. Deinhart, D. Friedrich, R. Eichberger, F. F. Abdi, R. van de Krol, *Grain boundaries limit charge carrier transport in pulsed laser deposited α -SnWO₄ thin film photoabsorbers*, **in preparation**

f) Acknowledgement

First of all, I want to thank Roel for giving me the chance to do my PhD at the EE-IF, the excellent guidance through this exciting project, and all the help during the writing of the manuscripts and this thesis. I really enjoyed working with you and I learned a lot!

I would like to thank Klaus for all his help and guidance especially in the beginning of my research. Thank you for pointing me in the right direction based on your great experience in the deposition of thin films using PVD techniques (*“the devil is in in the detail”*).

Fatwa, thank you for all the fruitful scientific discussion and your help during the writing of the α -SnWO₄ manuscripts and this thesis. I really appreciated your uncomplicated and efficient way of working (even while you were on vacations)!

A big thank goes to Karsten, who has always immediately helped with all technical problems regarding the PLD system. I really enjoyed working and sharing the office with you!

In addition, I want to thank all my other colleagues at the HZB for their help and the nice working atmosphere. Especially, I want to thank Paul Plate for performing XPS measurements; Katja Höflich and Viktor Deinhart for taking microscopy images; Inês Jordão Pereira for assisting me in the early days of the α -SnWO₄ project; and Andrei Petsiuk and Hannes Hempel for performing TRTS measurements. In addition, I want to thank Marco Favaro, Dennis Friedrich, Sean Berglund, Rainer Eichberger, Ibrahim Ahmet, Yimeng Ma, Abdelkrim Chemseddine, David Starr, Peter Bogdanoff, Matthias Müller, Matthias May, Sebastian Fiechter, Rene Gunder, Daniel Abou-Ras, Mirjam Guerra and Marlene Lamers for all their help and fruitful scientific discussions. I would not have finished this thesis without you! I also thank PREVAC for teaching me some lessons about the complexity of building a PLD system and the consistently friendly working relationship.

I would also like to thank Prof. Dr. Alfred Ludwig for being my second referee, and Prof. Dr. Peter Hildebrandt for being the chairman at my defense.

Last but not least, I would like to acknowledge the German Bundesministerium für Bildung und Forschung (BMBF) for funding my research within the framework of the “MeOx4H2” project (03SF0478A).

Natürlich haben auch „nicht-wissenschaftliche“ Menschen zum Gelingen dieser Arbeit beigetragen. Dabei möchte ich mich als allererstes bei meinem Papa, meiner Mama und meiner Schwester bedanken, die mich seit 28 Jahren bei allem was ich mache bedingungslos unterstützen.

Bei meiner lieben Freundin Laura bedanke ich mich für die immense Unterstützung und Rücksicht während der *gesamten* 3 Jahre (*„Jetzt nur noch einen Monat hart arbeiten, dann hab ich’s geschafft“*).

Ich bedanke mich auch bei allen meinen Freunden (allen voran meine Mitbewohner Tugrul, Paola, Fabi, Denise & Lisa und Mike, Sam, Flo, Peete & Kai von den Suns of Shine)!

g) References

- [1] BP Statistical Review of World Energy 2018. <https://www.bp.com/>. Accessed August 2018.
- [2] BP Energy Outlook 2018. <https://www.bp.com/>. Accessed August 2018.
- [3] J. Gütschow, L. Jeffery, R. Gieseke, R. Gebel (2018): The PRIMAP-hist national historical emissions time series (1850-2015). V. 1.2. GFZ Data Services. <https://doi.org/10.5880/PIK.2018.003>. Accessed August 2018.
- [4] <https://www.esrl.noaa.gov/gmd/ccgg/trends/>. Accessed August 2018.
- [5] H. Moussab, Z. Ahmed, T. Kazuhiro, *physica status solidi (b)* **2016**, 253, 1115-1119.
- [6] <https://data.giss.nasa.gov/gistemp/graphs/>. Accessed August 2018.
- [7] W. Steffen, J. Rockström, K. Richardson, T. M. Lenton, C. Folke, D. Liverman, C. P. Summerhayes, A. D. Barnosky, S. E. Cornell, M. Crucifix, J. F. Donges, I. Fetzer, S. J. Lade, M. Scheffer, R. Winkelmann, H. J. Schellnhuber, *Proc. Natl. Acad. Sci. U. S. A.* **2018**.
- [8] <https://unfccc.int/>. Accessed August 2018.
- [9] R. van de Krol, M. Grätzel, Photoelectrochemical Hydrogen Production, Springer, New York, USA **2012**.
- [10] <http://www.iea-pvps.org/>. Accessed August 2018.
- [11] N.S. Lewis, G. Crabtree, Basic Research Needs for Solar Energy Utilization: report of the Basic Energy Sciences Workshop on Solar Energy Utilization, April 18-21, 2005. <http://resolver.caltech.edu/CaltechAUTHORS:LEWsolarenergyp05>. Accessed August 2018.
- [12] T. M. Gür, *Energy Environ. Sci.* **2018**, 11, 2696-2767
- [13] B. Bolund, H. Bernhoff, M. Leijon, *Renewable Sustainable Energy Rev.* **2007**, 11, 235-258.
- [14] G. J. May, A. Davidson, B. Monahov, *J Energy Storage* **2018**, 15, 145-157.
- [15] J. Janek, W. G. Zeier, *Nat. Energy* **2016**, 1, 16141.
- [16] R. van de Krol, B. A. Parkinson, *MRS Energy & Sustainability* **2017**, 4, E13.
- [17] B. Parkinson, *ACS Energy Lett.* **2016**, 1, 1057-1059.
- [18] <http://hydrogencouncil.com/>. Accessed August 2018.
- [19] <https://www.alstom.com/>. Accessed August 2018.
- [20] <https://www.now-gmbh.de/en>. Accessed August 2018.
- [21] K. Sturm, H.-U. Krebs, *J. Appl. Phys.* **2001**, 90, 1061-1063.
- [22] https://www.bundesnetzagentur.de/SharedDocs/Pressemitteilungen/EN/2016/161128_PVDK.html. Accessed August 2018.
- [23] B. A. Pinaud, J. D. Benck, L. C. Seitz, A. J. Forman, Z. Chen, T. G. Deutsch, B. D. James, K. N. Baum, G. N. Baum, S. Ardo, H. Wang, E. Miller, T. F. Jaramillo, *Energy Environ. Sci.* **2013**, 6, 1983-2002.
- [24] A. Fujishima, K. Honda, *Nature* **1972**, 238, 37.
- [25] P. Würfel, Physics of Solar Cells, Wiley-VCH, Weinheim, Germany **2005**.
- [26] S. Haussener, S. Hu, C. Xiang, A. Z. Weber, N. S. Lewis, *Energy Environ. Sci.* **2013**, 6, 3605-3618.
- [27] X. Ye, J. Melas-Kyriazi, Z. A. Feng, N. A. Melosh, W. C. Chueh, *Phys. Chem. Chem. Phys.* **2013**, 15, 15459-15469.
- [28] F. F. Abdi, S. Berglund, *J. Phys. D: Appl. Phys.* **2017**, 50, 193002.
- [29] S. Giménez, J. Bisquert, Photoelectrochemical Solar Fuel Production, Springer International Publishing, Switzerland **2016**.

- [30] C. C. L. McCrory, S. Jung, I. M. Ferrer, S. M. Chatman, J. C. Peters, T. F. Jaramillo, *J. Am. Chem. Soc.* **2015**, *137*, 4347-4357.
- [31] L. C. Seitz, Z. Chen, A. J. Forman, B. A. Pinaud, J. D. Benck, T. F. Jaramillo, *ChemSusChem* **2014**, *7*, 1372-1385.
- [32] W.-H. Cheng, M. H. Richter, M. M. May, J. Ohlmann, D. Lackner, F. Dimroth, T. Hannappel, H. A. Atwater, H.-J. Lewerenz, *ACS Energy Lett.* **2018**, *3*, 1795-1800.
- [33] F. F. Abdi, N. Firet, R. van de Krol, *ChemCatChem* **2013**, *5*, 490-496.
- [34] J.-W. Jang, C. Du, Y. Ye, Y. Lin, X. Yao, J. Thorne, E. Liu, G. McMahon, J. Zhu, A. Javey, J. Guo, D. Wang, *Nat. Commun.* **2015**, *6*, 7447.
- [35] L. Pan, J. H. Kim, M. T. Mayer, M.-K. Son, A. Ummadisingu, J. S. Lee, A. Hagfeldt, J. Luo, M. Grätzel, *Nat. Catal.* **2018**, *1*, 412-420.
- [36] P. Bornozy, F. F. Abdi, S. D. Tilley, B. Dam, R. van de Krol, M. Graetzel, K. Sivula, *J. Phys. Chem. C* **2014**, *118*, 16959-16966.
- [37] P. Dias, A. Vilanova, T. Lopes, L. Andrade, A. Mendes, *Nano Energy* **2016**, *23*, 70-79.
- [38] J. H. Kim, J.-W. Jang, Y. H. Jo, F. F. Abdi, Y. H. Lee, R. van de Krol, J. S. Lee, *Nat. Commun.* **2016**, *7*, 13380.
- [39] X. Shi, H. Jeong, S. J. Oh, M. Ma, K. Zhang, J. Kwon, I. T. Choi, I. Y. Choi, H. K. Kim, J. K. Kim, J. H. Park, *Nat. Commun.* **2016**, *7*, 11943.
- [40] S. M. Sze, *Physics of Semiconductor Devices*, John Wiley & Sons, New York, USA **1981**.
- [41] A. J. E. Rettie, W. D. Chemelewski, D. Emin, C. B. Mullins, *J. Phys. Chem. Lett.* **2016**, *7*, 471-479.
- [42] M. Ziwritsch, S. Müller, H. Hempel, T. Unold, F. F. Abdi, R. van de Krol, D. Friedrich, R. Eichberger, *ACS Energy Lett.* **2016**, *1*, 888-894.
- [43] S. K. Pilli, T. E. Furtak, L. D. Brown, T. G. Deutsch, J. A. Turner, A. M. Herring, *Energy Environ. Sci.* **2011**, *4*, 5028-5034.
- [44] S. P. Berglund, H. C. Lee, P. D. Núñez, A. J. Bard, C. B. Mullins, *Phys. Chem. Chem. Phys.* **2013**, *15*, 4554-4565.
- [45] D. Kang, J. C. Hill, Y. Park, K.-S. Choi, *Chem. Mater.* **2016**, *28*, 4331-4340.
- [46] G. Wang, Y. Ling, Y. Li, *Nanoscale* **2012**, *4*, 6682-6691.
- [47] J.-W. Jang, D. Friedrich, S. Müller, M. Lamers, H. Hempel, S. Lardhi, Z. Cao, M. Harb, L. Cavallo, R. Heller, R. Eichberger, R. van de Krol, F. F. Abdi, *Adv. Energy Mater.* **2017**, *7*, 1701536.
- [48] M. Lamers, S. Fiechter, D. Friedrich, F. F. Abdi, R. van de Krol, *J. Mater. Chem. A* **2018**, *6*, 18694-18700.
- [49] K. Sivula, R. Zboril, F. Le Formal, R. Robert, A. Weidenkaff, J. Tucek, J. Frydrych, M. Grätzel, *J. Am. Chem. Soc.* **2010**, *132*, 7436-7444.
- [50] H. S. Han, S. Shin, D. H. Kim, I. J. Park, J. S. Kim, P.-S. Huang, J.-K. Lee, I. S. Cho, X. Zheng, *Energy Environ. Sci.* **2018**, *11*, 1299-1306.
- [51] Y. Pihosh, I. Turkevych, K. Mawatari, J. Uemura, Y. Kazoe, S. Kosar, K. Makita, T. Sugaya, T. Matsui, D. Fujita, M. Tosa, M. Kondo, T. Kitamori, *Sci. Rep.* **2015**, *5*, 11141.
- [52] K. Sivula, F. Le Formal, M. Grätzel, *ChemSusChem* **2011**, *4*, 432-449.
- [53] A. Paracchino, V. Laporte, K. Sivula, M. Grätzel, E. Thimsen, *Nat. Mater.* **2011**, *10*, 456.
- [54] J. Luo, L. Steier, M.-K. Son, M. Schreier, M. T. Mayer, M. Grätzel, *Nano Lett.* **2016**, *16*, 1848-1857.
- [55] J. G. Rowley, T. D. Do, D. A. Cleary, B. A. Parkinson, *ACS Appl. Mater. Interfaces* **2014**, *6*, 9046-9052.
- [56] Q. Yan, J. Yu, S. K. Suram, L. Zhou, A. Shinde, P. F. Newhouse, W. Chen, G. Li, K. A. Persson, J. M. Gregoire, J. B. Neaton, *Proc. Natl. Acad. Sci. U. S. A.* **2017**, *114*, 3040-3043.

- [57] A. Shinde, S. K. Suram, Q. Yan, L. Zhou, A. K. Singh, J. Yu, K. A. Persson, J. B. Neaton, J. M. Gregoire, *ACS Energy Lett.* **2017**, *2*, 2307-2312.
- [58] R. Gutkowski, C. Khare, F. Conzuelo, Y. U. Kayran, A. Ludwig, W. Schuhmann, *Energy Environ. Sci.* **2017**, *10*, 1213-1221.
- [59] S. Kumari, R. Gutkowski, J. R. C. Junqueira, A. Kostka, K. Hengge, C. Scheu, W. Schuhmann, A. Ludwig, *ACS Comb. Sci.* **2018**, *20*, 544-553.
- [60] K. Sliozberg, D. Schäfer, T. Erichsen, R. Meyer, C. Khare, A. Ludwig, W. Schuhmann, *ChemSusChem* **2015**, *8*, 1270-1278.
- [61] R. Meyer, K. Sliozberg, C. Khare, W. Schuhmann, A. Ludwig, *ChemSusChem* **2015**, *8*, 1279-1285.
- [62] K. Sliozberg, D. Schäfer, R. Meyer, A. Ludwig, W. Schuhmann, *ChemPlusChem* **2015**, *80*, 136-140.
- [63] I. D. Sharp, J. K. Cooper, F. M. Toma, R. Buonsanti, *ACS Energy Lett.* **2017**, *2*, 139-150.
- [64] M. Zhang, Y. Ma, D. Friedrich, R. van de Krol, L. H. Wong, F. F. Abdi, *J. Mater. Chem. A* **2018**, *6*, 548-555.
- [65] C.-M. Jiang, M. Farmand, C. H. Wu, Y.-S. Liu, J. Guo, W. S. Drisdell, J. K. Cooper, I. D. Sharp, *Chem. Mater.* **2017**, *29*, 3334-3345.
- [66] S. Ida, K. Yamada, T. Matsunaga, H. Hagiwara, Y. Matsumoto, T. Ishihara, *J. Am. Chem. Soc.* **2010**, *132*, 17343-17345.
- [67] J. H. Kim, J. H. Kim, J.-W. Jang, J. Y. Kim, S. H. Choi, G. Magesh, J. Lee, J. S. Lee, *Adv. Energy Mater.* **2015**, *5*, 1401933.
- [68] J. E. Yourey, B. M. Bartlett, *J. Mater. Chem.* **2011**, *21*, 7651-7660.
- [69] F. F. Abdi, A. Chemseddine, S. P. Berglund, R. van de Krol, *J. Phys. Chem. C* **2017**, *121*, 153-160.
- [70] M. S. Prévot, N. Guijarro, K. Sivula, *ChemSusChem* **2015**, *8*, 1359-1367.
- [71] F. Wang, W. Septina, A. Chemseddine, F. F. Abdi, D. Friedrich, P. Bogdanoff, R. van de Krol, S. D. Tilley, S. P. Berglund, *J. Am. Chem. Soc.* **2017**, *139*, 15094-15103.
- [72] Y. J. Jang, Y. B. Park, H. E. Kim, Y. H. Choi, S. H. Choi, J. S. Lee, *Chem. Mater.* **2016**, *28*, 6054-6061.
- [73] A. Kudo, K. Ueda, H. Kato, I. Mikami, *Catal. Lett.* **1998**, *53*, 229-230.
- [74] C. Zachäus, F. F. Abdi, L. M. Peter, R. van de Krol, *Chem. Sci.* **2017**, *8*, 3712-3719.
- [75] A. W. Sleight, H. y. Chen, A. Ferretti, D. E. Cox, *Mater. Res. Bull.* **1979**, *14*, 1571-1581.
- [76] J. K. Cooper, S. Gul, F. M. Toma, L. Chen, P.-A. Glans, J. Guo, J. W. Ager, J. Yano, I. D. Sharp, *Chem. Mater.* **2014**, *26*, 5365-5373.
- [77] A. Kudo, K. Omori, H. Kato, *J. Am. Chem. Soc.* **1999**, *121*, 11459-11467.
- [78] J. K. Cooper, S. Gul, F. M. Toma, L. Chen, Y.-S. Liu, J. Guo, J. W. Ager, J. Yano, I. D. Sharp, *J. Phys. Chem. C* **2015**, *119*, 2969-2974.
- [79] J. K. Cooper, S. B. Scott, Y. Ling, J. Yang, S. Hao, Y. Li, F. M. Toma, M. Stutzmann, K. V. Lakshmi, I. D. Sharp, *Chem. Mater.* **2016**, *28*, 5761-5771.
- [80] K. Sayama, A. Nomura, T. Arai, T. Sugita, R. Abe, M. Yanagida, T. Oi, Y. Iwasaki, Y. Abe, H. Sugihara, *J. Phys. Chem. B* **2006**, *110*, 11352-11360.
- [81] F. F. Abdi, R. van de Krol, *J. Phys. Chem. C* **2012**, *116*, 9398-9404.
- [82] T. W. Kim, K.-S. Choi, *Science* **2014**, *343*, 990-994.
- [83] J. A. Seabold, K.-S. Choi, *J. Am. Chem. Soc.* **2012**, *134*, 2186-2192.
- [84] M. R. Nellist, J. Qiu, F. A. L. Laskowski, F. M. Toma, S. W. Boettcher, *ACS Energy Lett.* **2018**, *3*, 2286-2291.
- [85] K. E. Kweon, G. S. Hwang, J. Kim, S. Kim, S. Kim, *Phys. Chem. Chem. Phys.* **2015**, *17*, 256-260.

- [86] T. Liu, X. Zhou, M. Dupuis, C. Li, *Phys. Chem. Chem. Phys.* **2015**, *17*, 23503-23510.
- [87] K. P. S. Parmar, H. J. Kang, A. Bist, P. Dua, J. S. Jang, J. S. Lee, *ChemSusChem* **2012**, *5*, 1926-1934.
- [88] H. S. Park, K. E. Kweon, H. Ye, E. Paek, G. S. Hwang, A. J. Bard, *J. Phys. Chem. C* **2011**, *115*, 17870-17879.
- [89] P. M. Rao, L. Cai, C. Liu, I. S. Cho, C. H. Lee, J. M. Weisse, P. Yang, X. Zheng, *Nano Lett.* **2014**, *14*, 1099-1105.
- [90] X. Shi, I. Y. Choi, K. Zhang, J. Kwon, D. Y. Kim, J. K. Lee, S. H. Oh, J. K. Kim, J. H. Park, *Nat. Commun.* **2014**, *5*, 4775.
- [91] L. Zhou, C. Zhao, B. Giri, P. Allen, X. Xu, H. Joshi, Y. Fan, L. V. Titova, P. M. Rao, *Nano Lett.* **2016**, *16*, 3463-3474.
- [92] F. F. Abdi, A. Dabirian, B. Dam, R. van de Krol, *Phys. Chem. Chem. Phys.* **2014**, *16*, 15272-15277.
- [93] Y. Sang, Y. Huang, W. wang, Z. Fang, B. Geng, *RSC Adv.* **2015**, *5*, 39651-39656.
- [94] W. Jeitschko, A. W. Sleight, *Acta Crystallogr., Sect. B: Struct. Sci., Cryst. Eng. Mater.* **1972**, *28*, 3174-3178.
- [95] M. Harb, A. Ziani, K. Takanabe, *Phys. Status Solidi B* **2016**, *253*, 1115-1119.
- [96] A. Ziani, M. Harb, D. Noureldine, K. Takanabe, *APL Mater.* **2015**, *3*, 096101.
- [97] Z. Zhu, P. Sarker, C. Zhao, L. Zhou, R. L. Grimm, M. N. Huda, P. M. Rao, *ACS Appl. Mater. Interfaces* **2017**, *9*, 1459-1470.
- [98] I.-S. Cho, C. H. Kwak, D. W. Kim, S. Lee, K. S. Hong, *J. Phys. Chem. C* **2009**, *113*, 10647-10653.
- [99] K. J. Pyper, T. C. Evans, B. M. Bartlett, *Chin. Chem. Lett.* **2015**, *26*, 474-478.
- [100] H. M. Smith, A. F. Turner, *Appl. Opt.* **1965**, *4*, 147-148.
- [101] D. Dijkkamp, T. Venkatesan, X. D. Wu, S. A. Shaheen, N. Jisrawi, Y. H. Min-lee, W. L. Mclean, M. Croft, *Appl. Phys. Lett.* **1987**, *51*, 619-621.
- [102] A. G. James, *J. Phys. D: Appl. Phys.* **2014**, *47*, 034005.
- [103] R. Delmdahl, R. Pätzelt, *Appl. Phys. A: Mater. Sci. Process.* **2008**, *93*, 611-615.
- [104] S. Fähler, H.-U. Krebs, *Appl. Surf. Sci.* **1996**, *96-98*, 61-65.
- [105] C. B. Arnold, M. J. Aziz, *Appl. Phys. A: Mater. Sci. Process.* **1999**, *69*, S23-S27.
- [106] H. A. B. Dave, D. Matthijn, R. Guus, *J. Phys. D: Appl. Phys.* **2014**, *47*, 034006.
- [107] A. L. Geiler, S. D. Yoon, Y. Chen, A. Yang, C. N. Chinnasamy, M. Geiler, V. G. Harris, C. Vittoria, *J. Appl. Phys.* **2008**, *103*, 07B914.
- [108] A. Herklotz, K. Dörr, T. Z. Ward, G. Eres, H. M. Christen, M. D. Biegalski, *Appl. Phys. Lett.* **2015**, *106*, 131601.
- [109] J. Schou, *Appl. Surf. Sci.* **2009**, *255*, 5191-5198.
- [110] T. C. Droubay, L. Qiao, T. C. Kaspar, M. H. Engelhard, V. Shutthanandan, S. A. Chambers, *Appl. Phys. Lett.* **2010**, *97*, 124105.
- [111] <https://www.hzdr.de/db/Cms?pOid=29856&pNid=3537>. Accessed August 2018.
- [112] T. J. Savenije, A. J. Ferguson, N. Kopidakis, G. Rumbles, *J. Phys. Chem. C* **2013**, *117*, 24085-24103.
- [113] T. J. Savenije, A. Huijser, M. J. W. Vermeulen, R. Katoh, *Chem. Phys. Lett.* **2008**, *461*, 93-96.
- [114] J. E. Kroeze, T. J. Savenije, J. M. Warman, *J. Am. Chem. Soc.* **2004**, *126*, 7608-7618.
- [115] S.-H. Wee, D.-W. Kim, S.-I. Yoo, *J. Am. Ceram. Soc.* **2004**, *87*, 871-874.
- [116] L. M. Peter, *J. Solid State Electrochem.* **2013**, *17*, 315-326.
- [117] C. Strothkämper, K. Schwarzburg, R. Schütz, R. Eichberger, A. Bartelt, *J. Phys. Chem. C* **2012**, *116*, 1165-1173.

- [118] A. J. E. Rettie, S. Mozaffari, M. D. McDaniel, K. N. Pearson, J. G. Ekerdt, J. T. Markert, C. B. Mullins, *J. Phys. Chem. C* **2014**, *118*, 26543-26550.
- [119] S. Murcia-López, C. Fàbrega, D. Monllor-Satoca, M. D. Hernández-Alonso, G. Penelas-Pérez, A. Morata, J. R. Morante, T. Andreu, *ACS Appl. Mater. Interfaces* **2016**, *8*, 4076-4085.
- [120] S. Y. Jeong, K. S. Choi, H.-M. Shin, T. L. Kim, J. Song, S. Yoon, H. W. Jang, M.-H. Yoon, C. Jeon, J. Lee, S. Lee, *ACS Appl. Mater. Interfaces* **2017**, *9*, 505-512.
- [121] B. Dam, J. H. Rector, J. Johansson, J. Huijbregtse, D. G. D. Groot, *J. Appl. Phys.* **1998**, *83*, 3386-3389.
- [122] M. Tyunina, S. Leppävuori, *J. Appl. Phys.* **2000**, *87*, 8132-8142.
- [123] M. N. R. Ashfold, F. Claeysens, G. M. Fuge, S. J. Henley, *Chem. Soc. Rev.* **2004**, *33*, 23-31.
- [124] Y. Davila, A. Petitmangin, C. Hebert, J. Perrière, W. Seiler, *Appl. Surf. Sci.* **2011**, *257*, 5354-5357.
- [125] R. G. S. Roman, R. P. Casero, C. Maréchal, J. P. Enard, J. Perrière, *J. Appl. Phys.* **1996**, *80*, 1787-1793.
- [126] F. V. E. Hensling, D. J. Keeble, J. Zhu, S. Brose, C. Xu, F. Gunkel, S. Danylyuk, S. S. Nonnenmann, W. Egger, R. Dittmann, *Sci. Rep.* **2018**, *8*, 8846.
- [127] R. Perez-Casero, J. Perrière, A. Gutierrez-Llorente, D. Defourneau, E. Millon, W. Seiler, L. Soriano, *Phys. Rev. B* **2007**, *75*, 165317.
- [128] S. Heo, C. Oh, J. Son, H. M. Jang, *Sci. Rep.* **2017**, *7*, 4681.
- [129] L. M. Doeswijk, G. Rijnders, D. H. A. Blank, *Appl. Phys. A: Mater. Sci. Process.* **2004**, *78*, 263-268.
- [130] J. F. Ziegler, M. D. Ziegler, J. P. Biersack, *Nucl. Instrum. Methods Phys. Res.* **2010**, *268*, 1818-1823.
- [131] M. Lorenz, Pulsed Laser Deposition of ZnO-Based Thin Films, in: K. Ellmer, A. Klein, B. Rech (Eds.), *Transparent Conductive Zinc Oxide: Basics and Applications in Thin Film Solar Cells*, Springer Berlin Heidelberg, Berlin, Heidelberg, Germany **2008**, pp. 303-357.
- [132] C. Ma, C. Chen, Pulsed Laser Deposition for Complex Oxide Thin Film and Nanostructure, in: Y. Lin, X. Chen (Eds.), *Advanced Nano Deposition Methods*, Wiley-VCH, Weinheim, Germany **2016**, pp. 1-31.
- [133] S. Sasanka Kumar, R. Reshmi, N. V. Joshy, A. C. Saritha, M. K. Jayaraj, *J. At. Mol. Phys.* **2014**, *2014*, 9.
- [134] P. W. Atkins, *Physical Chemistry*, Oxford University Press, Oxford, UK **1990**.
- [135] S. K. Hau, K. H. Wong, P. W. Chan, C. L. Choy, *Appl. Phys. Lett.* **1995**, *66*, 245-247.
- [136] F. F. Abdi, T. J. Savenije, M. M. May, B. Dam, R. van de Krol, *J. Phys. Chem. Lett.* **2013**, *4*, 2752-2757.
- [137] J. E. Kroeze, T. J. Savenije, M. J. W. Vermeulen, J. M. Warman, *J. Phys. Chem. B* **2003**, *107*, 7696-7705.
- [138] J. W. Jang, D. Friedrich, S. Müller, M. Lamers, H. Hempel, S. Lardhi, Z. Cao, M. Harb, L. Cavallo, R. Heller, R. Eichberger, R. van de Krol, F. F. Abdi, *Adv. Energy Mater.* **2017**, *7*, 1701536.
- [139] O. G. Reid, M. Yang, N. Kopidakis, K. Zhu, G. Rumbles, *ACS Energy Lett.* **2016**, *1*, 561-565.
- [140] L. Chen, E. Alarcón-Lladó, M. Hettick, I. D. Sharp, Y. Lin, A. Javey, J. W. Ager, *J. Phys. Chem. C* **2013**, *117*, 21635-21642.
- [141] F. F. Abdi, L. Han, A. H. M. Smets, M. Zeman, B. Dam, R. van de Krol, *Nat. Commun.* **2013**, *4*, 2195.

- [142] L. Chen, F. M. Toma, J. K. Cooper, A. Lyon, Y. Lin, I. D. Sharp, J. W. Ager, *ChemSusChem* **2015**, *8*, 1066-1071.
- [143] F. Gauzzi, B. Verdini, A. Maddalena, G. Principi, *Inorg. Chim. Acta* **1985**, *104*, 1-7.
- [144] J. L. Solis, J. Frantti, V. Lantto, L. Häggström, M. Wikner, *Phys. Rev. B* **1998**, *57*, 13491-13500.
- [145] A. Kuzmin, M. Zubkins, R. Kalendarev, *Ferroelectrics* **2015**, *484*, 49-54.
- [146] J. L. Solis, V. Lantto, *Sens. Actuators, B* **1998**, *48*, 322-327.
- [147] R. Brenot, R. Vanderhaghen, B. Dreviron, I. French, P. Roca i Cabarrocas, *Thin Solid Films* **1997**, *296*, 94-97.
- [148] J. Ravensbergen, F. F. Abdi, J. H. van Santen, R. N. Frese, B. Dam, R. van de Krol, J. T. M. Kennis, *J. Phys. Chem. C* **2014**, *118*, 27793-27800.
- [149] D. Friedrich, M. Kunst, *Nano Energy* **2012**, *1*, 303-308.
- [150] P. H. Sher, J. M. Smith, P. A. Dalgarno, R. J. Warburton, X. Chen, P. J. Dobson, S. M. Daniels, N. L. Pickett, P. O'Brien, *Appl. Phys. Lett.* **2008**, *92*, 101111.
- [151] M. Kuno, D. P. Fromm, H. F. Hamann, A. Gallagher, D. J. Nesbitt, *J. Chem. Phys.* **2000**, *112*, 3117-3120.
- [152] R. Ulbricht, E. Hendry, J. Shan, T. F. Heinz, M. Bonn, *Rev. Mod. Phys.* **2011**, *83*, 543-586.
- [153] H. Němec, P. Kužel, V. Sundström, *J. Photochem. Photobiol., A* **2010**, *215*, 123-139.
- [154] H. Hempel, A. Redinger, I. Repins, C. Moisan, G. Larramona, G. Dennler, M. Handwerg, S. F. Fischer, R. Eichberger, T. Unold, *J. Appl. Phys.* **2016**, *120*, 175302.
- [155] M. S. Prévot, X. A. Jeanbourquin, W. S. Bourée, F. Abdi, D. Friedrich, R. van de Krol, N. Guijarro, F. Le Formal, K. Sivula, *Chem. Mater.* **2017**, *29*, 4952-4962.
- [156] S. Hilliard, G. Baldinozzi, D. Friedrich, S. Kressman, H. Strub, V. Artero, C. Laberty-Robert, *Sustainable Energy Fuels* **2017**, *1*, 145-153.
- [157] Unpublished results from our institute.
- [158] S. P. Berglund, F. F. Abdi, P. Bogdanoff, A. Chemseddine, D. Friedrich, R. van de Krol, *Chem. Mater.* **2016**, *28*, 4231-4242.
- [159] S. Y. Jeong, H.-M. Shin, Y.-R. Jo, Y. J. Kim, S. Kim, W.-J. Lee, G. J. Lee, J. Song, B. J. Moon, S. Seo, H. An, S. H. Lee, Y. M. Song, B.-J. Kim, M.-H. Yoon, S. Lee, *J. Phys. Chem. C* **2018**, *122*, 7088-7093.
- [160] I. Thomann, B. A. Pinaud, Z. Chen, B. M. Clemens, T. F. Jaramillo, M. L. Brongersma, *Nano Lett.* **2011**, *11*, 3440-3446.
- [161] X. Zhang, G. Ji, Y. Liu, X. Zhou, Y. Zhu, D. Shi, P. Zhang, X. Cao, B. Wang, *Phys. Chem. Chem. Phys.* **2015**, *17*, 8078-8086.
- [162] J. C. Hill, K.-S. Choi, *J. Phys. Chem. C* **2012**, *116*, 7612-7620.
- [163] S. Tanuma, C. J. Powell, D. R. Penn, *Surf. Interface Anal.* **1994**, *21*, 165-176.
- [164] Y. Liang, T. Tsubota, L. P. A. Mooij, R. van de Krol, *J. Phys. Chem. C* **2011**, *115*, 17594-17598.
- [165] Y. Liang, C. S. Enache, R. van de Krol, *Int. J. Photoenergy* **2008**, *2008*, 7.
- [166] J. Kamimura, P. Bogdanoff, F. F. Abdi, J. Lähnemann, R. van de Krol, H. Riechert, L. Geelhaar, *J. Phys. Chem. C* **2017**, *121*, 12540-12545.
- [167] P. W. Menezes, A. Indra, O. Levy, K. Kailasam, V. Gutkin, J. Pfrommer, M. Driess, *Chem. Commun.* **2015**, *51*, 5005-5008.
- [168] O. Diaz-Morales, D. Ferrus-Suspedra, M. T. M. Koper, *Chem. Sci.* **2016**, *7*, 2639-2645.